Genesis and $^{40}Ar/^{39}Ar$ dating of K-Mn oxides from the Stavelot Massif (Ardenne, Belgium): Insights into Oligocene to Pliocene weathering periods in Western Europe

Augustin Dekoninck[a,*], Patrick Monié[b], Sabine Blockmans[a,c], Frédéric Hatert[d], Gaëtan Rochez[a], Johan Yans[a]

[a] *Institute of Life-Earth-Environment (ILEE), University of Namur, 61 rue de Bruxelles B-5000 Namur, Belgium*
[b] *Géosciences Montpellier, UMR-CNRS 5243, Université de Montpellier, Montpellier, France*
[c] *Service Géologique de Wallonie, DGO3, Service Public de Wallonie, 14 Avenue Prince de Liège B-5100, Jambes, Belgium*
[d] *Laboratoire de Minéralogie, Université de Liège, 14 allée du six août B-4000, Liège, Belgium*

ARTICLE INFO

ABSTRACT

The occurrence of Ordovician Fe-Mn-rich sediments (Ottré Formation, Salm Group) in the Stavelot inlier (NE Ardenne, Rhenish Massif, Belgium) has drawn the attention of geoscientists for more than one century, as they contain natural "coticule" whetstones and numerous weathered Mn deposits. Two locations expose the Fe-Mn-bearing rocks: the Chevron area to the north is located at an altitude of 230–380 m, and the Salmchâteau at 480–570 m. The Mn-bearing sediments have undergone greenschist facies metamorphism in relation to the Caledonian and Variscan orogenesis, and more recently weathering processes, transforming the early mineral assemblages (mainly rhodochrosite and/or kutnohorite, spessartine, muscovite, chloritoïd, andalusite, hematite) into secondary Mn oxides,—hydroxides and—oxyhydroxides (cryptomelane, nsutite, lithiophorite, manganite, pyrolusite), clays (mainly kaolinite) and Fe oxides (goethite). In this paper, we investigate the weathering processes of these Mn-rich rocks by i) new mineralogical, petrographical and geochemical data, and ii) new $^{40}Ar/^{39}Ar$ geochronology of K-Mn oxides.

Petrographical and geochemical data indicate that rhodochrosite (and/or kutnohorite) is the main source of Mn, from which Mn oxides have precipitated. Spessartine and other Mn-silicates have poorly contributed to the Mn mobilization. Pure Mn oxides, namely manganite, nsutite, and pyrolusite, successively replace rhodochrosite under increasing O_2 conditions due to the weathering fluids, while the formation of cryptomelane and then lithiophorite in veins is associated to the recombination of K^+, Li^+ and Al^{3+} released from the phyllosilicate matrix of the host slate, probably in relation with sligh pH changes. This multistage character of weathering processes is well identified in the Salmchâteau area, where weathering conditions are stronger than in the Chevron area because of the elevation. This also positions the Mn levels close to the roll front within the lower saprolite and the fissured horizon, respectively. Such differences in the weathering grade of these areas determined a weathering-type deposit in the Salmchâteau area and a carbonate-hosted sedimentary deposit in the Chevron area. Weathering deposits are accompanied by an enrichment in Mn and associated transition metals (As, Co, Cu, Ni). Dating of pure cryptomelane samples corroborate the multistage character of the ore and yield at least four weathering stages: Chattian (26.33 ± 0.17 Ma), Aquitanian (22.2 ± 0.6 and 20.0 ± 0.2 Ma), Serravalian-Tortonian (11.79 ± 0.10 to 10.12 ± 0.18 Ma) and Pliocene or younger (5.30 ± 0.76 and 4.11 ± 0.57 Ma). A relatively continuous weathering of the Massif since the late Oligocene, or older weathering phases, cannot be excluded as the upper part of the saprolite (and laterite) have been removed. As climatic conditions evolve from tropical to temperate by the Oligocene, the uplift of the Ardenne is probably the main factor triggering the development of weathering mantle, together with the increasing seasonality and high precipitation. These ages with others obtained in supergene ores of Western European massifs define a long-

lasting weathering wave since the late Oligocene until the uppermost Neogene. The absence of older periods in the $^{40}Ar/^{39}Ar$ record of these deposits indicates that the upper part of the weathering mantle was recently stripped and limit their economic interest.

1. Introduction

Intense and long-term chemical weathering and related supergene enrichment processes have produced numerous economic manganese ore deposits worldwide (e.g., Kuleshov, 2016; Maynard, 2010; Varentsov, 1996). Supergene Mn oxide deposits typically form in humid tropical or subtropical zones where tectonic movements are slow (Kuleshov, 2016; Varentsov, 1996; Vasconcelos, 1999; Vasconcelos et al., 2018). They are commonly related to thick weathering of Mn-bearing minerals (e.g., rhodochrosite, kutnohorite, Mn-bearing calcite and silicates) able to provide Mn and other metals to form various Mn oxides -hydroxides, -oxyhydroxides (here resumed as Mn oxides; Dekoninck et al., 2016b, 2016a; Gutzmer et al., 2012; Verhaert et al., 2018) and silicates. These supergene deposits are generally high in Mn grades and constitute an important source through the world (e.g., Laznicka, 1992; Maynard, 2010). Additionnaly, manganese deposits formed during weathering record the chemical modifications of the host rock, the timing of weathering, if K-bearing Mn oxides are present (Vasconcelos, 1999), a condition generally met in weathered Mn-rich rocks. Hollandite group minerals [(K,Ba,Pb,Na)Mn$_8$O$_{16}$] (Biagioni et al., 2013) are among the most common minerals in supergene Mn deposits that could contain between 0.5% and 5% of potassium hosted in structural channels; these phases are therefore suitable for K-Ar and $^{40}Ar/^{39}Ar$ dating. $^{40}Ar/^{39}Ar$ dating is a powerful tool to determine the timing of a weathering profile, as the methodology provides control over the ages obtained by their evolution through the release of K-derived ^{39}Ar during the step-heating procedure (Ruffet et al., 1996; Vasconcelos, 1999; Vasconcelos et al., 1992).

In Western Europe, several locations contain terrestrial Fe-Mn deposits originating from supergene processes (Fig. 1; Dill et al., 2008). Five genetic types (Hunsrück-type; Bottke, 1969; Dill, 2010) were determined by Dill (1985a): (i) ferricretes *s.s.*, (ii) pebble iron ores, (iii) ferruginous conglomerates and breccias (chanel deposit), (iv) carbonate replacement ores, and (v) limonitic gossan of vein type deposits. These
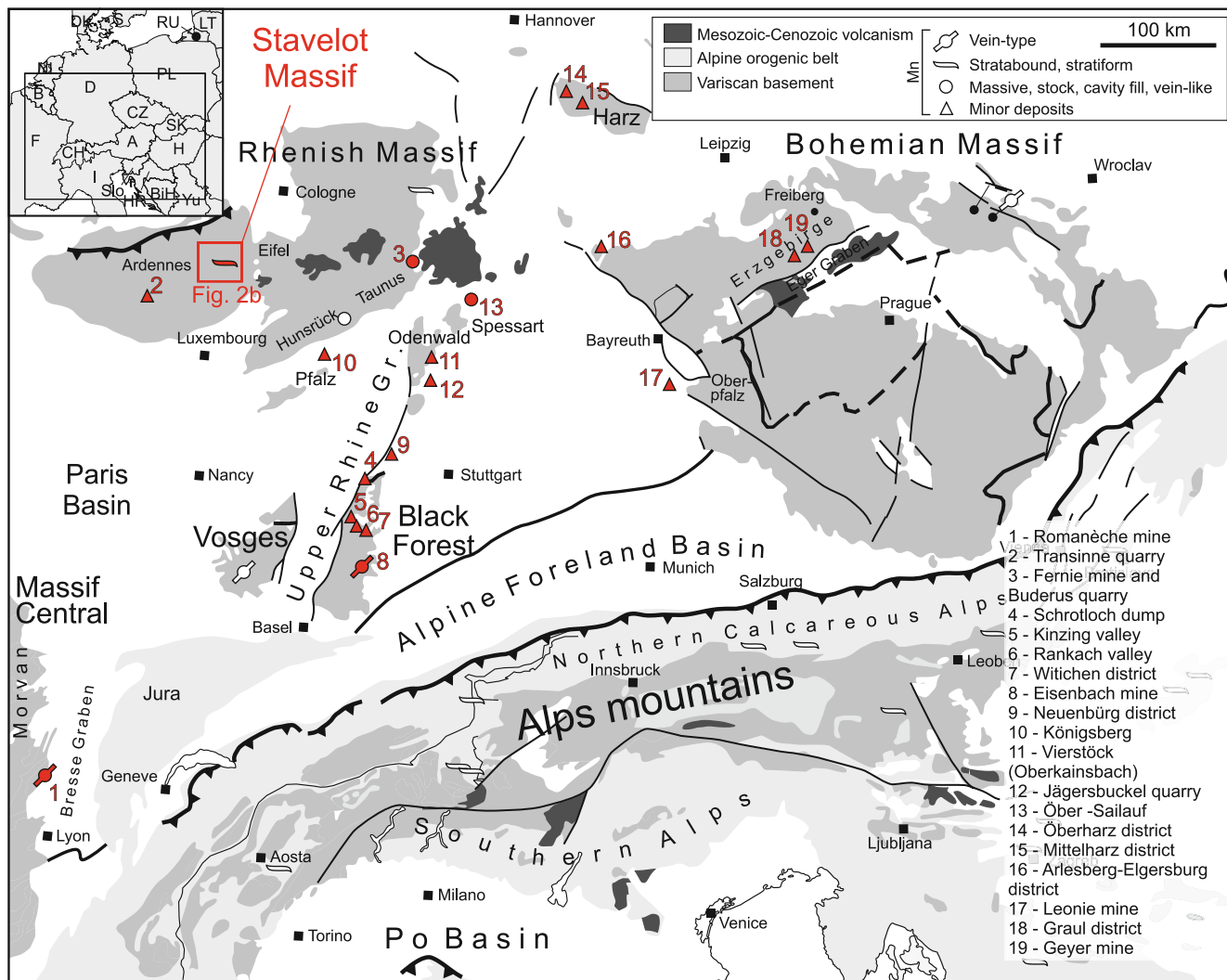

Fig. 1. Location of the Stavelot Massif (Ardenne, Rhenish Massif) in the major geological units of Central Europe (modified after Dill et al., 2008). Red symbols correspond to Mn deposits where $^{40}Ar/^{39}Ar$ are available. See Table 1 for reference number. (For interpretation of the references to color in this figure legend, the reader is referred to the web version of this article.)

Table 1

^{40}Ar/^{39}Ar ages of differnet Western European massifs. See Fig. 1 for location (with reference list number).

Sample label	Dated mineral	Location	Massif	Age (Ma)	Error (Ma)	Reference	Reference list
RF1-ke	romanechite	Romanèche mine	Massif Central	25.78	0.38	Hautmann and Lippolt (2000)	1
RF4b-k	romanechite	Romanèche mine	Massif Central	24.92	0.39	Hautmann and Lippolt (2000)	1
RF4a1-k	romanechite	Romanèche mine	Massif Central	20.9	0.73	Hautmann and Lippolt (2000)	1
RF4a2-k	romanechite	Romanèche mine	Massif Central	20.76	0.6	Hautmann and Lippolt (2000)	1
CRY-1B (g697)	cryptomelane	Transinnes quarry	Rhenish Massif (Ardenne)	21.54	0.45	Yans (2003)	2
WZ1a	cryptomelane	Fernie mine and Buderus quarry	Rhenish Massif	20.79	0.38	Hautmann and Lippolt (2000)	3
LM1	cryptomelane	Fernie mine and Buderus quarry	Rhenish Massif	18.6	0.19	Hautmann and Lippolt (2000)	3
SL2	hollandite	Schrotloch dump (Hornisgrinde)	Black Forest	6.99	0.23	Hautmann and Lippolt (2000), Wernicke and Lippolt (1995)	4
SB1-k	cryptomelane	Kinzing valley	Black Forest	12.58	0.07	Hautmann and Lippolt (2000)	5
CL13	hollandite	Rankach valley	Black Forest	13.66	1.84	Hautmann and Lippolt (2000)	6
CL13-T	hollandite	Rankach valley	Black Forest	13.52	1.35	Hautmann and Lippolt (2000)	6
CL12	hollandite	Rankach valley	Black Forest	7.38	0.64	Hautmann and Lippolt (2000)	6
GBF1	hollandite	Witichen district	Black Forest	1	0.1	Hautmann and Lippolt (2000)	7
BW6a	hollandite	Eisenbach	Black Forest	10.94	0.28	Hautmann and Lippolt (2000)	8
RL1c-k	hollandite	Eisenbach	Black Forest	9.51	0.06	Hautmann and Lippolt (2000)	8
VHR1-k	cryptomelane	Neuenbürg district	Black Forest	14.62	0.11	Hautmann and Lippolt (2000)	9
HH23	cryptomelane	Neuenbürg district	Black Forest	7.41	0.05	Hautmann and Lippolt (2000)	9
PM2-k	hollandite	Königsberg (Wolfstein)	Pfalz	9.58	0.28	Hautmann and Lippolt (2000)	10
PM1b	hollandite	Königsberg (Wolfstein)	Pfalz	8.96	0.05	Hautmann and Lippolt (2000)	10
PM1	hollandite	Königsberg (Wolfstein)	Pfalz	8.86	0.03	Hautmann and Lippolt (2000)	10
OK2-2	romanechite	Vierstöck (Oberkainsbach)	Odenwald	22.69	0.4	Hautmann and Lippolt (2000)	11
FB1	romanechite	Jägersbuckel quarry (Finkenbach valley)	Odenwald	22.87	0.49	Hautmann and Lippolt (2000)	12
SA15-k	cryptomelane	Ober-Sailauf	Spessart	10.92	0.03	Hautmann and Lippolt (2000)	13
SA4d-k	cryptomelane	Ober-Sailauf	Spessart	1.48	0.01	Hautmann and Lippolt (2000)	13
GT1	cryptomelane	Oberharz district (Gegental-Lautenthal)	Harz	2.59	0.04	Hautmann and Lippolt (2000)	14
GT1n	cryptomelane	Oberharz district (Gegental-Lautenthal)	Harz	2.52	0.02	Hautmann and Lippolt (2000)	14
BL1	cryptomelane	Mittelharz district (Braunstein)	Harz	19.62	0.1	Hautmann and Lippolt (2000)	15
IM1	hollandite	Öhrenstock area (Ilmenau South)	Bohemian Massif (Thüringer Wald)	7.46	0.17	Hautmann and Lippolt (2000)	16
Ar2d	hollandite	Arlesberg-Elgersburg district	Bohemian Massif (Thüringer Wald)	7.22	0.07	Hautmann and Lippolt (2000)	16
EB7	hollandite	Arlesberg-Elgersburg district	Bohemian Massif (Thüringer Wald)	7.19	1.14	Hautmann and Lippolt (2000)	16
Ar2d-T	hollandite	Arlesberg-Elgersburg district	Bohemian Massif (Thüringer Wald)	7.12	0.05	Hautmann and Lippolt (2000)	16
WT1-k	cryptomelane	Öhrenstock area (Ilmenau South)	Bohemian Massif (Thüringer Wald)	0.75	0.2	Hautmann and Lippolt (2000)	16
AB1	cryptomelane	Leonie mine (Auerbach)	Bohemian Massif (Oberpfalz)	14.73	0.3	Hautmann and Lippolt (2000)	17
SE1	romanechite	Graul district (Schwarzenberg)	Bohemian Massif (Erzgebirge)	18.22	0.49	Hautmann and Lippolt (2000)	18
GE1	cryptomelane	Amethyst pit (Geyer)	Bohemian Massif (Erzgebirge)	7.05	0.09	Hautmann and Lippolt (2000)	19
CRY-4 (g698)	cryptomelane	Bihain	Rhenish Massif (Ardenne)	25.06	0.88	Yans (2003)	
CRY-5 (g699)	cryptomelane	Bihain	Rhenish Massif (Ardenne)	21.1	0.3	Yans (2003)	
CRY-6 (g700)	cryptomelane	Bihain	Rhenish Massif (Ardenne)	22.2	0.6	Yans (2003), Demoulin et al. (2018)	
CRY-7 (g702)	cryptomelane	Bihain	Rhenish Massif (Ardenne)	20	0.2	Yans (2003), Demoulin et al. (2018)	

secondary Fe-Mn enrichments were controlled by the host-rock lithology, the local and regional geomorphology and the Cenozoic climatic conditions (Dill, 1985a). The ages recovered from K-Mn oxides in several of these massifs mostly delimit a Neogene period for weathering (see Table 1 for ^{40}Ar/^{39}Ar ages; Barbier et al., 2010; Brannath and Smykatz-Kloss, 1992; Bruyère et al., 2003; Demoulin et al., 2018, 2010; Dill, 1985b; Dill et al., 2010; Dill and Wemmer, 2012; Hautmann and Lippolt, 2000; Segev et al., 1992, 1991; Thiry et al., 2006; Yans, 2003).

The Ardenne Massif is located on the western side of the Rhenish Massif (Fig. 1) and documents widely preserved weathering profiles, up to 80 m thick, on Paleozoic sediments (Thiry et al., 2006; Yans et al., 2003). The bedrock underwent a long evolution under tropical conditions (Demoulin et al., 2018). Stratigraphic arguments (age of the cover, tectonics) defined these periods in and around the Ardenne (Dejonghe and Boni, 2005; Dusar and Lagrou, 2007; Quesnel, 2003; Yans, 2003; Yans et al., 2003), but the timing and the duration require careful attention as datable material is often missing between the host rock formation and the cover of the saprolite. In the Stavelot massif (Eastern Belgium, Fig. 2a and b), the Ottré Formation (Salm Group, Lower to Middle Ordovician) is mainly composed of Mn- and Fe-rich red to purple pelitic rocks corresponding to the Les Plattes and Meuville Members (Fig. 2b). These levels are known worldwide for their coticule layers, a metasedimentary yellowish rock composed of fine-grained Mn-garnet (spessartine), quartz and white micas (Baijot et al., 2011; Herbosch et al., 2016; Lamens and Geukens, 1984). These strata have undergone strong weathering leading to the formation of supergene manganese oxides (Blondieau, 2019, 2006, 2005; Fransolet, 1979; Gustine, 2002; Schreyer et al., 2001). The investigation proposed here focuses on the characterization and timing of weathering processes in these sediments in order to integrate them into the large scale weathering phases in Belgium and foreign areas.
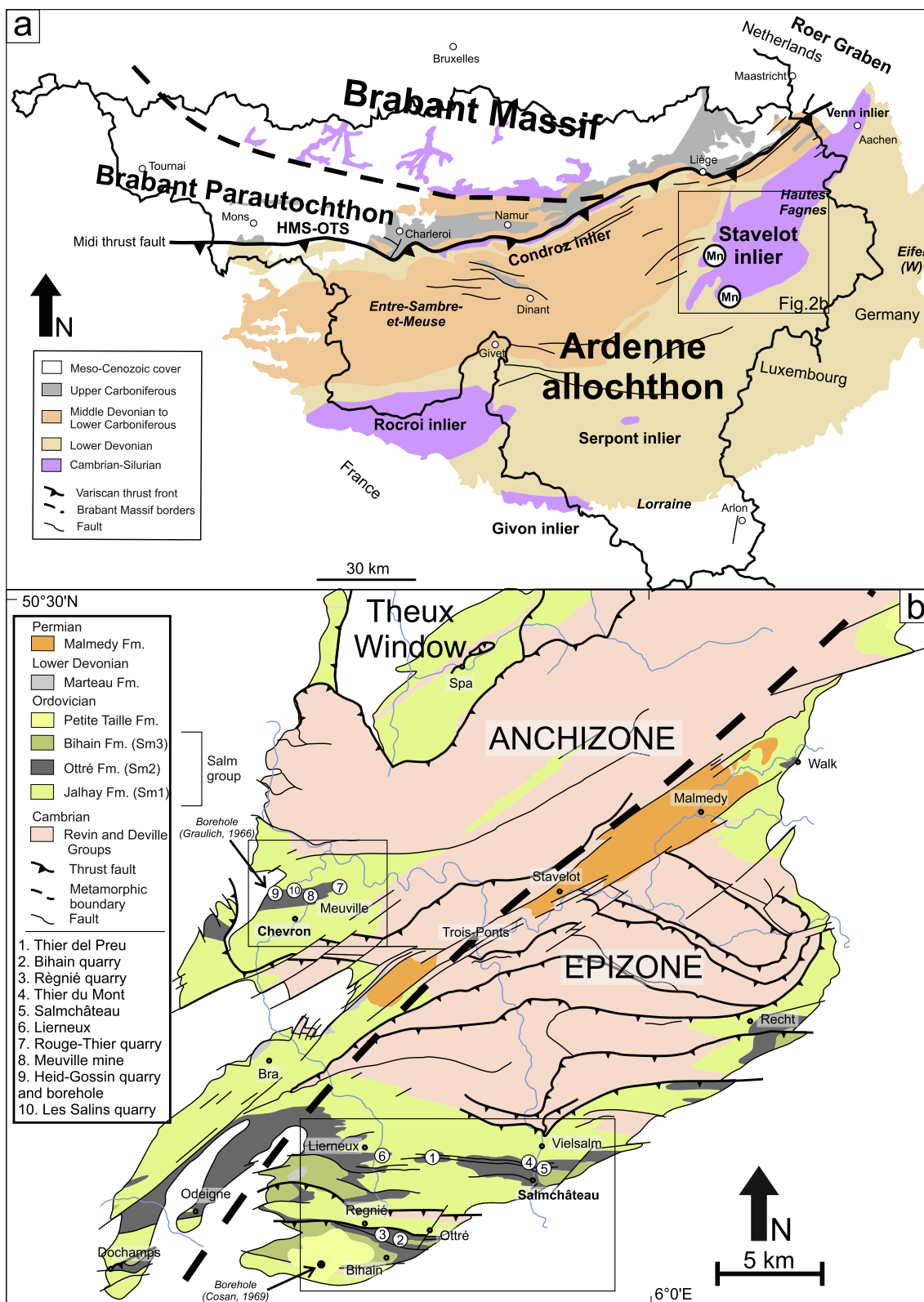
Fig. 2. a) Simplified geological map of southern Belgium showing the major structural units and the location of the Stavelot inlier on the eastern edge of the Ardenne allochthon (modified after Herbosch et al., 2016). b) Simplified geological map of the Stavelot Massif (after Geukens, 1999, 1986) showing the Ottré Formation containing the Fe-Mn-rich slates and coticule layers. Sampling sites are located in the main Mn ores and indicated by numbers from 1 to 10. Also shown are two metamorphic zones separated by the Malmedy graben.

2. Regional settings of the Ardennes and Stavelot massifs

2.1. Geological features

The Stavelot Massif belongs to the Ardenne region, which is part of the Rheno-hercynian fold-and-thrust belt (Fig. 2a and b). This massif extends into Germany (Venn Massif) to the east (Fig. 2a). These locations are often considered together and compose the eastern part of the Ardenne allochthon (Fielitz and Mansy, 1999; Oncken et al., 1999). This inlier is situated in the northwestern part end of the Rhenish Massif (Fig. 1) and has undergone Variscan folding and Late Carboniferous very low (anchizone) to low-grade (epizone) metamorphism (Fielitz and Mansy, 1999; Theye et al., 1996). Caledonian folding is recorded by an unconformity between the Stavelot inlier and the overlying Lower Devonian series (Adams and Vandenberghe, 1999; Hance et al., 1999).

The Cambrian-Ordovician succession of the Stavelot Massif is a continuous, mainly terrigenous sedimentary succession (Verniers et al., 2001), with minor volcanic events (Kramm and Bühl, 1985; Lamens and Geukens, 1984). The stratigraphy is subdivided into three groups (Geukens, 1999; Verniers et al., 2001; von Hoegen et al., 1985, Fig. 2b): (1) the Deville Group (400–600 m, Lower Cambrian), (2) the Revin Group (1900 m, Middle to Upper Cambrian) and (3) the Salm Group (900–1200 m, Lower and Middle Ordovician). Special care has been taken to the Salm Group as it contains Mn-rich sediments mined during the last centuries (Goemaere et al., 2016). This group is a thick series of terrigenous rocks subdivided into three Formations (Fig. 2b). The Jalhay Formation (Sm1) corresponds to a turbidite sequence evolving into wavy bedded siltstones and then to greenish slates and siltstones. The Ottré Formation (Sm2) is mainly composed of Fe- and Mn-rich red to purple pelitic rocks. Three members are distinguished (Geukens, 1999; Lamens, 1986, Fig. 3a): the Meuville Member (Sm2a, 60–80 m thick), the Les Plattes Member (Sm2b, 0–50 m thick) and the Colanhan Member (Sm2c, 50–100 m thick). Their precise age is unknown as stratigraphic microfossils are lacking due to their relatively high

oxidizing depositional environment. However, the occurrence of condonts at the boundary between the Meuville and Les Plattes members in the Chevron area gives an Early Ordovician, tentatively the latest Tremadocian age, even if a Floian age cannot be excluded (Vanguestaine et al., 2004). The Ottré Formation was probably deposited between 478 and 467 Ma (Herbosch et al., 2016). The upper Bihain Formation (Sm3) is composed of black silty slates and greenish sandstones containing pyrite and showing evidence of bioturbation. The Salm Group ends with the Petites Tailles Formation, a quartzite sandstone, which is often brecciated and composed of bedded chloritic slates and conglomerate sandstone with greenish shale pebbles. Lochkovian conglomerate of the Marteau Formation overlies, in angular unconformity, the Lower Paleozoic units (Hance et al., 1992; Vandenven, 1991, Fig. 2b).

2.2. Structure and tectonic of the Stavelot Massif

The Massif is strongly tectonized by both the Caledonian and the Variscan orogenic cycles, although the main features of the Caledonian deformation is still a matter of debate (Ferket et al., 1998; Piessens and Sintubin, 1997; Sintubin et al., 2009). Two main structural domains can be distinguished (Geukens, 1999, 1986; Fig. 2b). A northern domain consists mainly of rocks of the Revin Group showing a succession of closed synclinal structures interpreted to be Variscan (Hance et al., 1999; Mansy et al., 1999). Brittle tectonics overprinted earlier Caledonian east–west oriented structures. The southern part of the Massif, where the Ottré Formation outcrops in the Salmchâteau syncline and in the Recht area, records an epizonal low-grade metamorphism, while the northern part of the massif corresponds to an anchizonal metamorphism (Fig. 2b, Ferket et al., 1998). These two structural domains are separated by a N50°E oriented graben filled by Permian conglomerates (Geukens, 1975, 1957), delimiting two metamorphic zones. The metamorphic p-T conditions of the epizone are estimated between 400 and 450 °C, and 2 to 3 kbar, based on the presence of Mn-andalusite,
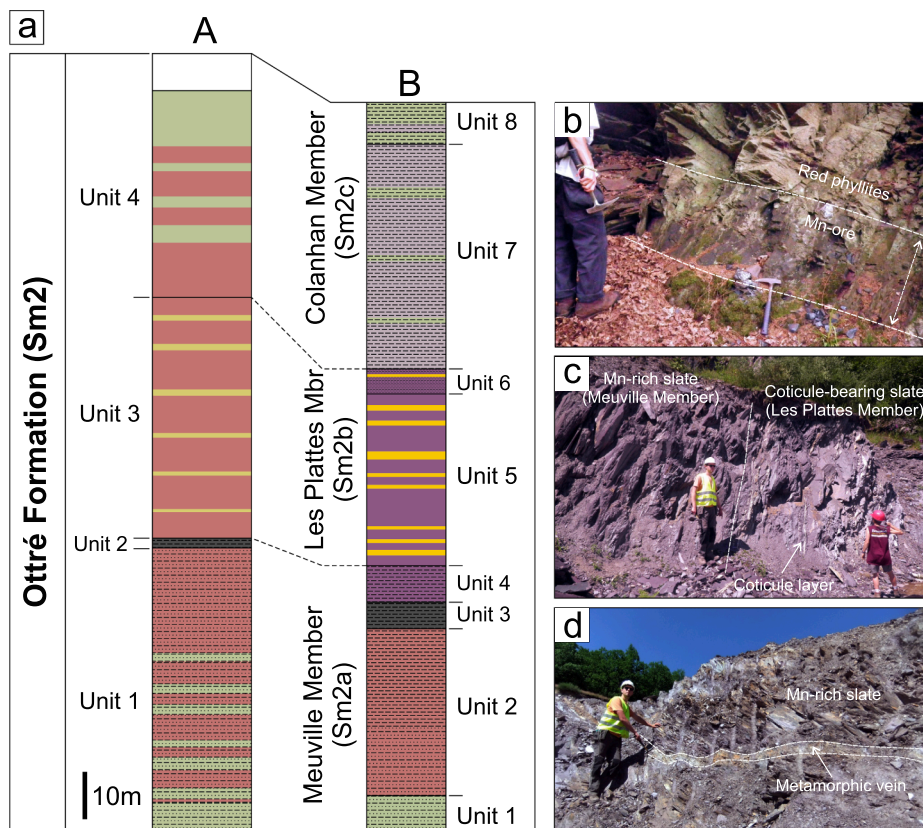

Fig. 3. a) Lithostratigraphic log of the Ottré Formation members and their correlation between the Chevron (A) and Salmchâteau (B) areas (Herbosch et al., 2016; Lamens, 1985b). See text and Herbosch et al. (2016) for the description of lithology. Mn ores are evidenced in dark gray and coticule layers in yellow. b) Mn ore level interbedded in the red phyllites in the Chevron area (Meuville mine, Unit 4). c) Limit between the Mn-rich purple slates of the Meuville Member (Unit 4) and coticule-bearing strata of the Les Plattes Member (Unit 5) in the Thier del Preu quarry (see Fig. 2b for location). d) Quartz-pyrophyllite-andalusite metamorphic veins crossing the Mn-rich dark slates (Unit 3) in the Thier del Preu quarry (see Fig. 2b for location). (For interpretation of the references to color in this figure legend, the reader is referred to the web version of this article.)

Mn-chloritoid, spessartine and muscovite, which corresponds to a greenschist-facies (Ferket et al., 1998; Fielitz and Mansy, 1999; Schreyer et al., 2004). The occurrence of carpholite and sursassite, instead of andalusite in the northern domain (Chevron area), implies p-T conditions of about 300 °C and 1 to 2 kbar (Fransolet et al., 2007; Theye et al., 1996).

The relative tectonic stability during the Mesozoic is inverted in the Upper Cretaceous, resulting in the subsidence of the northern part of the Ardenne Massif and the tilt from south to north (Demoulin, 1995a). The Cenozoic evolution of the Ardenne poorly records the effect of the Alpine orogenic cycle as folding is not observed (e.g., Demoulin, 1995b). However, beyond local tectonics, broad scale differential deformation suggests that every particular uplift episode of the massif during the Cenozoic did not exceed a few hundred meters with respect to the foreland (Demoulin et al., 2018). The age of the planation surfaces and the remains of Paleocene and Late Cretaceous sediments led Demoulin (1995a) to conclude that Tertiary uplift of the Ardennes started with large scale tilting during Paleocene, after a very long period of tectonic quiescence and even potential Jurassic cover (Barbarand et al., 2018). This is well demonstrated by a tilt between the pre-Senonian and Danian paleosurfaces (Demoulin et al., 2018) and hiatus in the Danian chalk (Boulvain and Vandenberghe, 2018). This was followed by a doming event during the Eocene, responsible for 200 m heights cumulated between the Selandian and Rupelian (Demoulin et al., 2018). This tectonic rearrangement is interpreted to be a response to the Pyrenean deformation pulse at the end of the Eocene (Boulvain and Vandenberghe, 2018), but also in relation to the dawn of the Lower Rhine rift activity (Roer Valley Graben) at least in the North (Demoulin et al., 2018, Figs. 1 and 2a). The major doming of the Ardennes started at the Late Oligocene, after the Early Oligocene transgression, continued during Neogene and accelerated at the Pliocene (Demoulin, 1995a). This acceleration uplift is evidenced by river terraces during Middle Pleistocene and a deep incision of the valleys (e.g., Garcia-Castellanos et al., 2000; Meyer and Stets, 1998; Van Balen et al., 2000).

2.3. Weathering of the Ardenne Massif

During Mesozoic and Cenozoic times, the Ardenne underwent many phases of exposure, only interrupted by marine transgressions onto the borders (Demoulin, 1995a; Demoulin et al., 2018) or above the massif itself (Barbarand et al., 2018). The most significant sedimentation episodes occured in the Triassic, Jurassic, Eocene and Early Oligocene. Therefore, some periods of exposure favored the setting up of widely preserved saprolites with thickness varying strongly from a place to another (Mees and Stoops, 1999). The age of these weathering periods is particularly well documented in kaolinic saprolites developed on Paleozoic sediments. Four periods record such events in and around the Ardenne Massif, namely during the Permian-Triassic, in the Early Cretaceous (extending in the "middle" Cretaceous), the late Paleocene/early Eocene and the Early Miocene (e.g., Demoulin et al., 2018; Thiry et al., 2006; Yans, 2003; Yans et al., 2003). This first weathering period is identified in the Lower Devonian bedrock in southern Belgium (Lorraine) and Malmedy area (Stavelot Massif), where kaolin deposits are covered by Permo-Triassic Formations (Boulvain et al., 2000; Geukens, 1975; Stoops, 1962), indicating a weathering and erosion phase at least older than Permo-Triassic (Fig. 2b). A long phase of weathering and kaolinization of the northern part of the Ardenne, which affected the Paleozoic basement of the Brabant Massif, started in the Early Cretaceous and continued up until the Cenomanian along the southern margin of the massif and into the Santonian or later along its northern margin (Dusar and Lagrou, 2007). However, weathering periods are mostly post-Maastrichtian in central Ardenne, post-Eocene in the Condroz and Entre-Sambre-et-Meuse, whereas the south has been exposed only since the Quaternary as interpreted by Alexandre and Thorez (1995; Fig. 2a). Following these authors, the prevailing effect of

the wet and warm Eocene climate would have developed weathering profiles, some of them being inherited from Mesozoic-Cenozoic periods, as recently confirmed by geochronological data (Barbier et al., 2010; Demoulin et al., 2018; Thiry et al., 2006; Yans, 2003; Yans et al., 2003).

Two major planation surfaces shaped the Ardennian landscapes: (1) the oldest one experienced several periods of weathering and denudation at higher elevation, whereas (2) the youngest, lower lying surfaces, only record Neogene weathering phases. Seven generations of paleolandscapes were identified (Demoulin, 2003, 1995b). However, connecting the development of weathering mantles with specific planation surfaces remains challenging, as weathering is often a long-term process resulting from the accumulation of different phases. A sedimentary cover is not always observed to delimit the timing of a planation surface and the weathering profile is often stripped and affected by successive erosion phases. Therefore, remains of intense weathering are only evidenced in plateaus (Alexandre and Thorez, 1995).

A pre-Triassic topography is observed in Western Eifel and continued westward by the so-called post-Variscan peneplain. However, Demoulin et al. (2018) indicated that the oldest preserved surface of the Ardenne is pre-Senonian and culminates at 650–700 m in the Stavelot Massif. This paleosurface is evidenced by a tilt (~1.4%) of Senonian sediments (clays and sands) toward the NNW over the bedrock and the presence of early Late Cretaceous pockets of clays within Dinantian limestones. Pre-Senonian surfaces experienced strong post-planation deformation during the Cenozoic, mainly in the form of differential uplift of the Hautes-Fagnes delimited by flexures on its northern and southern sides, whereas a series of Variscan faults were reactivated and accommodated the ~100 m height difference with the ridges. Some K-Ar ages recovered from neoformed Mn oxides in dissolution pockets yielded Late Cretaceous ages (88 to 95 Ma; Demoulin et al., 2010).

Post-Cretaceous acyclic erosion phases removed almost completely the Cretaceous cover and caused an extensive erosion surface during the Danian. This surface represents the end product of the long-lasting acyclic evolution of the Ardenne under conditions of prevailing tectonic stability along the Mesozoic. The Mn-Fe mineralization (580–600 m) lies below this erosion surface in the Salmchâteau area (Fig. 2b).

New paleosurfaces developed at the expense of the older ones from the middle Paleocene (Selandian surface), mainly in relation to the tilt of the Ardenne, which may be the result of the distant effect of the Alpine orogenesis (Xu et al., 2009). These new surfaces created scarps (~70 m) and produced stepped landscapes in response of this tilt. This happened first on the western side of the massif during the Selandian, until this surface was buried by the Early Thanetian sea to the west (Demoulin et al., 2018). The weathering mantle could be thick (~65 m in Transinne, 445 m asl) and also preserves late Cretaceous weathering phases in the upper part, and Miocene ages in the lower part of the profile (Yans, 2003; Yans et al., 2003). The middle part of the weathering profile of the Morialmé quarry (260 m asl) preserves Eocene ages between ~51 and 61 Ma (Barbier et al., 2010). This shows that weathering was still active before the Late Paleocene to Early Eocene sedimentation (Demoulin et al., 2018).

A new uplift of the Massif is responsible for new surfaces along the northern and southern sides of the Ardenne by the Late Eocene (pre-Oligocene surface), delimiting ~170 m scarps near the Danian surface. This surface is also found in the Paris Basin further west with elevations at ~300–420 m asl. Although the age of this surface is still debated, ranging between upper Eocene to Miocene (Demoulin, 2006; Quesnel, 2003), it is clear that there is no relation with the Plio-Quaternary differential uplift (Demoulin et al., 2018). The Oligocene-Miocene evolution is restricted to the development of intramontane planation basins of limited extent, owing to climatic conditions less favorable to chemical weathering (Demoulin et al., 2018). The Early Miocene age of this surface is supported by (i) the absence of Paleogene marine deposits and (ii) the evidence of the last phase of active bedrock kaolinization around 20 Ma based on K-Ar and $^{40}Ar/^{39}Ar$ dating of cryptomelane at the base of the weathering mantle at Transinne and Plateau

des Tailles (west of Bihain – see location in Fig. 2b; Demoulin et al., 2018; Thiry et al., 2006; Yans, 2003). The Beez quarry (~160 m asl) exposes cryptokarst formation, in which K-Ar dating of jarosite also provided Miocene ages (~17–18 Ma) for the weathering of the Visean limestones.

The Plio-Quaternary uplift of the Ardenne did not provide such well-developed weathering profiles as climatic conditions were less favourable and that the strong uplift resulted in the ~150 m incision of the valleys (Demoulin, 2018).

Although the Ardennian saprolites were developed by ferrallitic processes under climates warmer (and more humid) than present, the ferruginous upper part of the profile (laterite *sensu* Nahon, 1991) was mostly removed by erosion of the uplifted plateaus. The weathering profiles are only preserved in scattered places (Théveniaut et al., 2007), where uninterrupted Mesozoic and Cenozoic tectonic stability strongly limited denudation (Barbarand et al., 2018). Weathering profiles are thicker, more important and frequent in high elevation areas (> 500 m). Their size and frequency decrease progressively to be very scarce and small in dimensions under 340–360 m (Alexandre and Thorez, 1995). Therefore, the Ardenne preserves the most important weathered rocks with thickness of 20 to 65 m (Alexandre and Thorez, 1995; Dupuis et al., 1996; Gullentops, 1954), and up to 50 in the Stavelot Massif (NE of Ardenne; Cosan, 1969; Fig. 2b). Paleozoic quartzite and slates are respectively weathered into sands and clays, the latter being dominated by kaolinite and illite (Alexandre and Thorez, 1995), together with Fe- and Mn oxides, -hydroxides and -oxyhydroxides. The only remaining evidences are the roots of these profiles (Alexandre and Thorez, 1995; Cosan, 1969). The borehole of Brackvenn in the northern part of the Stavelot Massif (Fig. 2b) indicates a (pre-)Cretaceous weathering period, as the Paleozoic weathered rocks are covered by Maastrichtian chalk deposits. However, the depth of 22.5 m thick saprolite differs from those observed in the same area with only few meters in thickness (Alexandre and Thorez, 1995).

3. The Fe-Mn levels

The main manganese ores of Belgium are located in the southern part of the Stavelot Massif in the red to purple slates of the Meuville Member (Salm Group, Ottré Formation, Fig. 2b and 3). These manganese ores were mined for desulfurization component in the manufacturing of cast iron (Goemaere et al., 2016) periodically between 1886 and 1934 in the Chevron area (Berger, 1965), from which 180,000 tonnes of ore was produced (Dejonghe, 1985; Dussart and Dussart, 1991; Libert, 1905). However, most of the manganese levels were mined for the cm-size coticule whetstones in the Salmchâteau area within the Les Plattes Member (Fig. 3a, Herbosch et al., 2016). Note that coticule layers cannot be considered as a manganese ore, because they are mined for the production of whetstone. No coticule has ever been exploited in the Chevron zone, as the composition of the yellow levels differs too much from those of the southern part (Fig. 3a). The underlying Mn ore was mined for Mn ores in many places in the Salmchâteau area (Goemaere et al., 2016 and reference therein), but also as a by-product of coticule mining in Thier del Preu quarry, mainly assigned to the manufacture of black ceramic products (Herbosch et al., 2016). Two other places expose the Ottré Formation in the eastern part of the Massif, east of the village of Recht, and near Walk (Fig. 2b). In the Odeigne-Doschamps strips, where the Ottré Formation is widely exposed, coticule has never been observed (Dejonghe, 2008; Geukens, 1986; Lamens, 1985a, 1986), as well as in the German northeast part (Echle et al., 1985; Meyer and Walter, 1985, Fig. 2b).

3.1. Stratigraphic position of the Mn ores

The Mn-rich sediments are located in the upper part of the Meuville member, whereas coticule layers are enclosed in the Les Plattes Member (Fig. 3a). The latter consists of red slates interbedded with cm-size coticule beds. The thickness of the Les Plattes Member is variable, which corresponds to important variations in its paleogeographic distribution (Herbosch et al., 2016). The thickness of 40–45 m observed in Salmchâteau decreases rapidly to < 10 m in Lierneux, vanishing toward the west of Regné (Lamens, 1985a; Lamens et al., 1986). This member also thins toward the north-northeast from 30 to 35 m in Recht, to only a few meters in Walk (Herbosch et al., 2016, 2016; Fig. 2). In the Chevron syncline, the Meuville and Les Plattes Members reach 47–52 m in thickness (Graulich, 1966; Lamens, 1985a; Fig. 3a).

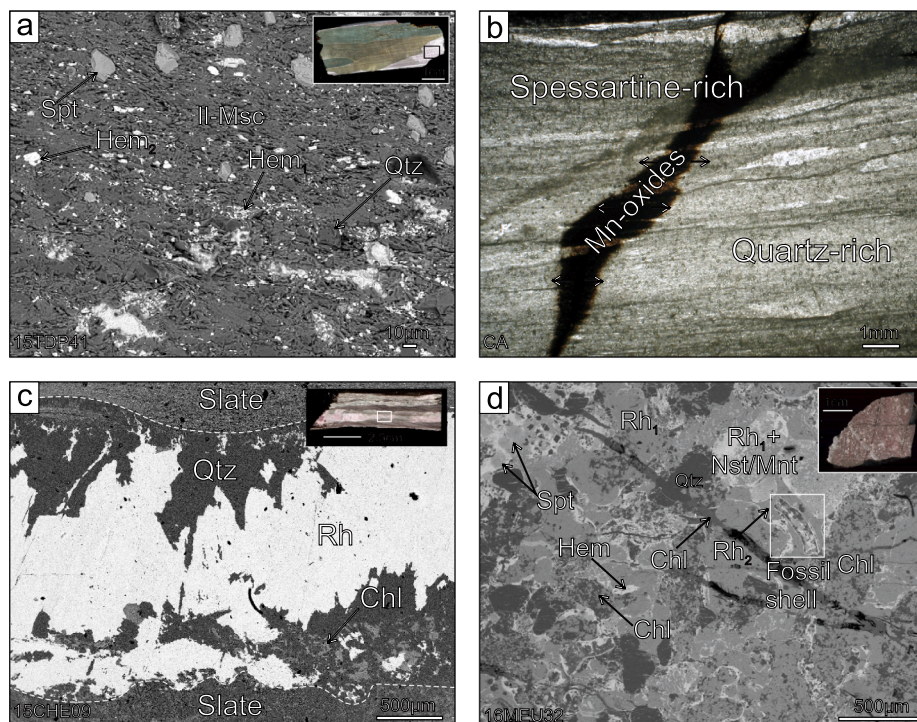The manganese ores are quite different between the two locations.

Fig. 4. Petrographic features of the unweathered Mn-rich levels and coticule. a) Back-scattered electron view of disseminated spessartine and hematite in the micaceous purple slate (Units 3–4) in the Thier del Preu quarry. b) Transmitted light view of a coticule level showing the variation in the spessartine-quartz composition in Thier del Preu quarry. Coticule is crossed by a Mn oxide vein forming a dark halo into the coticule level. c) Back-scattered electron view of red phyllites showing rhodochrosite-quartz lenses formed during diagenesis-metamorphism in the Heid-Gossin borehole (Graulich, 1966). d) Back-scattered electron view of the Mn ore (Unit 4) in the Meuville mine showing rhodochrosite nodules (Rh$_1$) cemented by a second generation of rhodochrosite (Rh$_2$) together with quartz, spessartine, hematite and chlorite. Fossil shell remains into the Mn ore evidence the sedimentary feature of this level. Hem: hematite; Il: illite; Musc: muscovite; Qtz: quartz; spt: spessartine; Rh: rhodochrosite; Chl: chlorite; Nst: nsutite; Mnt: manganite. (For interpretation of the references to color in this figure legend, the reader is referred to the web version of this article.)

In the Chevron area, the ore is mostly a carbonate-bearing assemblage of poorly weathered metamorphic minerals. A mixture of coarse rhodochrosite and spessartine (0.05 to 0.2 mm) is associated with quartz, chlorite and hematite, forming a massive dark purple rock (Fig. 3b). The Salmchâteau Mn ore consists of purple slates replaced by secondary Mn oxides, which originate from weathering of the host slates (Fig. 3c). Some Mn oxides in the Salmchâteau area could also have a hypogene origin, as demonstrated by hollandite-strontiomelane association in quartz veins with kanonaite and braunite (Schreyer et al., 2001; Fig. 3d). Muscovite, hematite, spessartine, Mn-chloritoïde, quartz and accessory minerals are remaining minerals of the enclosing slates.

3.1.1. Salmchâteau area

The red slates are composed of fine-grained micas, quartz and hematite with small amounts of spessartine, andalusite and kaolinite blasts (Lamens et al., 1986). Lamens (1985a, 1985b) described in detail the lithological succession of the Ottré Formation in the Vielsalm and Salmchâteau section. This author subdivided the Ottré Formation in 8 Units distributed into three members (from base to top of the Ottré Formation; Fig. 3a). The Meuville Member comprises Units 1 to 4 and is composed of red slates rich in hematite and spessartine. The base of Unit 1 is marked by a characteristic chloritoïd-rich quartzite bed (Geukens, 1965). Unit 2 contains red slates with some beds rich in 50–100 μm spessartine porphyroblasts (Herbosch, 1965; Nicaise, 1985). The occurrence of large poikiloblasts (0.5–5 mm) of rhodochrosite in Unit 3 has led the level to be considered as the main Mn ore level of the southern area. Unit 4 also contains hematite-spessartine-bearing violet slates, but with common mm-scale spots of kaolinite and/or andalusite (Theunissen, 1971), which are sometimes replaced by massive purple slates rich in hematite, kanonaite and braunite (Herbosch, 1967; Schreyer et al., 2004, 2001). The Les Plattes Member consists of purple slate interbedded with mm to cm size dominantly yellowish folded coticule. Unit 5 contains most of the minable coticule-bearing strata and differs from Unit 6 by the occurrence of chloritoïd porphyroblasts instead of spessartine. Finally, units 7 and 8 characterize the Colanhan Member with purple and green chloritoïd-rich slates containing "pseudocoticule" layers characterized by large spessartine garnets enclosed in a quartz matrix (Baijot et al., 2011).

Purple slates show very regular millimeter-scale laminations corresponding to small variations in the terrigeneous influx. Some of these beds are light-colored and thus richer in quartz, while other darker laminae are very rich in hematite. Two major forms of hematite are recognized: (1) as a very fine micron-size dust dispersed within the phyllosilicate matrix and (2) as a more concentrated form with 10–50 μm-size crystals in dark laminae (Fig. 4a). The spessartine content is quite variable in the purple slates, ranging from absent to 10–15% in laminae (Fig. 4a), and even more abundant near dark hematite laminae. Hematite content is highly variable but relatively abundant in unit 5 (3.58–20.9% wt., mean = 13.4% wt. Fe_2O_3), while FeO is very low (0.2–0.7% wt., mean = 0.32% wt. FeO; Herbosch et al., 2016). Manganese is generally less abundant than iron in the slates (0.46–14.8% wt., Mean = 3.86% wt. MnO) due to the presence of disseminated crystals of spessartine. Mn content decreases strongly in the chloritoïd-slates of Unit 6 (0.65–1.4% wt., mean = 0.89% wt. MnO) due to the absence of Mn-garnet (Herbosch et al., 2016). The mean mineralogical composition of these slates is 38% phyllosilicates, 26% quartz, 14% hematite, 13% andalusite-kaolinite spots, 4% chlorite and 3% spessartine (Lamens, 1985a) close to that of the coticule layers composition (Kramm, 1976; Krosse and Schreyer, 1993).

The contact of purple slates with enclosed coticule is usually sharp in Les Plattes Member. Coticule layer composition is usually 39% of 1 to 5 μm (sometime 25 μm) spessartine, 28% quartz, 24% phyllosilicates, 3% chlorite and 3% of other minerals (hematite, chloritoïd, kaolinite, andalusite, rutile, tourmaline (Lamens, 1985b). Kramm (1976), Lamens (1985a) and more recently Herbosch et al. (2016) subdivided coticule veins in five types, depending on their chemical or mineralogical

composition and texture. Sometimes, these coticules are found as mm-size globules in the red slates (Schreyer et al., 1992). Coticule layers are even more folded or micro-folded than the host-slates, and most of these structures are attributed to metamorphism. However, some sedimentary or diagenetic features such as load casts, ball and pillow, flames or flute mark structures can be found when the purple enclosing slates are regularly laminated (Lamens et al., 1986), led Herbosch et al. (2016) to interpret coticule layers as distal turbidites. The evolution from quartz-rich, to spessartine-rich coticule from the base to the top of a single layer corroborates the sedimentary deposition (Fig. 4b, Lamens et al., 1986), as well as the lateral extension of coticule-bearing slates, which is estimated to be at least 5 to 6 km (Herbosch et al., 2016). The geochemical contact between the slates and the coticule strata is sharp, showing a reverse evolution between Fe_2O_3 and MnO content: Fe_2O_3 content decreases progressively from the slates to the outer rim of the coticule layers, whereas MnO increases, and reach a maximum peak inside the coticule that overtakes the Fe_2O_3 content. FeO is low in both coticules and slates (Kramm, 1976). Coticule chemical composition is enriched in MnO (0.8–22.8% wt., mean = 9.83% wt. MnO) and poor in Fe_2O_3 (0.3–4.34% wt., mean = 0.3% wt. Fe_2O_3), as spessartine is very common and hematite is often depleted. However, pseudocoticule layers in the Colanhan Member (at the top of the Les Plattes Member, unit 6) shows higher manganese (8.6–25.4% wt., mean = 16.6% wt. MnO) and iron contents than other coticules (2.7–5.5% wt., mean = 3.59% wt. Fe_2O_3), which might be related to the higher amounts of hematite (Baijot et al., 2011).

3.1.2. Chevron area

Lamens (1985b) recognized four lithological units of the Ottré Formation, corroborated by the borehole drilled on the western side of the Chevron syncline (Graulich, 1966; Fig. 2b). The lower unit C1 is a red laminated siltstone with some intercalation of green siltstones and red hematite-rich phyllites in the upper part. Rhodochrosite clearly occurs in lenticular forms, following the stratification of the slate (Fig. 4c). Unit C2 corresponds to the main Fe-Mn ore bodies 1 to 3 m in thickness (Fig. 3b). On the western side of the Chevron area, C2 unit is only 0.7 cm thick (Graulich, 1966; Fig. 2b). The manganese level consists of interbedded red phyllites, siltstone and coarse-grained beds 1–20 cm thick. The coarse beds are composed of 1–5 mm fossils (rhodochrosite echinoderm fragments, oncolites, elongate apatite fossil remnants) and rock fragments (mudstone, quartzite, well-rounded quartz, volcanic material) embedded in hematite, spessartine, chlorite and a rhodochrosite-rich matrix (Fig. 4d) associated with scarce siderite and pyrolusite (Berger, 1965). Carbonate is nearly pure rhodochrosite (Berger, 1965) to kutnohorite (Theye et al., 1996). Units C1 and C2 are considered as the lateral equivalent of the Meuville Member (Lamens, 1985a, 1985b). Unit C3 is a 45 m thick succession of red slates (quartz, muscovite, paragonite, hematite and rhodochrosite) alternating with whitish, greenish or pinkish beds (phyllosilicates, quartz, spessartine and scarce hematite) 1–10 cm thick, attributed to the Les Plattes Member coticule-bearing strata (Lamens, 1985b). Rhodochrosite spherules are dispersed or concentrated in nodules or as lenticular beds 0.5–3 cm thick (Fig. 4c). The 45 m thick unit C4 shows red and green silty slates without any rhodochrosite, and is considered as the equivalent of the Colanhan Member (Lamens, 1985b). These metapelites often show intensive veining, which includes deposition of centimeter size quartz, hematite and rhodochrosite, indicating local migration of manganese during metamorphism. Manganese carbonates are partly replaced by spessartine and chlorite (Fig. 4d, Theye et al., 1996).

3.2. Origin, formation and evolution of the Fe-Mn-rich sediments

Several models have been proposed for the origin of the Mn-rich slates and coticule levels, and all consider a protolith deposited in a basin then subjected to diagenesis and later metamorphism. The slates

and coticules from the Les Plattes Member were deposited in a small basin of about 40–50 km from north to south (currently 20 km) and 25 km for its east–west extension, delimited by Chevron to the north-west, Walk and Recht to the northeast and Bihain-Ottré to the south (Fig. 2b, Herbosch et al., 2016). This basin was fed to the north by the emerged Brabant Massif (Fig. 2a, Herbosch and Verniers, 2014, 2013; Linnemann et al., 2012) during the drifting of Avalonia from Gondwana and the consequent opening of the Rheic Ocean (Cocks and Fortey, 2009; Cocks and Torsvik, 2002; Torsvik et al., 2012). Kramm (1976) first proposed a volcanoclastic model for the coticule, successively refined by Kramm (1980) and Krosse and Schreyer (1993) involving a hydrothermal origin for manganese and iron given the geochemical data. However, coticule and adjacent slates represent two different sedimentary processes, as the slates were deposited in a quiet, deep and O_2-rich environment, and coticule in a deep but high-energy environments (Herbosch et al., 2016; Lamens et al., 1986). This has led Lamens et al. (1986) to suggest that coticule layers were water-oversaturated limy mud sediments rapidly deposited under high-energy conditions, whereas the purple slates originated from slow sedimentation of suspended clay, silt and Fe-Mn particles. Herbosch et al. (2016) recently improved the density current model, in particular the paleogeography of those sediments. The enrichment of Fe and Mn is related to the flocculation of Fe and Mn particles coming from hydrothermal vents in the mid-ocean spreading ridge of the Rheic Ocean. The *in situ* precipitation of dissolved Mn^{2+} and Fe^{2+} from seawater is, however, difficult to entail but probably that early sedimentary Mn oxides or hydroxides are the earliest minerals hosting the Mn and associated metals following the model of Johnson et al. (2016). The protore of the coticule was deposited in a deep oceanic basin as limy mud turbidites, which is enriched in Mn during early diagenesis by replacement of calcium by manganese through diffusion of divalent manganese from the enclosing Fe-Mn-rich slates to form rhodochrosite (Herbosch et al., 2016). Alternativelly, microbially-mediated rhodochrosite formation is also likely (Maynard, 2014), as well as other diagenetic Mn-bearing silicates (Johnson et al., 2016). Processes of Mn precipitation in sediments are also summarized in Maynard (2014). The Mn-slates, rich in spessartine and hematite, were formed when the terrigenous input was low, and/or when the hydrothermal flux was high. This density current model is responsible for the rapid deposition of the coticule protolith and the dilution of the Fe-Mn compounds, compared with the enclosing slates.

Metamorphic transformations of the former shales of the Ottré Formation has led to the formation of slates and quartz veins containing spessartine, Mn-chloritoïd, andalusite-kanonaite, pyrophyllite, paragonite, kaolinite and chlorite in the southern area. Spessartine crystallization resulted from the recombination of elements contained in rhodochrosite and clay minerals in both coticule and slates (Lamens et al., 1986). This could explains the mineralogical difference between the spessartine content in the epizone (Salmchâteau), and rhodochrosite in the anchizone (Chevron). However, this metamorphic reaction is nearly complete as both spessartine and rhodochrosite occur together in the Chevron area.

4. Material and methods

We have focused our investigations on the Salmchâteau (Thier del Preu quarry, Bihain quarry, Règnié quarry, Thier du Mont and Salmchâteau) and Chevron areas (Rouge-Thier quarry, Meuville mine, borehole 159 W1215, Heid-Gossin quarry and "Les Salins" quarry), where Les Plattes and Meuville Members crop out (Fig. 2b). More than one-hundred samples were collected on the field or taken from the collections of the Geological Service of Belgium and from the Laboratory of Mineralogy, University of Liège. From these samples, twenty-six geochemical analyses were performed for major and trace elements (Tables 2 and 3) and thirteen $^{40}Ar/^{39}Ar$ ages were obtained from K-Mn oxides (Table 4). All these samples were analyzed for their mineralogy

using XRD patterns. Additionally, twenty-four polished sections and twenty-two thin sections were prepared.

4.1. Mineralogical and petrological preparations

XRD analyses of powdered samples were performed using X-ray Panalytical X'Pert Pro diffractometer and a PHILLIPS PW3710 (CuKα radiation) at the PC2 platform (UNamur), operating at 40 kV and 30 mA. Major mineral phases were identified using the ICDD View software with PDF-2 data base (Powder Diffraction File 2009). Samples were crushed to powder in stainless steel grinding jar, introduced in a RETSCHER PM 100 planetary ball mills and sieved to 125 μm before their analysis.

Thin and polished sections were respectively prepared at the Sedimentary Petrology unit of the Geology Department at the University of Liège (Belgium), and in the G-Time laboratory of the University of Brussels (Belgium). Both sections were studied by light microscopy, and some of them by a JEOL 7500-F Scanning Electron Microscope coupled with an ULTRA MINI-CUP Energy Dispersive Spectrometer hosted at the Microscopy Service of the University of Namur.

4.2. Geochemistry

Geochemical analyses were carried out at the Activation Laboratories Ltd (Actlabs, Ontario, Canada). Crushing was performed with a RETSCH PM 100 planetary ball mills (University of Namur) in order to obtain the maximum 125 μm grain size. REEs and trace elements were analyzed by Fusion Mass Spectrometry (FUS-MS) and major elements by Fusion Inductively Coupled Plasma Optical Emission Spectrometry (FUS-ICP). FeO was quantified by titration. Trace elements V, Sr, Zr, and Ba were determined with FUS-ICP. For samples presenting high contents of Li, Cu, Pb, Zn, V, Ag, Mo, In, and Sb, analyses were carried out by Fusion Inductively Coupled Plasma Sodium Peroxide Oxidation (FUS-Na_2O_2) and Inductively Coupled Plasma Optical Emission Spectrometry (ICP-OES). Major elements of the mineralized samples are compared and normalized to the average slate composition of unit 5 summarized in Herbosch et al. (2016) in order to emphasize the enrichment and depletion of these elements during weathering. Considering the sedimentary nature of the Mn-rich slates, and the lack of some metal average in the Unit 5 slate of Herbosch et al. (2016), REE and trace elements are normalized to the Upper Crust (McLennan, 2001). Trace elements are ordered depending on their mobility during weathering and their LILE or HFSE nature. Ca, Na, Mg, Ba, K, P, V, U, Sr are considered as mobile elements along a weathering profile, while Zr, Hf, Ti, Al, Fe, Mn, Sc, Th, Nb, Sc and REEs are immobile elements (Carroll, 1970; Ma and Liu, 1999; Middelburg et al., 1988).

4.3. $^{40}Ar/^{39}Ar$ dating

One major difficulty in dating supergene K-Mn oxides arises from contamination of the samples by the older parental material, providing mixing and geologically meaningless or uninterpretable ages (Vasconcelos, 1999). This is especially the case considering the large amount of K-bearing minerals (muscovite, illite) in the host Ordovician phyllites. Mn oxide impregnations in the host phyllites are of low purity and poor crystallinity, and are therefore not considered for dating. Only pure K-Mn oxide veins were selected in order to avoid any contamination. These samples do not show botryoidal and banded textures, as it is generally the case in most of supergene manganese deposits (Dekoninck et al., 2016b, 2016a). This means that K-Mn oxides would record a single weathering phase, and not a succession of stages.

The studied samples were collected in Thier del Preu (15TDP25, TDPR-003) and Bihain quarries (15HEB01, 15HEB03, BIHD-009, BH311, BH11b), which are respectively located at 490 m and 570 m of

Table 2

Major oxides (in wt. %) and minor element (in ppm) geochemical analyses. LOI: Lost on ignition. Mineral abbreviation: spt = spessartine, qtz = quartz, musc = muscovite, lith = lithiophorite, cry = cryptomelane, hem = hematite, ppl = pyrophyllite, chl = chlorite, and = andalusite, rh = rhodochrosite, nst = nsutite, mnt = manganite, prl = pyrolusite, chd = chloritoïd, fds = feldspar, goe = goethite, kaol = kaolinite.

Label	Mineralogy	Rock type	Outcrop	SiO$_2$	Al$_2$O$_3$	Fe$_2$O$_{3(T)}$	MnO	MgO	CaO	Na$_2$O	K$_2$O	TiO$_2$	P$_2$O$_5$	LOI	Total
15RN01	spt, qtz, musc	Coticule	3	48.46	18.99	1.2	26.42	0.62	0.4	0.39	1.37	1.042	0.07	1.43	100.4
CA	qtz, spt, musc, lith, cry	Coticule (weathered)	3	52.56	16.98	1.06	24.81	0.36	0.42	0.35	1.07	0.927	0.07	1.56	100.2
15RN04	spt, musc, qtz, hem, ppl	Coticule (weathered)	3	46.77	19.97	8.43	16.92	0.54	0.26	0.71	2.3	1.084	0.12	3.31	100.4
15RN05	qtz, ppl, chl, and	Metamorphic vein	3	78.25	17.31	0.46	0.04	0.44	0.03	0.12	0.18	0.004	< 0.01	3.1	99.92
16CHE01	rh, qtz, chl	Metamorphic vein	9	48.12	0.71	1.27	29.24	0.38	1.77	< 0.01	0.03	0.006	0.02	17.06	98.62
16MEU34	rh, qtz, hem, chl, musc	Metamorphic vein	8	27.15	6.61	26.72	24.05	1.26	1.88	0.17	0.48	0.3	0.43	9.21	98.26
16CHE08	nst, qz, mnt, prl	Metamorphic vein (weathered)	9	44.36	0.81	1.53	40.44	0.11	0.08	0.01	0.1	0.009	0.04	7.16	94.63
16MEU32	qtz, spt, chl, rh	Mn ore	8	31.46	8.55	30.07	21.11	0.93	1.81	0.31	0.6	0.486	0.53	4.35	100.2
16CHE09	qtz, hem, chl, rh	Mn ore	9	38.97	7.65	35.69	7.321	0.99	0.73	0.08	1.83	0.297	0.51	4.9	98.98
16MEU38	qtz, hem, rh, chl, spt	Mn ore (weathered)	10	37.78	5.61	38.24	9.372	0.79	1.09	0.42	0.97	0.259	0.44	5.07	100
RN838	cry, lith, nst	Mn oxide	6	1.45	4.86	1.02	60.93	0.06	0.25	0.28	0.69	0.03	0.5	15.91	86.01
RN859	cry	Mn oxide	6	0.23	1.01	0.5	65.99	0	0.19	0.4	1.14	0.004	0.67	12.92	83.06
RA8432	cry, qtz	Mn oxide	6	2.07	1.88	1.02	65.29	0.03	0.23	0.44	2.44	0.042	0.89	12.47	86.81
15HEB03	qtz, musc, hem, spt, cry, lith	Mn slate	2	51.91	18.47	12.78	5.392	0.27	0.08	1.2	3.15	0.82	0.12	4.3	98.47
15TDP07	qtz, musc, hem, spt, nst	Mn slate	1	43.88	17.53	20.89	7.099	1.06	0.42	0.68	2.88	0.76	0.19	4	99.39
16TDM10	qtz, musc, hem, chd	Mn slate	4	49.2	18.84	15.33	3.853	1.16	0.42	2.11	3.81	0.842	0.21	2.76	98.53
16MEU23	qtz, hem, musc, chl	Mn slate	8	38.45	14.87	36.54	0.322	0.76	0.37	0.64	2.63	0.628	0.26	3.09	98.56
16MEU33	qtz, hem, musc, chl, fds	Mn slate	8	63.27	7.7	20.4	1.412	1.18	0.31	0.65	1.64	0.826	0.14	1.82	99.34
16MEU03	qtz, chl, hem, musc	Mn slate	7	61.22	14.52	10.66	2.777	3.25	0.44	0.2	1.28	0.683	0.41	4.36	99.79
15TDP32	qtz, musc, hem, chl	Mn slate	1	51.42	22	12.44	1.228	2.18	0.32	0.97	3.24	1.025	0.21	4.1	99.14
16MEU01	qtz, musc, chl, hem	Mn slate	7	46.97	21.38	14.79	2.494	2.13	1.93	0.5	2.8	0.896	1.37	4.46	99.71
15HEB01	qtz, musc, hem, cry, lith	Weathered Mn slate	2	31.57	12.49	9.54	30.19	0.1	0.13	1.17	3.1	0.522	0.37	6.94	96.12
RA8431	qtz, musc, hem, cry	Weathered Mn slate	6	18.38	7.27	17.24	39.15	0.09	0.18	0.67	2.25	0.289	0.52	9.45	95.49
15TDP12	musc, qtz, cry, hem, lith	Weathered Mn slate	1	36.82	17.49	17.48	15.76	0.19	0.08	0.59	3.11	0.703	0.23	7.69	100.2
15TDP45	qtz, musc, kaol, hem, goe, lith, cry, spt	Weathered Mn slate	1	27.53	12.65	16.15	29.73	0.16	0.31	0.85	2.21	0.499	0.27	8.3	98.65
15TDP42	qtz, musc, spt, lith, cry, chl	Weathered Mn slate	1	39.35	15.56	14.05	17.2	0.24	0.14	0.51	2.86	0.667	0.28	7.67	98.51

Label	Li	Sc	Be	V	Cr	Co	Ni	Cu	Zn	Ga	Ge	As	Rb	Sr	Y	Zr	Nb	Mo
15RN01	20	24	2	188	110	36	30	20	30	20	22.7	56	65	124	45.2	142	15.9	8
CA	25	18	2	678	90	175	30	60	60	17	24.8	274	50	97	42.3	139	13.1	14
15RN04	33	28	3	141	130	359	60	70	40	25	12.8	84	104	232	68.2	166	18.1	15
15RN05	137	1	< 1	7	170	10	< 20	10	< 30	27	1.4	< 5	8	17	1.7	4	< 0.2	< 2
16CHE01	14	< 1	< 1	11	170	21	< 20	20	< 30	6	2.5	22	2	5	4.5	7	< 0.2	10
16MEU34	54	12	6	153	70	99	90	< 10	140	33	7	409	21	38	44	270	10.4	5
16CHE08	13	1	< 1	7	120	16	< 20	30	50	7	2.2	29	4	32	2.7	6	< 0.2	12
16MEU32	55	16	8	212	110	84	110	20	110	18	9.6	483	28	43	53.3	263	15.9	8
16CHE09	33	16	3	148	60	59	60	30	550	35	2.2	215	86	44	42.8	161	9.3	3
16MEU38	30	14	4	98	90	73	50	20	80	25	1.6	275	50	55	37.3	193	11.1	3
RN838	862	2	4	42	60	427	1000	290	1570	10	0.5	51	17	436	23.6	1	< 0.2	19
RN859	9	< 1	5	62	140	325	40	4190	950	10	1	61	14	717	17.7	< 1	< 0.2	22
RA8432	136	2	10	709	170	677	260	370	1110	12	0.5	156	38	2843	4.2	8	0.3	77
15HEB03	328	18	5	64	100	141	280	10	250	31	2.3	133	146	343	41.3	117	14	< 2
15TDP07	160	16	4	106	120	124	160	60	190	35	3.8	79	143	278	33.7	104	13.1	2
16TDM10	93	18	4	68	120	64	90	70	70	31	3.3	123	189	202	40.8	116	14.8	< 2
16MEU23	61	14	4	153	70	40	60	< 10	50	23	2	31	117	154	31.5	83	10.4	2
16MEU33	50	11	3	106	140	21	30	50	70	22	2	55	78	56	36.9	1490	11.5	8
16MEU03	159	14	2	87	80	119	90	440	220	24	3.8	10	54	68	44.3	104	11.2	< 2
15TDP32	100	20	4	105	100	82	90	30	140	34	2.1	195	152	284	38.5	133	15.8	4
16MEU01	105	21	4	128	90	89	90	80	130	32	3.7	16	118	120	62.6	140	15.3	< 2
15HEB01	99	12	3	47	90	92	80	850	370	21	3.4	140	106	516	37	73	9.4	9
RA8431	46	10	6	98	50	515	130	40	320	15	2.2	631	68	974	48.1	42	5.3	28
15TDP12	105	20	6	88	60	173	140	120	210	25	2.7	133	140	294	87	107	13	7
15TDP45	477	12	4	234	70	320	1350	120	1210	21	3.7	145	95	450	51.8	73	10.4	13
15TDP42	374	15	5	140	60	421	730	130	670	36	2.5	132	128	290	60.5	98	11.4	13

Label	Ag	Sn	Sb	Cs	Ba	Hf	Ta	W	Tl	Pb	Bi	Th	U
15RN01	< 0.5	3	2.8	4	434	4	1.33	21.4	0.13	26	< 0.1	12.8	3.1
CA	< 0.5	3	3.1	3.3	423	3.8	1.22	8	0.16	17	< 0.1	10.6	2.49
15RN04	< 0.5	4	3	6.3	881	4.3	4.26	20.2	0.37	39	1	15.5	4.11
15RN05	< 0.5	2	0.7	0.9	45	0.1	0.06	1.1	< 0.05	6	0.1	0.08	0.16
16CHE01	< 0.5	< 1	< 0.2	< 0.1	24	0.1	0.29	28.4	< 0.05	< 5	0.1	0.21	0.38
16MEU34	0.6	1	4.2	0.9	182	6.2	0.41	10.6	< 0.05	101	1.4	9.8	5.53
16CHE08	< 0.5	< 1	< 0.2	0.3	27	0.1	1.12	15	< 0.05	6	0.1	0.36	0.19
16MEU32	< 0.5	2	3.3	1	260	6.1	1.11	19.5	0.12	112	1.5	14.1	5.92
16CHE09	< 0.5	1	4.3	3.6	578	3.8	0.46	5.7	0.15	77	1.8	10.5	3.56
16MEU38	< 0.5	< 1	4.8	2.2	537	4.4	0.45	10.4	0.09	143	2.6	10.9	4.66
RN838	< 0.5	< 1	< 0.2	0.9	591	< 0.1	< 0.01	< 0.5	< 0.05	< 5	< 0.1	0.47	2.23
RN859	< 0.5	< 1	< 0.2	< 0.1	100	< 0.1	< 0.01	< 0.5	< 0.05	< 5	< 0.1	0.06	3.22

Table 2 (*continued*)

Label	Ag	Sn	Sb	Cs	Ba	Hf	Ta	W	Tl	Pb	Bi	Th	U
RA8432	< 0.5	< 1	2.2	0.4	439	0.2	0.19	9.9	< 0.05	< 5	< 0.1	0.82	22.5
15HEB03	< 0.5	3	6.4	12.6	973	3.2	1.05	4.5	0.52	59	0.3	12.8	1.84
15TDP07	< 0.5	3	3.7	9.3	962	2.7	0.94	4.6	0.44	52	0.5	11.6	1.79
16TDM10	< 0.5	3	4	18.9	1357	3.4	1.11	5.7	0.79	44	0.4	13	1.11
16MEU23	< 0.5	2	2.6	4.9	1009	2.3	0.81	5.1	0.39	73	1	10.3	2.02
16MEU33	4.3	2	2.9	3.3	545	35.2	1	5.2	0.2	80	0.6	21.3	3.93
16MEU03	< 0.5	2	1.8	2.4	497	2.8	0.83	5.1	0.16	24	0.2	9.53	1.7
15TDP32	< 0.5	4	4.2	6.5	1374	3.6	1.21	4.6	0.53	45	0.5	13.7	2.17
16MEU01	< 0.5	3	2.3	4.9	963	3.8	1.09	3.8	0.48	38	0.4	12.1	2.91
15HEB01	< 0.5	2	15.4	11.8	901	2.1	0.87	11.1	0.08	72	0.4	8.88	2.38
RA8431	< 0.5	3	1.7	4.7	3697	1.3	0.41	12.4	< 0.05	33	0.2	5.23	3.45
15TDP12	< 0.5	3	3	8.8	965	3	1.09	8.6	0.38	52	0.4	12	3.78
15TDP45	< 0.5	2	3.6	6.8	640	2	0.76	15.4	0.18	62	0.5	8.07	3.84
15TDP42	< 0.5	2	3.2	8.5	890	2.8	0.85	6.2	0.5	54	0.3	10.5	4.91

elevation. No elevation was available for samples RA8432, RA8433, RN859, as they were taken from the Belgium Geological Survey Desk (Lierneux location; Fig. 2b). K-Mn oxides are well crystallized and contain between 1 and 2 wt% of K_2O, without any Ba and Pb, indicating that these minerals are cryptomelane, despite the slight Cu, Co, Ni and Sr enrichment (Table 2).

All dated materials were hand-picked from crushed rocks, washed in distilled water and then treated in an ultrasonic bath and dried to avoid fine particles adsorbed on grain surfaces. The crystallinity, purity and composition of the samples were further determined by X-ray Diffraction (XRD), Energy Dispersive Spectrometry (EDX) and Scanning Electron Microscopy (SEM). Several grains from each sample were investigated with a JEOL 7500-F Scanning Electron Microscope coupled with an Energy Dispersive Spectrometer hosted at the Microscopy Service of the University of Namur.

$^{40}Ar/^{39}Ar$ analyses were conducted in the Noble Gas laboratory of Géosciences at the University of Montpellier 2, France, using a new generation multicollector mass spectrometer (Thermo Scientific Argus VI MS) with a nominal mass resolution of ~ 200 and a sensitivity for argon measurements of $3.55 \times 10{-}17$ mol/fA at 200 μA trap current. The mass spectrometer is equipped with a Nier-type source and a fixed array of five Faraday detectors and one Compact Discrete Dynode (CDD) detector. It is linked to a stainless steel gas extraction/purification line and CO_2 laser system for step-heating which produces, after focusing, a 1 mm diameter beam that is used for step heating. The samples selected for dating were irradiated for 40 h in the core of the Triga Mark II nuclear reactor of Pavia (Italy) with several aliquots of the Taylor Creek sanidine standard (28.34 ± 0.10 Ma) as flux monitor. Argon isotopic interferences on K and Ca were determined by irradiation of KF and CaF_2 pure salts from which the following correction factors were obtained: $(^{40}Ar/^{39}Ar)_K = 0.00969 \pm 0.00038$, $(^{38}Ar/^{39}Ar)_K = 0.01297 \pm 0.00045$, $(^{39}Ar/^{37}Ar)_{Ca} = 0.0007474 \pm 0.000021$ and $(^{36}Ar/^{37}Ar)_{Ca} = 0.000288 \pm 0.000016$. After loading in the sample chamber, the samples were baked at about 120 °C during 24 h to remove atmospheric argon from the sample surface. Air aliquots from the automated pipette system were analyzed prior to the sample analyses to monitor mass discrimination and detector bias. Line blanks were analyzed between every 3 sample analyses and were subtracted from succeeding sample data. Step-heating experiments on single grains were conducted with a duration of heating of

Table 3
Rare Earth Elements geochemistry (in ppm).

Label	La	Ce	Pr	Nd	Sm	Eu	Gd	Tb	Dy	Ho	Er	Tm	Yb	Lu	ΣREE	Ce_N/Ce_N*	Eu_N/Eu_N*	La_N/Lu_N
15RN01	43.9	94.6	9.74	38	15.2	8.75	15.7	1.96	8.92	1.46	3.8	0.573	3.82	0.609	247.03	1.04	2.66	1.03
CA	31.9	73	7.23	28	13.4	6.86	12.7	1.65	7.79	1.3	3.57	0.491	3.26	0.523	191.67	1.10	2.47	0.87
15RN04	56.7	147	13.1	48.4	13.8	5.17	16.7	2.63	13.6	2.42	6.31	0.912	5.75	0.854	333.35	1.23	1.60	0.95
15RN05	0.2	0.57	0.06	0.34	0.25	0.104	0.59	0.06	0.27	0.04	0.11	0.016	0.09	0.013	2.71	1.19	1.27	0.16
16CHE01	2.49	20.5	0.99	4.62	1.22	0.289	1.09	0.19	1.08	0.19	0.46	0.067	0.46	0.074	33.72	2.98	1.18	0.36
16MEU34	51.9	201	11.9	46.6	10.3	2.23	10	1.62	9.79	1.81	4.85	0.717	4.56	0.679	357.96	1.84	1.03	0.82
16CHE08	2.24	8.85	0.63	2.7	0.71	0.181	0.68	0.1	0.55	0.1	0.27	0.046	0.31	0.048	17.42	1.70	1.22	0.50
16MEU32	55.9	224	12.8	51.3	12.1	3	11.5	1.93	11.3	2.09	5.68	0.826	5.39	0.816	398.63	1.91	1.20	0.98
16CHE09	30.5	127	8.69	37.1	8.77	2.17	9.2	1.43	8.18	1.56	4.27	0.631	3.99	0.66	244.15	1.78	1.14	0.66
16MEU38	28.7	135	7.87	33.5	8.22	1.8	8.18	1.32	7.87	1.51	4.23	0.638	4.18	0.651	243.67	2.05	1.03	0.63
RN838	4.67	9.62	0.99	4.39	1.18	0.306	1.61	0.26	1.88	0.54	1.99	0.396	2.89	0.462	31.18	1.02	1.04	0.11
RN859	0.71	2.12	0.19	0.93	0.37	0.124	0.79	0.12	0.81	0.2	0.61	0.089	0.52	0.076	7.66	1.32	1.08	0.10
RA8432	3.67	10.9	0.88	3.75	1	0.251	1.2	0.16	0.85	0.15	0.41	0.057	0.41	0.065	23.75	1.38	1.08	0.60
15HEB03	55.8	138	12.6	47.1	8.84	1.85	7.38	1.25	7.53	1.48	4.01	0.582	3.8	0.608	290.83	1.19	1.08	0.98
15TDP07	61.2	144	13.3	49.3	9.41	2.2	8.85	1.27	6.86	1.22	3.3	0.471	2.95	0.446	304.78	1.15	1.13	1.46
16TDM10	63	172	14.1	53.5	9.97	2.28	8.77	1.37	7.91	1.52	4.24	0.592	3.92	0.618	343.79	1.32	1.15	1.09
16MEU23	47.5	127	11.2	43.1	9.94	2.36	8.47	1.24	6.84	1.27	3.34	0.469	2.95	0.455	266.13	1.26	1.21	1.11
16MEU33	48.6	109	12.4	49.3	10.4	1.58	9.33	1.35	7.43	1.3	3.62	0.547	3.81	0.596	259.26	1.01	0.75	0.87
16MEU03	44.3	105	10.3	40.2	8.18	1.98	8.21	1.37	8.39	1.63	4.48	0.648	3.82	0.625	239.13	1.12	1.14	0.76
15TDP32	55.3	130	12.3	45.8	8.72	1.62	7.02	1.23	7.39	1.36	3.74	0.518	3.28	0.493	278.77	1.14	0.97	1.20
16MEU01	76.5	185	17.1	66.8	13.8	3.39	13.1	2	11.5	2.17	6.04	0.862	5.29	0.776	404.33	1.17	1.18	1.05
15HEB01	42.8	140	10.2	39.8	8.44	1.91	7.31	1.14	6.39	1.24	3.51	0.507	3.12	0.481	266.85	1.53	1.14	0.95
RA8431	23.1	68	6.36	33.7	12.3	2.82	11.8	1.66	9.02	1.7	4.64	0.664	4.31	0.692	180.77	1.28	1.10	0.36
15TDP12	64.7	172	15.1	57.8	10.5	2.41	11.5	2.49	16.9	3.56	10.4	1.63	10.6	1.66	381.25	1.25	1.03	0.42
15TDP45	30.7	124	8.36	35.7	9.84	2.4	9.52	1.52	8.74	1.75	4.83	0.692	4.49	0.709	243.25	1.77	1.17	0.46
15TDP42	52.5	136	11.8	44.5	8.43	1.99	8.75	1.51	9.7	1.98	5.8	0.832	5.27	0.798	289.86	1.25	1.09	0.70

Table 4
Summary of $^{40}Ar/^{39}Ar$ ages of supergene K-Mn oxides in the Salmchâteau area. [a]: pseudo-plateau age; [+]: integrated age determined by less than 20% of ^{39}Ar released; n.a. : not applicable. [*] range of individual step-heating ages.

Label	Outcrop	Elevation	Plateau age (Ma)	± 2σ	Total fusion age (Ma)	± 2σ	Isochron age (Ma)	± 2σ	Intercept $^{40}Ar/^{36}Ar$	± 2σ	MSWD (steps)	Comments
15TDP25a	Their del Preu quarry (1)	486 m	11.97[a]	0.31	11.60	0.20	14.33	3.59	−665.1	1480.8	0.27 (16 to 21)	Pseudo-plateau
15TDP25b		486 m	11.07[a]	0.30	11.07	0.30	9.50	3.49	687.2	877.2	5.93 (7 to 9)	Pseudo-plateau
TDPR-003		480 m	17.66[a]	0.19	18.46	0.11	19.68	1.09	−247.1	291.5	11.07 (24 to 30)	^{39}Ar recoil, excess argon, saddle shaped spectrum
15HEB01	Bihain quarry (2)	572 m	15.61[a]	0.16	16.83	0.10	15.55	0.76	302.6	102.5	17.89 (10 to 14)	^{39}Ar recoil, excess argon, saddle shaped spectrum
15HEB03		573 m	20.01[+]	0.34	33.30	0.24	n.a.	n.a.	n.a.	n.a.	n.a.	^{39}Ar recoil, excess argon, saddle shaped spectrum
BH311		570 m	11.43	0.08	11.38	0.07	11.23	0.22	335.7	43.0	9.94 (12 to 31)	Plateau
BH311b		570 m	11.79	0.10	11.69	0.11	12.14	0.39	152.1	143.4	13.27 (5 to 20)	Plateau
BIHD-009		570 m	26.83	0.20	26.33	0.17	25.98	1.74	412.2	238.5	2.10 (8 to 12)	Plateau
RA8432	Lierneux (6)	–	11.38[+]	0.25	14.26	0.08	10.68	1.51	355.6	128.4	0.16 (2 to 8)	Staircase spectrum
RA8433a		–	5.30[a]	0.76	4.92	0.65	5.04	1.67	296.4	5.1	1.41 (2 to11)	Recent ages
RA8433b		–	4.11[a]	0.57	3.02	0.36	2.74	2.03	305.1	13.9	1.15 (1 to 9)	Recent ages
RN859		–	11.74[+]	0.19	14.17	0.09	11.88	0.20	291.8	2.9	1.03 (1 to 8)	Staircase spectrum
Verleu 1399	Verleumont	–	10.12[+]	0.18	11.71	0.07	10.13	0.28	295.1	4.4	3.51 (1 to 12)	Staircase spectrum

45 s at each step. A custom-made software was used to control the laser intensity, the timing of extraction/purification and the data acquisition. The ArArCalc software© v2.5.2 (Koppers, 2002) was used for data reduction and plotting. All the data were corrected for system blanks, radioactive decay, isotopic interferences and mass discrimination. Atmospheric ^{40}Ar was estimated using a value of the initial $^{40}Ar/^{36}Ar$ ratio of 295.5. Plateau ages are defined as including > 50% of the total ^{39}Ar released, distributed over at least 3 contiguous steps, with $^{40}Ar*/^{39}Ar$ ratios within agreement of the means at the 95% confidence level. Calculated ages are reported at the 2σ level and include uncertainties in the J-values, but exclude errors associated with the age of the flux monitor and the decay constants.

5. Results

The purple and red slates of the Ottré Formation are weathered into a clayey rock containing Mn oxides. Despite this weathering is more intense in the Salmchâteau area compared to the Chevron area, it seems that the formation of supergene mineral assemblage is associated with the same process in both areas. Manganese oxides are known as early, middle and late weathering products of Mn carbonates and Mn-rich silicates. Their study requires careful attention as they are often mixed. The poor crystallinity of these minerals is also a feature which makes the study of Mn oxides often tricky. Therefore, the results presented here focus on the weathering mineral assemblages, first presenting the general mineralogy and petrography of the weathered manganiferous sediments and then the geochemistry of these weathered rocks. $^{40}Ar/^{39}Ar$ dating is presented separately.

5.1. Mineralogy of the weathered ores

As the Ottré Formation is particularly enriched in Fe and Mn, the secondary mineralogy resulting from weathering processes, is extensively dominated by the formation of Mn oxides, -hydroxides and -oxyhydroxides (here resumed as Mn oxides). Cryptomelane and nsutite are the most abundant minerals in the weathered manganese ores in the Salmchâteau and Chevron areas. Lithiophorite is often concentrated, and some other pure Mn oxides, such as manganite and pyrolusite could also be observed in some samples (Fig. 5a), together with clays (illite and kaolinite) and goethite.

Cryptomelane (KMn_8O_{16}), frequently used for $^{40}Ar/^{39}Ar$ dating, occurs as a deep black matrix, which is mixed with the enclosing red phyllites, often showing a homogeneous composition and sometimes the typical botryoidal habit composed of micrometric growth bands (Fig. 5b). The mineral typically displays a needle-like crystal, with each crystal being < 15 μm long and 0.5–1 μm in diameter (Fig. 5c). However, most of these crystals are difficult to identify because they are agglomerated in a dense and cryptocrystalline matrix as commonly observed in other places in the world (Decrée et al., 2010; Dekoninck et al., 2016a). This K-Mn oxide is identified by XRD (Fig. 5a) and SEM-EDS analyses (Fig. 5d) in almost all locations, but is abundant in Thier del Preu and Bihain quarries (Fig. 2b). The composition is nearly pure cryptomelane as Ba, Na and Pb are nearly absent, and K_2O composition ranges between 1.0 and 3.0 wt% in chemical and EDS analyses (Fig. 5d, Table 2). Slight enrichment in Al is frequently observed, as well as trace elements such as Co, Cu, Zn, Sr, P and Fe (this issue, Gustine, 2002). Inclusions of halite, hematite and zincite are also observed and could explain the enrichment in other metals.

Lithiophorite [(Al, Li) MnO_2 (OH)$_2$] occurs as small tabular crystals of < 10 μm long and 2 μm in diameter or as euhedral cubic crystals of 1–5 μm (Fig. 5e). However, lithiophorite is generally poorly crystalline forming a homogeneous matrix similar to that of cryptomelane. Micrometric bands are also observed in veins, and relate to the variation of lithiophorite composition, these containing few percent of Ca, K, P, Si, Co and Cu under EDS analyses, while Li is relatively low (800 ppm, Table 2). Small quantities of As-sulfate inclusions (undetermined) can
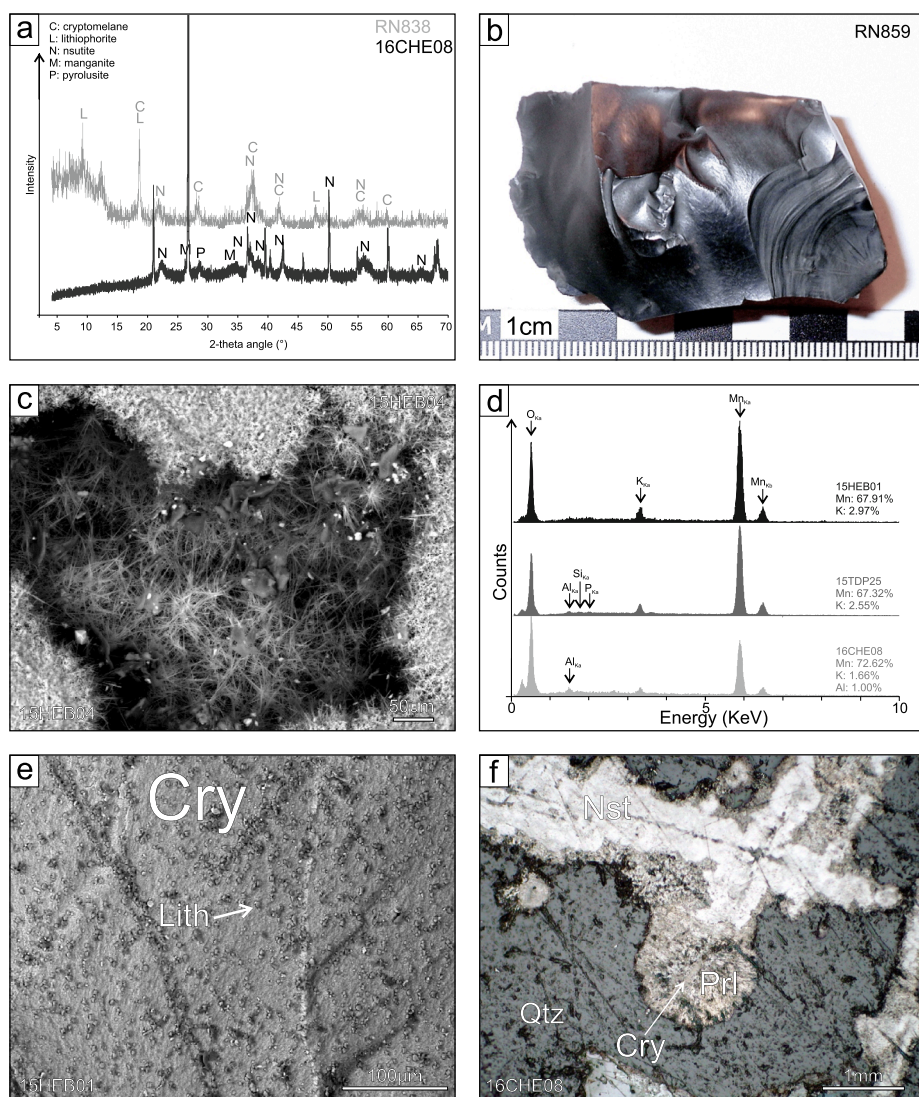
Fig. 5. Mineralogy of the Mn oxides. a) XRD pattern of two samples containing the dominant Mn oxide minerals. b) Pure cryptomelane sample showing the typical black color and colloform textures. c) Back-scattered electron view of cryptomelane needles in the Bihain quarry. d) Energy Dispersive Spectra (EDX) of three cryptomelane samples located in the Bihain quarry (15HEB01), Thier del Preu quarry (15TDP25) and Heid-Gossin quarry (16CHE08). The composition is nearly pure cryptomelane which can contain little amount of Al, Si and P. e) Back-scattered electron view of lithiophorite coating onto pure cryptomelane vein in the Bihain quarry. f) Reflected light view of nsutite, cryptomelane and tabular pyrolusite in the Heid-Gossin quarry. Cry: cryptomelane; Lith: lithiophorite; Nst: nsutite; Qtz: quartz; Prl: pyrolusite.

be found.

Pure cation-free Mn oxides are also present in the weathered ores. Manganite (MnOOH) and nsutite [Mn^{4+}, Mn^{2+}) $(O,OH)_2$] are clearly identified by XRD in weathered rhodochrosite veins of the Chevron area (Fig. 5a). These minerals are associated with pyrolusite (Fig. 5f, MnO_2). The presence of small quantities of pyrolusite is a common feature of these mineral associations as nsutite is considered as an intergrowth of cryptocrystalline ramsdellite and pyrolusite (Post, 1999). Pyrolusite is easily recognized by its coarse prismatic crystals 5–50 μm long and 1–15 μm wide and well-developed cleavages in Scanning Electron views. Petrographic features, such as high reflectivity, yellow reflection color, well-developed bireflection, and strong anisotropism, makes it easily recognizable under an optical microscope (Fig. 5f). The determination of nsutite is more complicated in light and scanning electron microscopy because of the similar features with other cation-free Mn oxides (Fig. 5f). Although their composition contains only Mn and O in energy disspersive spectra, manganite is darker than nsutite in back-scattered electron views, this feature being related to the heavier average molecular mass of nsutite than manganite, when these minerals occur together. These three Mn oxides are often associated with Mn ores worldwide and commonly form from oxidation of Mn carbonates (Post, 1999).

Hematite and goethite are extensively disseminated in the host slates, the latter giving yellow to brown tints to the weathered host slates (Fig. 6a). Hematite (Fig. 4a) follows the stratification. Its presence

in the weathered slates is due to the relative stability of hematite after supergene conditions. This could explain why goethite is relatively rare in most of the sampling sites, as Fe remains hosted in the hematite structure, even so botryoidal goethite is observed filling voids in the host slates and where Mn oxides are highly concentrated (Fig. 6b). This goethite is characterized by Mn, P and Al substitutions to Fe^{3+}. Undetermined Fe-Mn oxides are also detected in some samples and could be a mixture of Fe oxides and Mn oxides.

Secondary clay minerals widely occur in the form of illite, as a replacement for the former muscovite present in the manganiferous slates. Kaolinite is also identified as filling voids of the dissolved rhodochrosite and a weathering product of the slates. Chlorite is present in some levels of the host slates and in quartz veins. However, its formation is most likely related to metamorphic conditions rather than supergene transformation. Their chemical composition allows the distinction of two chlorites, one being Mg-rich and the other Fe-rich. Most of these chlorites contain small amounts of Mn (1–10%) in their structure.

5.2. Petrographic features of the weathered ores

In order to deal with the petrography of the weathered ore, we consider the Salmchâteau area (south) and the Chevron area (north) separately, because (1) they underwent weathering processes with variable intensity, and (2) the primary Mn-bearing assemblage is
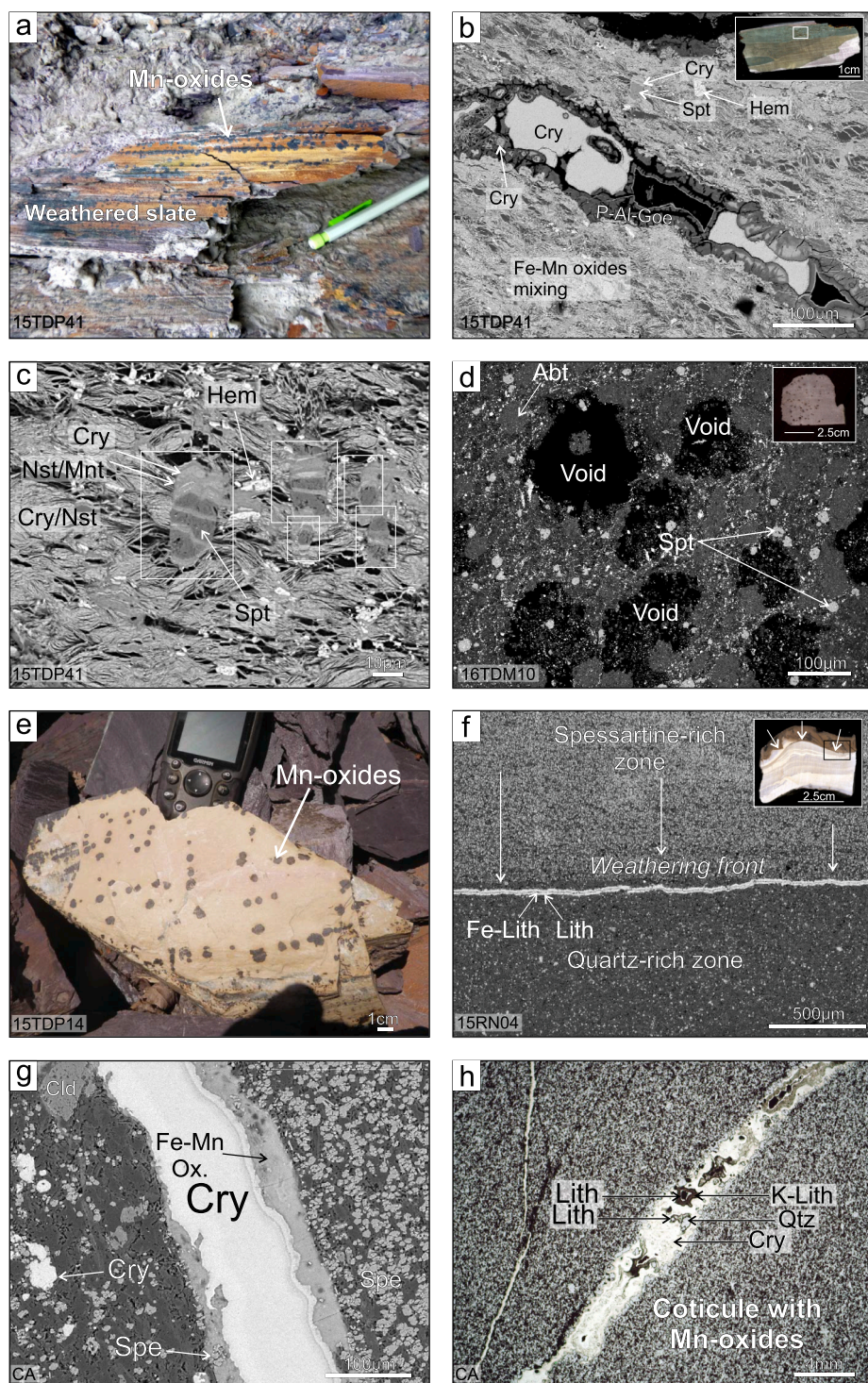
Fig. 6. Petrographic features of Thier del Preu and Regnié quarries with their coticule levels. a) Weathered Mn-rich purple slate showing Mn oxides (black halos) and secondary Fe-oxides (yellow to brown tints) on the surface. b) Back-scattered electron view of heavily weathered lenses containing botryoidal P-Al-rich goethite veins filled by cryptomelane. The micaceous matrix is replaced by nsutite/manganite and cryptomelane, conserving the typical habitus of muscovite-illite. Spessartine is also partially replaced, whereas hematite remains stable. c) Back-scattered electron view of spessartine crystals (delimited by white rectangles) partially replaced by cryptomelane and nsutite/manganite, together with the micaceous matrix. d) Dissolved pyrite in the red slates (Unit 2) in Thier du Mont Hill (Fig. 2b). Spessartine and albite are well preserved. e) Weathered coticule level showing dark halos composed of Mn oxides. f) Back-scattered electron view of a weathering front in a coticule sample delimited by the formation of lithiophorite and Fe-lithiophorite. The boundary is well marked between the spessartine-rich and quartz-rich layers of the coticule sample. g) Back-scattered electron view of a cryptomelane vein crossing the coticule levels as it is shown in Fig. 4b. Fe-Mn oxides (undetermined) occur on the border of this vein. h) Reflected light view of a cryptomelane vein in the coticule sample showing successively the formation of cryptomelane, K-rich lithiophorite and lithiophorite from the border to the center. Cry: cryptomelane; Lith: lithiophorite; Nst: nsutite; Mnt: manganite; Qtz: quartz; Hem: hematite; Spt: spessartine; Goe: goethite; Abt: albite; Cld: Mn chloritoid. (For interpretation of the references to color in this figure legend, the reader is referred to the web version of this article.)

somewhat different. It is also necessary to keep in mind that Mn-rich sediments are composed of a succession of purple to red slates, cm-size coticule layers and Mn ore level, which are all crossed by several metamorphic veins in both locations.

5.2.1. Salmchâteau area

The manganiferous purple slates in Thier del Preu quarry are weathered into a reddish to purple clayey rock, which is impregnated by black Mn oxides (Fig. 6a) intimately mixed with the phyllosilicate matrix. Where Mn is more concentrated by weathering processes, cryptomelane and nsutite/manganite precipitate in the cleavage of

these K-phyllosilicates (illite or muscovite), or even preserve their typical habitus when replacement is nearly complete (Fig. 6b and c). Despite the fact that spessartine is generally well preserved in the weathered slates, there are evidences that cryptomelane and nsutite/manganite partially replace some of the garnet crystals (Fig. 6c). Mn veins are enclosed in the host slates and are mostly composed of cryptomelane (Fig. 6b). P-Al-rich goethite is identified on the borders of these veins, which could also contain nsutite/manganite in the center. Further east of the Thier del Preu quarry, in Thier du Mont hill (Fig. 2b), the Fe-rich purple to red slates of the Meuville Member contain cubic or rhomboedral (?) voids following the stratification of the sediments.

These minerals were probably grains of pyrite (which is unusual considering the high O_2 diagenetic environment) or carbonates (rhodochrosite?), which are sometimes filled by sulfate minerals (Fig. 6d). Mn oxides are not reported at this location; instead spessartine, hematite and Mn-chlorite are widely preserved.

Coticule layers exhibit black to brown halos (Figs. 4b and 6e), which surround black veins or spots composed of lithiophorite, Fe-Mn oxides (thought to be Fe-lithiophorite) and cryptomelane (Fig. 6f, g and h). These veins are also present in the enclosing slates. Their occurrence is only clearly shown when the rock is strongly weathered, as coticule seems to be more resistant to weathering than the host slates. These veins display a mineral sequence of successive Mn-Fe-oxides, cryptomelane, K-rich lithiophorite and lithiophorite from the edge to the core (Fig. 6f, g and h). K-rich lithiophorite makes the transition between the aforementioned minerals (Fig. 6h); Fe-Mn oxides (Fe-lithiophorite?) are present on the borders (Fig. 6g). These Mn oxides also separate the brownish weathered coticule and the "fresh" coticule, as a sharp boundary (Fig. 6f). The delimitation is not randomly distributed, but occurs mainly between the spessartine-rich layers of the coticule samples. This observation clearly shows the link between spessartine and secondary supergene Mn oxides in coticule (Fig. 6f). We also noted that some muscovite could be slightly enriched in Fe and Mn, probably because they were partially replaced by Mn oxides, as already demonstrated in the weathered Mn-slates (Fig. 6c).

The study of Mn oxides in the Bihain quarry brings new insights to the petrography of the Mn-rich slates, as they are higher elevated (572 m) and more weathered than in Thier Del Preu quarry (486 m). Centimeter-size Mn-veins crosscut the red clayey rocks (Fig. 7a and b). These veins are successively filled by cryptomelane, and sometimes lithiophorite in the core (Fig. 7b and c) or as a coating onto cryptomelane crystals (Fig. 5e). The latter could be present in small quantities at the contact of these veins and the host slates. Scanning Electron views also show that cryptomelane replaces a former mineral, as cryptomelane contains ~1 wt% Ca. An analogue observation exhibits rhombohedral nsutite/manganite crystals, which means this mineral could have replaced a former carbonate (Post, 1999; Fig. 7d). These crystals are embedded in a cryptomelane matrix and located only in the highly mineralized zones. Lithiophorite and a second generation of cryptomelane veinlets also crosscut this first cryptomelane generation (Fig. 7b). Another interesting petrographic feature is the presence of cryptomelane spots disseminated in the host slates (Fig. 7e), which is a common feature with Thier del Preu quarry. Goethite crystals are associated with cryptomelane and lithiophorite.

The slates are crossed by several metamorphic veins, most of them being composed of quartz, andalusite-kanonaite, pyrophyllite, hematite, Mn-chlorite and muscovite. No replacement texture of the metamorphic Mn-silicates by Mn oxides were evidenced in these veins. However, pure cryptomelane veinlets cross such kind of veins and form cement to the brecciated quartz (Fig. 7f).
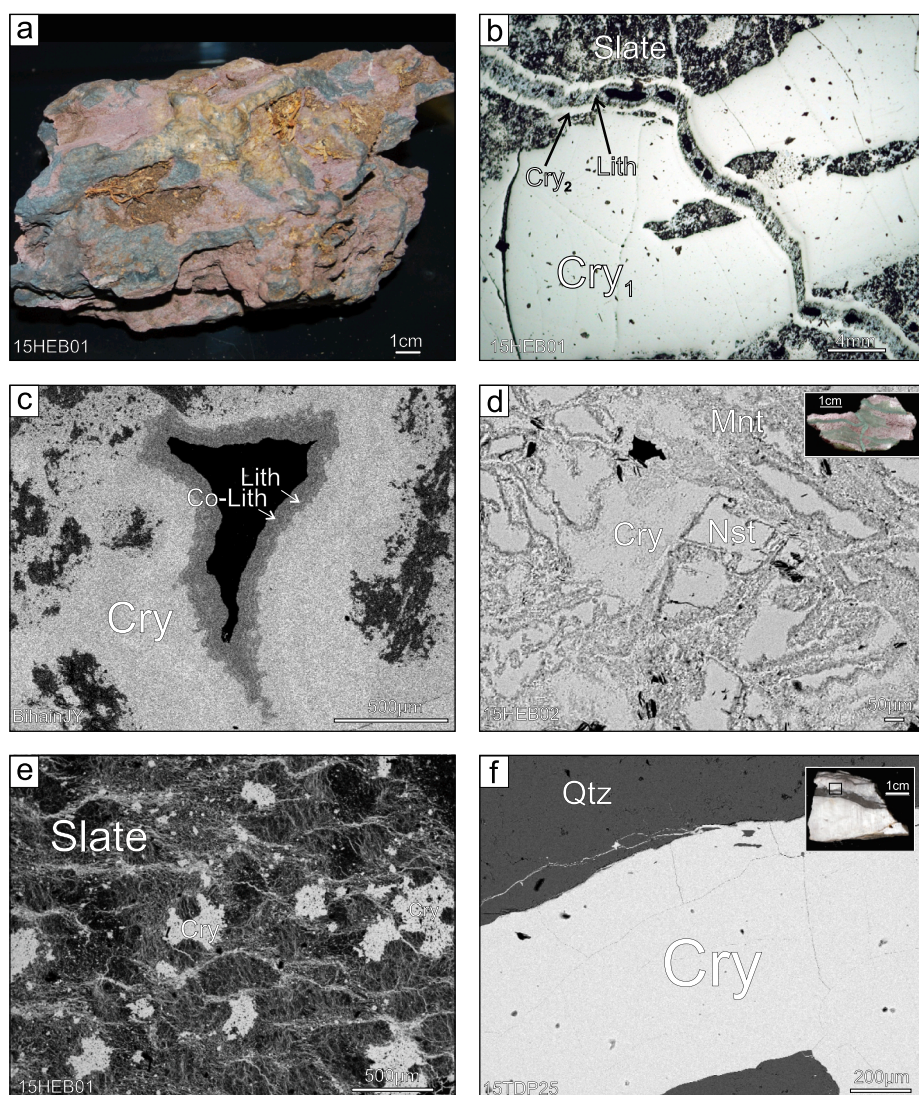
Fig. 7. Petrographic features of the Bihain quarry and metamorphic veins. a) Heavily mineralized slate crossed by several veins of Mn oxides (mainly cryptomelane) in the Bihain quarry. b) Reflected light view of a cryptomelane vein (Cry_1) crossed by a second generation of cryptomelane veinlet (Cry_2), subsequently filled by lithiophorite. c) Back scattered electrons view of cryptomelane and lithiophorite filling voids, showing the typical colloform texture. d) Back scattered electrons view of nsutite replacing rhomboedral crystals and cemented by cryptomelane and manganite/nsutite. e) Back scattered electrons view of disseminated spots of cryptomelane in the host slate. f) Back scattered electrons view of cryptomelane veinlets crossing a metamorphic quartz vein in Thier del Preu quarry. Cry: cryptomelane; Lith: lithiophorite; Nst: nsutite; Mnt: manganite; Qtz: quartz.
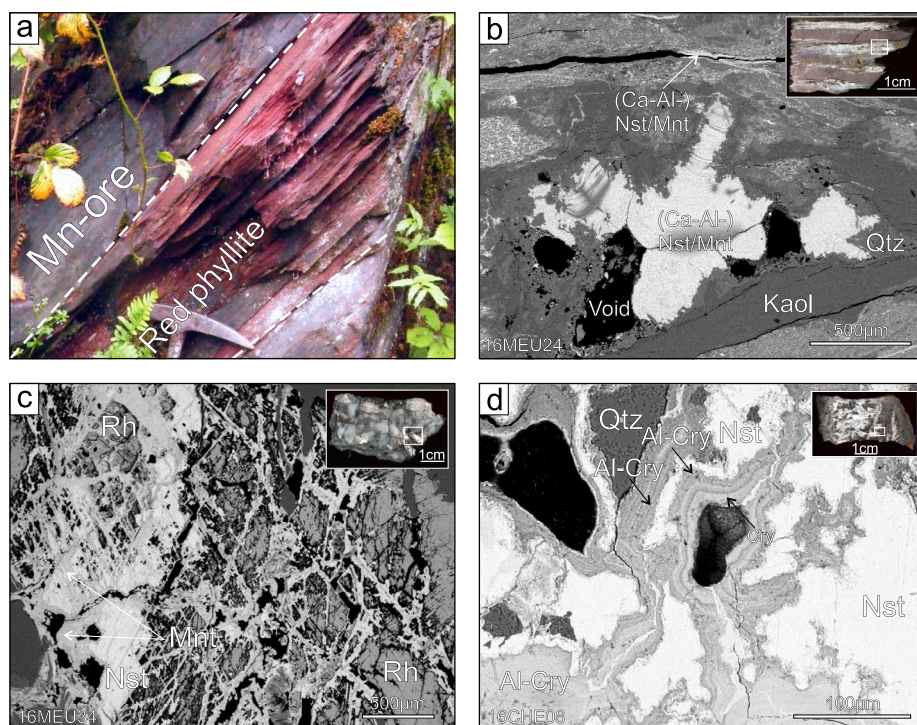
Fig. 8. Petrographic features of the Chevron area. a) Mn ore level interbedded with red phyllites in "Les Salins" quarry (see Fig. 2b for location). b) Back scattered electrons view of rhodochrosite lenses replaced by successive kaolinite and Ca-Al-bearing nsutite/manganite in the Meuville mine. See the similar texture between this weathered sample and the non-weathered sample of Fig. 4c containing well-preserved rhodochrosite lenses. c) Back-scattered electron view of the Mn ore (Unit 4) in the Meuville mine, showing rhodochrosite partially replaced by nsutite and manganite. d) Back-scattered electron view of rhodochrosite-quartz veins extensively replaced by nsutite and manganite in the Meuville mine, and filled by several generations of Al-rich cryptomelane. Nst: nsutite; Mnt: manganite; Kaol: kaolinite; Qtz: quartz; Hem: hematite; Rh: rhodochrosite; Spt: spessartine. (For interpretation of the references to color in this figure legend, the reader is referred to the web version of this article.)

5.2.2. Chevron area

The slates are rather red than purple in the Chevron area, which is probably due to the combination of lower metamorphic grade and the relative Fe content of the sediments (Fig. 3a). These red slates are interbedded with gray levels of sandstone and show Mn-Fe laminations (Fig. 8a). Weathering processes are less recorded in the Chevron area: most of the red slates show only partial dissolution features and black impregnations. These impregnations and veinlets are mainly composed of manganite/nsutite sometimes enriched in Ca (Fig. 8b), and subordinate amount of cryptomelane or lithiophorite.

The base of the Les Plattes Member consists of a coarse dark red Mn-Fe-ore level composed of rhodochrosite, spessartine, hematite, chlorite, Mn-chlorite, kutnohorite and quartz (Figs. 4d and 8a). Two generations of rhodochrosite occur, as nodules and cement in the brecciated ore. Spessartine also replaces rhodochrosite nodules on the border (Fig. 4d). Folded hematite in spessartine crystals indicates that hematite was present before metamorphism, and confirms hematite to be the results of sedimentary or diagenetic processes. The Mn ores are poorly weathered but when this is the case, Mn carbonates are replaced or crossed by manganite/nsutite veinlets, which are enriched in Ca in some sections (Fig. 4d).

Metamorphic rhodochrosite-quartz-chlorite veins usually occur across the Salm Group in the Chevron area, but also as cm-size lenses following the stratification of the red slates (Chevron borehole; Graulich, 1966; Fig. 4c). When these veins are weathered, they are characterized by black, red or orange mineral assemblage tints (Fig. 8b). The composition of the weathering product is mainly manganite, nsutite and pyrolusite (Fig. 5f, 8b, c and d) together with kaolinite (Fig. 8b). Al-cryptomelane is a subordinate mineral growing onto the cation-free Mn oxide minerals with typical growth bands (Fig. 8d). Red to orange tints are typical features of Fe-oxides (hematite, goethite and limonite).

5.3. Geochemistry of the ores

In order to better understand the geochemical signature of the Mn-rich rocks, we have subdivided the analyzed samples into different categories: (1) Mn-rich slates, (2) weathered Mn-rich slates, (3) pure Mn oxides, (4) carbonate Mn ores, (5) coticule layers and (6) metamorphic veins. Previous geochemical studies (e.g., Herbosch et al., 2016) mainly focused on the sedimentary features of the Ottré Formation, trying to identify the nature of the Mn-rich protore. Thereby, these sediments were enriched in iron and manganese before they underwent subsequent weathering conditions, the first enrichment of Mn being related to the input from hydrothermal vents in the Rheic ocean (Herbosch et al., 2016).

5.3.1. Chemical composition

Major element composition is compared to the average slate of the Les Plattes Member (Herbosch et al., 2016) in order to show variation in the chemical compositions with weathering (Fig. 9a). Manganese enrichment is slightly higher in the weathered Mn-rich slates than in the carbonate Mn ores, showing 4.1–10.1 and 1.9–5.5 times the average Mn-slate composition, respectively. Coticule layers have intermediate MnO composition between 4.4 and 6.8 the average Mn-slate (Table 2, Fig. 9a). As coticule and slates result from two different sedimentary processes, their Mn/Fe ratios differ quite well, showing high Mn/Fe ratio (1.6–22.4) and low Mn/Fe, respectively (0.01–0.4; Herbosch et al., 2016). Heavily weathered Mn-rich slates, where Mn oxides widely occur, are significantly enriched in Mn, reaching Mn/Fe ratios higher than 0.90, which correspond to concentration ranging between 15.8 and 39.2 wt% MnO (Table 2). Carbonate Mn ores of the Chevron area have higher enrichment in CaO and Fe_2O_3 than the average slate and weathered Mn-rich sediments of the Salmchâteau area, a feature related to the carbonate nature of the sediments containing abundant Ca-rhodochrosite (and kutnohorite) and hematite. Na_2O, K_2O and TiO_2 are slightly depleted in the carbonate Mn ores because detrital and/or authigenic clays and Fe-oxides are less abundant (Fig. 9a). Slate patterns are variable as a whole, because some of them could be slightly weathered, or because they do not originate from the same stratigraphic level than the average Mn-slate (Fig. 9a). An interesting style of these majors is the decrease in the SiO_2, Al_2O_3 and MgO content of the weathered Mn-slates in comparison with the average slate.

5.3.2. Rare Earth Elements

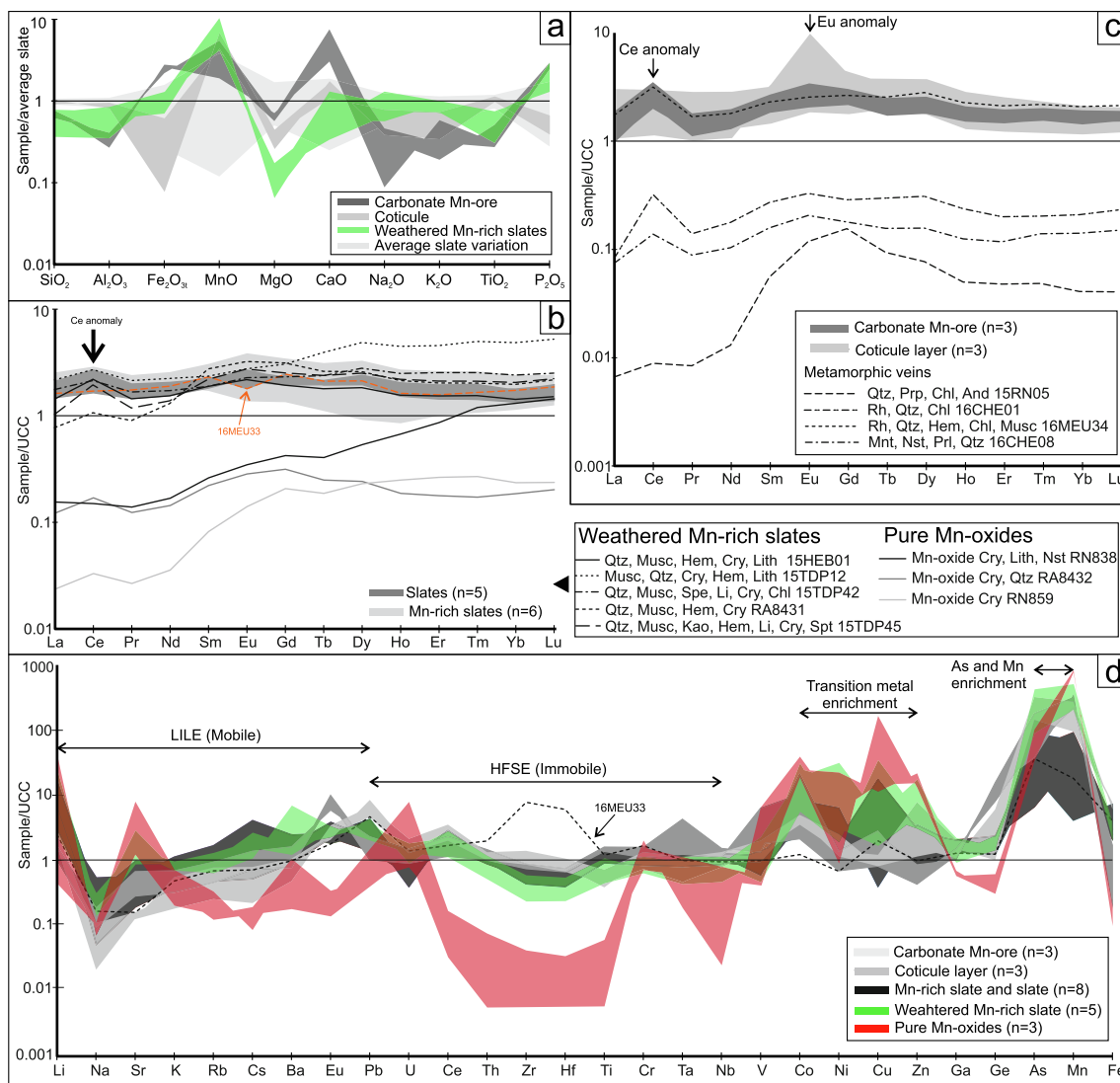Rare Earth Elements (REEs) in the Mn-rich slates, carbonate Mn

Fig. 9. Geochemistry of the Mn-rich slates, weathered Mn-rich slates, pure Mn oxides, carbonate Mn ores, coticule layers and metamorphic veins. a) Major element patterns compared to the average slate of the Ottré Formation (Herbosch et al., 2016). b) Rare Earth Elements patterns of some slates (light gray) and Mn-rich slates (dark gray) together with the patterns of each individual weathered Mn-rich slate (dashed and dotted lines) and pure Mn oxide minerals (full lines) compared to the Upper Continental Crust (McLennan, 2001). c) Rare Earth Elements patterns of the carbonate Mn ore of the Chevron area (dark gray) and coticule layers (light gray) together with metamorphic veins (dashed and dotted lines) compared to the Upper Continental Crust (McLennan, 2001). d) Trace element pattern of carbonate-hosted Mn ores of Chevron, coticule layers of Salmchâteau, Mn-rich slates and slates, weathered Mn-rich slates and pure Mn oxides, compared to the Upper Continental Crust (McLennan, 2001).

ores, metamorphic veins and coticule layers are poorly concentrated. The maximum value is reached in coticule layers (431 ppm) and minima in metamorphic veins (2 ppm). Pure Mn oxides contain little amount of REEs ranging between 8 and 31 ppm, while weathered Mn-slates do not show significantly higher values (239 and 381 ppm) than the poorly weathered Mn-slates (243 to 404 ppm), indicating there is no additional concentration of these elements during weathering processes (Fig. 9b and c; Table 3).

The Mn-rich slates display a flat pattern, which actually follows the UCC reference with a slight enrichment and possibly some slight Ce positive anomalies ($1.01 < Ce/Ce^* < 1.95$; McLennan, 2001; Fig. 9b). Note that a positive Eu anomaly could be observed in the Mn-rich slates ($1.07 < Eu/Eu^* < 1.21$), whereas only sample 16MEU33 displays a negative Eu anomaly ($Eu/Eu^* = 0.75$; Fig. 9b). The Ce ($1.27 < Ce/Ce^* < 1.77$) anomaly is reinforced in the weathered Mn-slates probably because Mn oxides widely occur in comparison with other analyzed slates (Fig. 9b). The flat pattern is not significant in all of these samples, as MREE or HREE could be favored instead of LREE, showing an

asymmetric trend with low La_N/Lu_N ratios ranging from 0.36 to 0.95 (Table 3). The REE content of the carbonate Mn ores and metamorphic veins in the Chevron area exhibit the same pattern in the weathered and non-weathered samples, showing a relatively flat pattern with a clear positive Ce anomaly ($1.78 < Ce/Ce^* < 2.05$ and $1.19 < Ce/Ce^*2.98$, respectively; Fig. 9c). While the REE values are close to that of the UCC reference for the carbonate Mn ores, metamorphic veins are largely below the values of McLennan (2001), except sample 16MEU34 which follows the carbonate Mn ore (Fig. 9c). An interesting feature of these geochemical patterns is the absence of a Ce anomaly in metamorphic veins of the Salmchâteau area, together with relative enrichment in MREE compared to LREE and HREE (Fig. 9c). Pure Mn oxides are characterized by an asymmetric pattern, where HREE are clearly favored, providing La_N/Lu_N ratios between 0.10 and 0.63 (Fig. 9b). However, all these profiles are below the UCC reference and slight positive Ce anomalies can be observed in pure cryptomelane samples ($1.32 < Ce/Ce^* < 1.38$). Coticule layers exhibit a flat pattern, but where a positive Eu (and MREE in general) anomaly is clearly shown,

ranging between 1.60 and 2.66 (Table 3; Fig. 9c).

5.3.3. Trace elements

A particular feature of trace element spider diagrams resides in a relatively strong enrichment in some transition metals (Fig. 9d). Arsenic is the most obvious one, showing enrichment overpassing 10 times the UCC reference of McLennan (2001) in all samples that are linked to the Mn-content of the sediments. Other metals, such as Co, Cu, Zn and Ni (Pb?), are particularly enriched in the weathered Mn-rich slates or in pure Mn oxide minerals up to 10 times the UCC reference (McLennan, 2001). Weathered coticule layers exhibit an enrichment in Co and Cu

only, while carbonate Mn ores have relatively high Co and Zn values (Table 2). Note that V could be high but is rather related to the composition of spessartine or chloritoid in coticule layers than in weathering minerals. Lithium is enriched in all samples when compared to the Upper Continental Crust, and is more concentrated in the weathered Mn-slates (46–477 ppm) and in pure Mn oxides (9–862 ppm), especially those samples containing lithiophorite. Despite the fact that Na is depleted in almost all rock types, mobile and immobile elements do not shift away from the average UCC reference. However, an exception is made for some elements: the substitution of Sr in cryptomelane can lead to a slight enrichment in the weathered Mn-rich slates and pure Mn
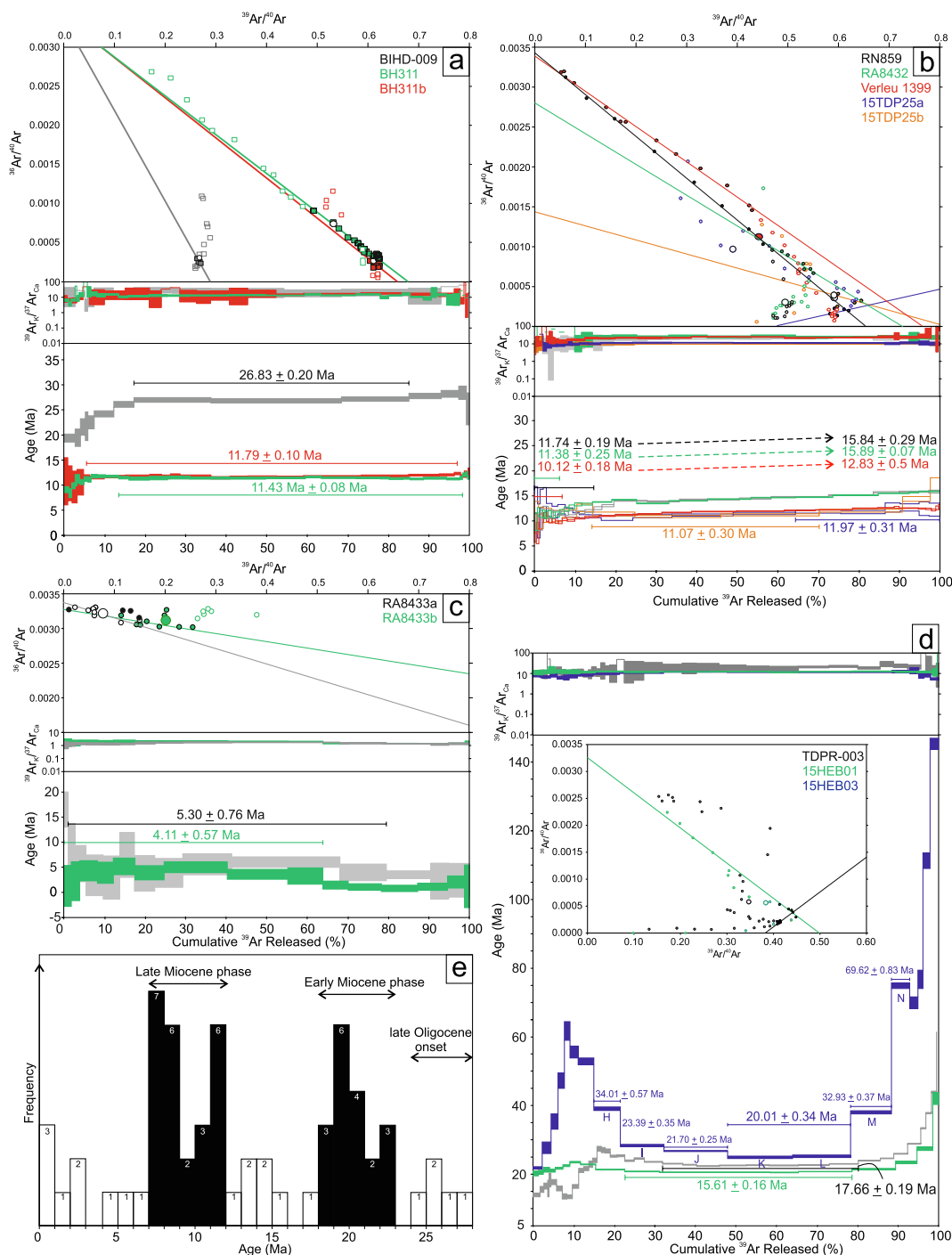
Fig. 10. ^{40}Ar/^{39}Ar geochronological data of the Salmchâteau area. a) Plateau ages obtained from three cryptomelane samples. b) Staircase spectra with non-plateau ages. c) Younger ages yielded from cryptomelane samples. d) Pseudo-plateau ages followed by staircase spectra showing increasing ages in the high temperature domain. e) ^{40}Ar/^{39}Ar age histogram for Mn oxides in Western Europe, including data from the Salmchâteau area. The ages are in Table 1.

oxides; Zr and Hf are relatively low in the weathered Mn-rich slates and high in Mn-slate 16MEU33 depending on the detrital input of the former sediments.

5.4. ^{40}Ar-^{39}Ar dating

The examination suggests that the K-Mn oxides studied for geochronology consist mainly of cryptomelane, with subordinate amounts of lithiophorite, manganite and nsutite (Fig. 5a). Void-filling cryptomelane is generally very pure, cryptocrystalline, and characterized by a homogeneous composition (Fig. 5b and d). All ^{40}Ar/^{39}Ar results, corrected for interfering isotopes and mass discrimination, are included in supplementary material and summarized in Table 4. These results are illustrated in Fig. 10. The plateau ages are defined by a sequence of three or more continuous steps that contain more than 50% of the total amount of ^{39}Ar released and yield apparent ages that are overlapping at 2σ (95% confidence level). Pseudo-plateau ages are determined as a sequence of three steps containing less than 70% of the total ^{39}Ar released, but the age values reproduce only 90% of the confidence level (2σ; Fig. 10a). Other ages are generally not considered as they are defined by less than 50% of the total amounts, of ^{39}Ar released and age values of each step are only reproducible by less than 90% confidence level (Fig. 10b, c, and d). Although this third type of age cannot provide absolute ages, they still contain valid geochronological information (Vasconcelos, 1999), which can be helpful to better understand the formation and timing of Mn oxides.

Plateau ages are somewhat difficult to be determined in the studied samples as they often reproduce less than 95% of the confidence level (2σ). Three samples yield pretty well-defined plateau ages of 11.29 ± 0.08 Ma, 11.79 ± 0.10 Ma and 26.83 ± 0.20 Ma (Fig. 10a), which are similar to the intercept ages in the inverse correlation plots and correspond to homogeneous K/Ca ratios (Fig. 10a). These data suggest the lack of recent radiogenic loss and ^{39}Ar recoil effect (e.g., Onstott et al., 1995), of contamination by old minerals or of inherited argon resulting from the decomposition of parent minerals. Therefore, the plateau ages are reliable and interpreted as precipitation age. Note that samples BIHD-009 and BH311 spectra show some minor interaction of the crystals with non-atmospheric or groundwater argon resulting in an increase of the ages in the first steps (Fig. 10a). This effect is not significant because the subsequent plateau ages are well-defined in the middle to high temperature steps.

Despite the relative chemical homogeneity of the collected samples, and the absence of growth bands, most of the analyzed samples do not show well-constrained plateaus. When the grains contain multiple generations of cryptomelane (Fig. 7b), which possess variable retentivity properties, incremental heating analyses result in staircase

spectra (Fig. 10b; Vasconcelos, 1999). Samples RN859, RA8432 and Verleu 1399 yield pseudo-plateaus in the low-temperature steps with 11.74 ± 0.19, 11.38 ± 0.25 and 10.12 ± 0.18 Ma ages, respectively, represented by less than 20% of the total amount of ^{39}Ar released. The inverse correlation diagrams using these steps provide similar intercept ages and atmospheric initial ^{40}Ar/^{36}Ar ratios (Fig. 10b). Subsequent mid-to high-temperature steps increase progressively to reach 15.84 ± 0.29, 15.89 ± 0.07 and 12.83 ± 0.50 Ma, respectively, at the end of the incremental degassing, without intermediate plateau ages. For RN859 and Verleu 1399, K/Ca values also show a slight increase during step-heating (Fig. 10b), while they remain constant for RA8432 (Fig. 10c). For samples 15TDP25a and b (Fig. 7f and 10b), two pseudo-plateau ages of 11.97 ± 0.31 and 11.07 ± 0.30 Ma can be calculated, respectively, on the final and intermediate portion of each spectrum (36 and 56% of ^{39}Ar released), which are quite similar to their total fusion ages. For both samples, the K/Ca ratios remain stable but no intercept age can be determined in the inverse correlation plot (Fig. 10b; Table 4). Ages outside the range 11–12 Ma for these samples are interpreted as a consequence of argon losses (sample 15TDP25a) or excess argon contamination (sample 15TDP25b). Two other plateau ages of 5.30 ± 0.76 and 4.11 ± 0.57 Ma are determined in samples RA8433a and RA8433b (Fig. 10c) and yield the youngst ages of the area. It is noteworthy that the atmospheric contents in these samples is very high (Fig. 10c), resulting in large errors on individual step ages and meaningless intercept ages in the isochron plots since the experimental points concentrate near the ordinate axis (Fig. 10b). Moreover, the age decrease observed for sample RA8433b at the end of degassing can suggest that ^{39}Ar recoil effect modified the original distribution of argon in this sample, or alternatively mixed generations of cryptomelane. Therefore, careful attention has to be taken interpreting these ages whose do not necessarily correspond to the timing of this Mn oxide formation, the true precipitation being younger.

^{39}Ar loss by neutron induced recoil is common in ^{40}Ar/^{39}Ar geochronology of Mn oxides (Vasconcelos, 1999), mainly due to the very fine-grained nature of the minerals (< 1–10 μm; Fig. 5c). When significant ^{39}Ar loss occurs, reliable age information on the samples cannot be retrieved. However, if only a minor amount of ^{39}Ar is lost by recoil, a plateau or pseudo-plateau age may still be obtained (Vasconcelos, 1999). Fig. 10d illustrates age spectra for samples that appear to have experienced ^{39}Ar recoil during neutron irradiation procedures. The spectra are characterized by apparent old ages in the low-temperature steps, which decrease progressively at middle and higher temperatures, and finally reach a pseudo-plateau defined by the mid-high temperature steps. The apparent ages are 17.66 ± 0.19 and 15.61 ± 0.16 Ma for samples TDPR-003 and 15HEB01, respectively (Fig. 10d), being the maximum estimates for the age of these samples. However, these
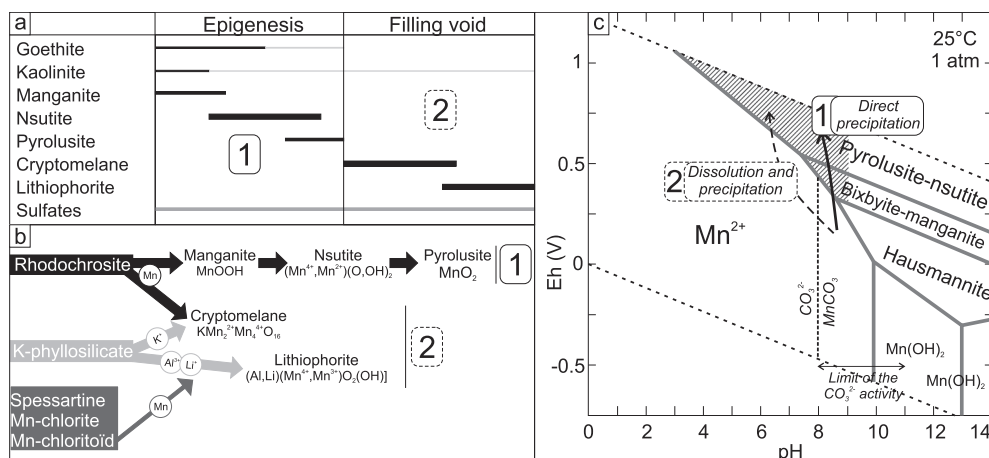

Fig. 11. a) Tentative paragenetic sequence of the manganese oxides and other supergene minerals during weathering processes. The first stage corresponds to the epigenesis of the host rock as shown in Fig. 6c and 8, while the second generation fills open cavities or veins (Fig. 6b and 7b). b) Mineral transformation chart during weathering of the early Mn-bearing minerals. c) Eh-pH diagram showing the oxidation of Mn (black arrow) at 25 °C and 1 atm. Dissolved Mn is calculated from log_{aMn} = -6. Direct oxidation (1) of rhodochrosite into cation-free Mn oxides (manganite, nsutite and pyrolusite) is shown by the black arrow. Dotted arrow is the alternative pathway where Mn^{2+} is dissolved within the weathering solution and then precipitated in veins by the oxidation potential (2), forming cryptomelane and lithiophorite. Hatched area corresponds to the supergene ore forming conditions. The upper pH boundary is variable depending on the activity of CO_3^{2-}.

spectra are often more complex because they cumulate recoil effect and contamination of other generations of cryptomelane or minerals, resulting in a saddle-shaped profile. For example, sample 15HEB03 could contain at least two generations of cryptomelane veins as it has been observed in other samples of the same area, or that micas have contaminated the sample (Fig. 7a and b). This is materialized by five mid-temperatures steps accounting for > 60% of the total ^{39}Ar released. These steps yield descending apparent ages at 34.01 ± 0.57, 23.39 ± 0.35 and 21.70 ± 0.25 Ma (H, I, J), respectively, whereas the two subsequent steps yield an internally concordant but much younger apparent age of 20.01 ± 0.34 Ma. The following high-temperature steps provide older ages of 32.93 ± 0.37 Ma and 69.62 ± 0.83 Ma and finish with 139.52 ± 1.76 Ma (Fig. 10d). Variation of the ages and the K/Ca ratios (Fig. 10d) for a single grain indicates mixing of radiogenic component domains, for example by recrystallization of older material (cryptomelane or other Mn-bearing minerals). Contamination of K-micas could not influence these ages, as the K/Ca ratio decreases when the age of the sample increases (Fig. 10d). However, mid-temperature steps in samples TDPR-003 and 15HEB01 contain internal pseudo-plateau ages of 17.66 ± 0.19 Ma and 15.61 ± 0.16, respectively. Subsequent high-temperature steps end with 56.45 ± 0.50 and 77.31 ± 1.88 Ma. For these samples, the minimum ages provided by the intermediate portion of the spectra have to be considered as maximum ages for the last recrystallization of cryptomelane. The 20.01 ± 0.34 Ma age of sample 15HEB03 is also a maximum age consistent with the 20.0 ± 0.2 and 22.2 ± 0.6 Ma obtained by Demoulin et al. (2018) in the same area.

6. Discussion

6.1. Paragenetic sequences

The determination of the relative timing of each mineral formed during weathering of the Mn-slates, coticules, carbonated Mn ore and metamorphic veins, is an essential point to i) decipher the genesis/processes of the weathering and ii) interpret the ^{40}Ar/^{39}Ar dating of secondary K-Mn oxides. Such paragenetic sequence is summarized in Fig. 11a. Petrographic observations indicate that the formation of Mn oxides in the Chevron and Salmchâteau area could follow two processes. First, rhodochrosite is directly weathered into cation-free Mn oxides, as this mineral is successively replaced by manganite, itself replaced by nsutite (Fig. 8c) and then pyrolusite (Fig. 5f). Such replacement of rhodochrosite has already been proposed by Gustine (2002). This feature is common in supergene manganese deposits worldwide (Post, 1999): most of nsutite is genetically derived from early carbonates (Zwicker et al., 1962) and this mineral with cryptomelane and lithiophorite are known as late alteration or weathering products of carbonates and, possibly, Mn-rich silicate. Cryptomelane occurs after the formation of these cation-free Mn oxides as they fill open voids and form the typical growth band textures growing onto weathered rhodochrosite (Fig. 8d) in the Chevron area. The same observation is made in the Salmchâteau area where nsutite/manganite replace former carbonate crystals and are cemented by a first generation of cryptomelane (Fig. 7d). This generation of cryptomelane forms also cm-size veins crossed by a second generation of K-Mn oxide, indicating that these minerals were formed at different stages of weathering (Fig. 7b and f) and corroborate discordant ^{40}Ar/^{39}Ar spectra (Fig. 10b and d). Lithiophorite occurs only in the core of cryptomelane veins, and is therefore the last Mn oxide to form during weathering (Fig. 6h, 7b and c). Fransolet (1979) and Gustine (2002) also identified replacement of cryptomelane veins by nsutite and cryptomelane by lithiophorite. Other supergene minerals associated with these Mn oxides include goethite and kaolinite. In the Salmchâteau area, small veins of goethite precipitate at the border of cryptomelane veins (Fig. 6b and g). In the Chevron area, kaolinite clearly precipitates before nsutite/manganite, as they fill the border of small druses, when nsutite/manganite

occurs in the core (Fig. 8b). Kaolinite is evenly dispersed in the weathered slates and coticule in the Salmchâteau area. Note that groutite (MnOOH), hausmannite (Mn_3O_4), hollandite-strontiomelane [$(Ba,Sr)Mn_8O_{16}$], hetaerolite ($ZnMn_2O_4$) and todorokite [$(Ca,Na,K)_X(Mn^{4+}, Mn^{3+})_6O_{12}\cdot3.5H_2O$] have also been described in relation to these metasediments, some of them having a hypogene origin (Blondieau, 2019; Blondieau et al., 2017; Fransolet, 1979; Fransolet and Mélon, 1975; Gustine, 2002; Hatert et al., 2014; Herbosch, 1967; Mélon et al., 1976; Schreyer et al., 2001), but are not detected in this study.

The final sequence of supergene minerals (Fig. 11a) indicates that weathering processes differ between the Chevron and Salmchâteau area. Weathering is incomplete in the Chevron area, because cryptomelane and lithiophorite are very scarce, whereas cation-free Mn oxides prevail. The polyphased formation of cryptomelane in the Salmchâteau area corroborates the high weathering state of the Mn-rich slates in this area.

6.2. Origin of manganese and weathering transformations

One of the most important question about the formation of weathering manganese deposits is the origin of manganese. Here, manganese seems not to have been transported for long distances, as the weathering manganese phases are restricted to the Mn-rich stratigraphic levels, and are not observed in the upper Bihain and lower Jalhay Formations. Transport of Mn is local (millimeters to meters) as it is supported by the occurrence of disseminated cryptomelane (Fig. 7e), cryptomelane-lithiophorite veins within the host Mn-bearing slates in the Salmchâteau area (Fig. 7a and b), and the *in situ* replacement of rhodochrosite by manganite, nsutite and pyrolusite in the Chevron (Fig. 8c) and Salmchâteau areas (Fig. 7d). Major elements geochemistry show that the enrichment factor of the weathered Mn-slates is, at least, between 4 and 10 times the composition of the average Mn-slates (Fig. 9a). This clearly shows that Mn is favored, instead of iron under weathering conditions.

Several modes could explain the formation of Mn oxides. It may result from oxidative dissolution and replacement of early Mn carbonates (rhodochrosite and kutnohorite) and Mn phyllosilicates (Mn-rich chlorite), but also to the replacement of spessartine, a feature which is quite unusual considering that garnet weathering rate is slow in saprolites (Parc et al., 1989; Price et al., 2005; Varentsov, 1996; Velbel, 1984). The Mn^{2+} is released and oxidized through the increasing weathering conditions, leading Mn to be incorporated first, into manganite as Mn^{3+} ($Mn^{3+}OOH$), then into nsutite as a combination of Mn^{2+} and Mn^{4+} [$(Mn^{4+}, Mn^{2+}) (O,OH)_2$; Fig. 8c], and finally into Mn^{4+} to form pyrolusite ($Mn^{4+}O_2$; Figs. 5f and 11b). The relative hydration of some of these minerals indicate that they were possibly formed within the vadose zone. The Eh-pH conditions can be established with the help of a Pourbaix diagram (Fig. 11c). The early Mn-bearing carbonates are dissolved and oxidized to the highest oxidation state defined by the pyrolusite-nsutite field. The pH conditions are below 7–9 pH units, depending on the CO_3^{2-} concentration in the weathering fluid. The latter delimits the dissolution of Mn carbonates. The main factor controlling the *in situ* transformation from carbonates (or silicates) into oxides is the Eh potential (> 0.5 V). Mn^{2+} is not transported for long distance within the saprolite and is rapidly oxidized. The role of pH is then secondary in the formation of such epigenetic cation-free Mn oxides (nsutite, manganite and pyrolusite), but could be important in the local motion of dissolved Mn^{2+} in the weathering solutions. Cryptomelane, lithiophorite and some nsutite/manganite seem to be tightly associated with the phyllosilicate matrix (illite-muscovite; Fig. 6c), suggesting that neutralization of these minerals together with the high Eh potential is responsible for the formation of veinlets. Cryptomelane ($KMn_6^{4+}Mn_2^{2+}O_{16}$) and lithiophorite [$(Al,Li)(Mn^{4+},Mn^{3+})O_2(OH)$] fromation results from the recombination of K^+, Al^{3+} and Li^+ released from the K-phyllosilicate matrix, and

Mn^{2+}, Mn^{3+} and Mn^{4+} from primary Mn-bearing minerals into open voids of the weathering solutions (Fig. 11b). Despite the fact that these two minerals are often associated, cryptomelane usually forms prior to lithiophorite, probably because K^+ is a mobile element leached from K-phyllosilicates (muscovite-illite) and act as a limiting cation in the formation of K-bearing Mn oxides (Parc et al., 1989; Varentsov, 1996). The less mobile Al and poorly concentrated Li cations allow the formation of lithiophorite in the center of cryptomelane veins (Fig. 7b and c). Al-rich cryptomelane or K-rich lithiophorite are probably intermediate products resulting from this reaction (Figs. 6h and 11b).

The Mn content in the phyllosilicate matrix is low and could not provide sufficient manganese to form the large number of Mn oxides. Therefore, early Mn-bearing minerals to be considered as the source of manganese could be spessartine, Mn-chloritoid, Mn-chlorite and rhodochrosite, as they are the dominant Mn-minerals in the Salmchâteau and Chevron areas (Fig. 11b). Scanning electron microscopic views show that spessartine is partly weathered into cryptomelane and nsutite/manganite (Fig. 6c). Spessartine could contain up to 43 wt% MnO following its empirical formula. The relative abundance of spessartine, and the concentration of manganese oxides in spessartine-rich zones (Fig. 6f) strengthen the interpretation that Mn could be released from partially dissolved garnet. Despite that coticule displays Mn/Fe ratios and Mn concentration higher than the host slates, weathering seems to be relatively poor where spessartine occurs. Their contribution into the weathering fluid could be limited, as they are preserved in most of the weathered rocks (Fig. 6d and g), exception made from samples highly affected by weathering processes (Fig. 6b and c). Therefore, other early Mn-bearing minerals could be responsible for the release of significant quantities of Mn. Rhodochrosite is generally a common primary (sedimentary, diagenetic and metamorphic) mineral in Mn deposits worldwide, as it could release large amounts of Mn during weathering (up to 61.71 wt% MnO), but also because it is readily dissolved than metamorphic minerals, such as garnet (i.e., Parc et al., 1989; Varentsov, 1996). Mn carbonates are not directly observed in the Salmchâteau area, but rhodochrosite has been described by Herbosch et al. (2016) and suggested as the primary Mn-bearing phase to the formation of Mn oxides by Fransolet (1979). Some enrichments of Ca in Mn oxides might indicate that early Mn carbonates (rhodochrosite, kutnohorite) were present in the Mn-slates, as well as the presence of nsutite/manganite (Post, 1999; Fig. 7d), which could have therefore provided Mn into the weathering fluid. A better interpretation is supported by the Rare Earth Elements geochemistry. Positive Ce anomalies in carbonate Mn ores and metamorphic veins of the Chevron area could be attributed to the presence of rhodochrosite, which usually traps Mn and also concentrates Ce relative to other LREE (Fig. 10c; Beukes et al., 2016; Chisonga et al., 2012; De Putter et al., 2018). As this anomaly is preserved into the cation-free Mn oxides, this supports that small

modifications are encountered through weathering processes, at least regarding the REE patterns (i.e., Varentsov, 1996). Following these observations, the presence of Ce positive anomalies in the weathered Mn-rich slates, as well as in pure Mn oxides in the Salmchâteau could decipher the former presence of rhodochrosite, or at least Mn carbonates, formed through diagenesis or metamorphism (Fig. 9b). However, the same conclusion cannot be achieved in the coticule layers, where a positive Eu (and MREE) anomaly replaces the positive Ce anomaly of Mn carbonates (Fig. 9c). Such changes in the geochemical behavior of the coticule layers, where Eu anomaly prevails instead of the Ce anomaly found in the enclosing slates, might be related to conditions during the deposition of the limy mud turbidites, now metamorphosed into coticule layers (Herbosch et al., 2016; Lamens et al., 1986; Fig. 9b and c).

Other early Mn-bearing minerals, such as Mn-chlorite and Mn-chloritoid, have probably poorly contributed to the mobilization of Mn in the supergene fluids, as they are not the dominant minerals in these rocks, but also because they are relatively stable under supergene conditions (e.g., chlorite). All these interpretations are summarized in Fig. 11b: rhodochrosite is the main early Mn-bearing mineral from which Mn has been released to form pure Mn oxides, while the phyllosilicate matrix (muscovite) has provided K, Al and Li to form cryptomelane and lithiophorite. Other Mn-bearing minerals have a limited impact into Mn and other cations mobilization.

Other trace elements could follow the same process: arsenic enrichment and its association with manganese has already been pointed out in the Chevron area (Fonseca, 1969), but also to a larger extent in Mn deposits where a hydrothermal origin is likely (Nicholson, 1992). Although this geochemical signature may result from the sedimentary settings (Herbosch et al., 2016), arsenic seems to be accommodated and retained within the Mn oxides during weathering. This observation could be extended to other transition metals, i.e. Co, Ni, Cu and Zn (Fig. 9d), which are incorporated in Mn oxides, especially in late minerals such as lithiophorite and cryptomelane (Fig. 7c). As hematite remains stable from its formation during sedimentary deposition of the slates, the presence of goethite indicates that some Fe is released during weathering. Such limited input of Fe, whereas hematite remains stable under supergene conditions implies that Fe could originate from weathering of diagenetic pyrites or carbonates, as it is found in Thier du Mont hill to the east of Thier del Preu quarry (Fig. 6d). The general decrease in the SiO_2, Al_2O_3 and MgO content of the weathered Mn-slates could also be due to the general increase in the MnO content (SiO_2 and MnO have a negative correlation) and/or to the loss of these elements during weathering as it is sometimes observed in the laterite (Widdowson, 2008 in Nash and McLaren, 2008), which would decrease the dominant major elements (i.e., SiO_2 and Al_2O_3).
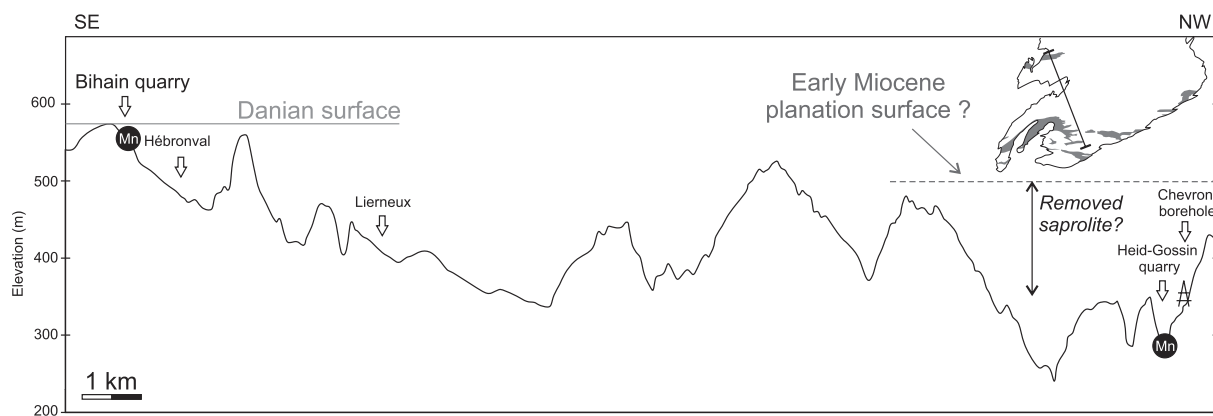

Fig. 12. NW-SE cross-section and sketch of the weathering intensity and its relation to the elevation of the area. Most of the Mn-rich slates occur below 500 m heights in the Chevron area, while these sediments are exposed to weathering agents beyond 500 m of elevation in the Salmechâteau area.

6.3. Intensity of weathering

One can see that mineralogical differences between the northern and southern areas of the Stavelot inlier clearly determines the nature of the Mn ore composition of the Salmchâteau and Chevron areas: manganese ores mined in the Salmchâteau area correspond to weathering Mn deposits, whereas in the Chevron area, the carbonate Mn ore has a sedimentary (diagenetic-metamorphic) origin. The Mn-bearing phases are mostly cryptomelane with subordinate amount of nsutite and lithiophorite in the Bihain and Thier del Preu quarries (Fig. 2b), whereas rhodochrosite dominates the Mn ore in the Chevron mines. The Chevron borehole shows that slates are poorly weathered and saprolite is not thick enough (probably only few meters; Graulich, 1966) to transform the carbonate ore. The Mn orebeds are situated beneath the saprolite, probably in the fissured zone, and therefore beneath the extrapolated Early Miocene planation surface (Fig. 12; Demoulin et al., 2018). Most of the ancient deposits were mined in deeply incised valleys, supporting that most of the weathering zone is absent and that traces of weathering are mostly recent. This further allows the interpretation that at the level of the Chevron plateau, the weathering zone cannot be observed because the Early Miocene surface is probably higher and that any older weathering phases cannot be observed.

On the other side, weathering deposits in the Salmchâteau area are located in the lower part of the saprolite, at least for the Bihain quarry (Fig. 2b and 12), and might probably be situated in the upper part of the fissured horizon in the Thier del Preu quarry, close to the roll front and saprolite (Cosan, 1969; Demoulin et al., 2018) to precipitate Mn oxides. Here, the weathered Mn ores are situated close enough to the Danian

surface to record ages as old as the late Oligocene and Miocene, although most of the upper part of the profile has been eroded, for example from its Eocene or even Cretaceous part. Another important point is that the plateaus are not deeply incised as it is the case in the Chevron area.

The topographic difference between these two areas is probably the most important factor explaining these variations, as the Mn ores in the Chevron area are located at relatively low elevation between 230 m and 380 m, compared to the Bihain and Thier del Preu quarries, culminating at 573 m and 486 m, respectively (Fig. 12). The Chevron Mn levels poorly underwent weathering processes compared to the southern area, which has contributed to the preservation of Mn carbonates. This interpretation explain the absence of rhodochrosite in the Salmchâteau area and the partial dissolution and replacement of spessartine in the slates and coticule layers. Although the Bihain and Thier del Preu ores seem to be connected to the Danian surface (Demoulin et al., 2018), their position in terms of elevation is different and impact the ages recovered from these sites. The oldest cryptomelane ages are located in the Bihain quarry, whereas the younger ones are observed in the Thier del Preu quarry (see discussion below; Table 4). This clearly demonstrates the *per descensum* evolution of the weathering fluid (e.g., De Putter et al., 2015; Vasconcelos, 1999). Such elevation effect on the development of weathering profiles is well documented in Belgium, where low elevation is nearly totally devoid of more than local spots of weathering (Alexandre and Thorez, 1995; Demoulin et al., 2018; Gullentops, 1954). However, differences in metamorphic grades, and therefore in the primary mineralogical composition between the Chevron and Salmchâteau areas, could be an additional factor
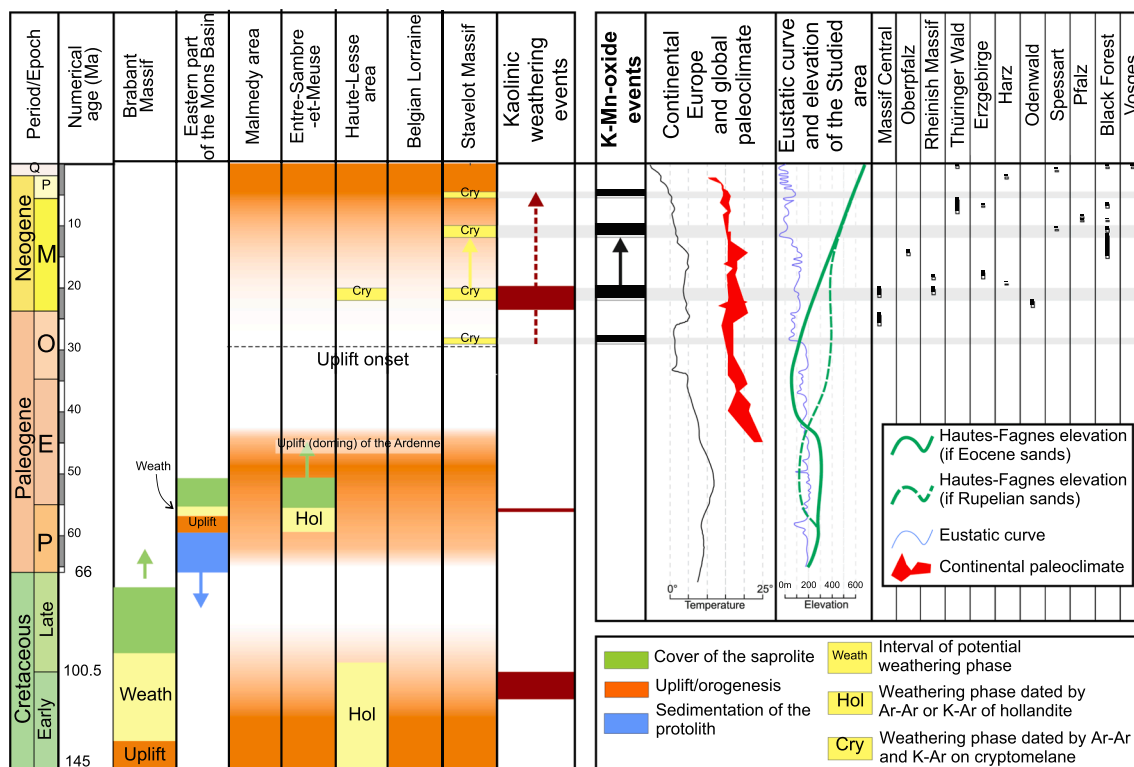

Fig. 13. Tentative chronology chart of weathering in Belgium including periods determined by $^{40}Ar/^{39}Ar$ datings of cryptomelane in the Stavelot Massif (Salmchâteau). Note that the latter periods are delimited by the late Oligocene and Pliocene. Sedimentation and geodynamic (uplift or deformation) are documented only for the weathered protolite rocks (modified after Demoulin et al., 2018). Continental European paleoclimate curves are from Mosbrugger et al. (2005) and marine climate curve is from Zachos et al. (2001). Supposed elevation of the Stavelot Massif (Hautes Fagnes) is adapted from Quesnel et al. (2002) and eustatic curve of Europe is from Hardenbol et al. (1998). K-Mn oxide events are documented by $^{40}Ar/^{39}Ar$ and K-Ar ages. All available $^{40}Ar/^{39}Ar$ of Western European massifs are included and detailed in Fig. 1 and Table 1.

explaining this distribution.

6.4. Timing of weathering and regional implications

6.4.1. Weathering in the Ardenne

The ages obtained by the $^{40}Ar/^{39}Ar$ methodology in cryptomelane samples have provided four stages for the formation of the Mn oxides, lasting from late Oligocene to Pliocene (Fig. 13): Chattian (26.83 ± 0.20 Ma), Aquitanian (22.2 ± 0.6 and 20.0 ± 0.2 Ma according to Demoulin et al., 2018), Serravalian-Tortonian (11.97 ± 0.31 to 10.12 ± 0.18 Ma) and Pliocene (5.30 ± 0.76 and 4.11 ± 0.57 Ma). There is no evidence that the whole period from late Oligocene to Pliocene has recorded a continuous weathering event, but this period seems to have produced conditions suitable for the formation of a weathering mantle. These ages also reveal that, at least, two young periods (Serravalian-Tortonian and Pliocene) of weathering affected the Ardenne region and that weathering probably ceased during the Quaternary.

The 26.8 ± 0.2 Ma age (Fig. 10a) indicates that the Mn sediments were exposed to meteoric agents at least since late Oligocene, a period when the Ardenne started to rise (Demoulin, 1995c). This age is consistent with the oldest one connected to the Neogene weathering phase in Western Europe (e.g., Dill, 1985a; Hautmann and Lippolt, 2000). Older periods of weathering cannot be excluded but are not identified in $^{40}Ar/^{39}Ar$ spectra, although some staircase shape suggest mixing with old radiogenic components (Fig. 10d). These old apparent ages are difficult to interpret but could be attributed to different cryptomelane phases, to inclusions of other minerals containing radiogenic argon or to the presence of excess argon. No inclusion of K-bearing minerals are found in scanning electron microscopic analyses, and K/Ca ratio (Fig. 10d) exclude the presence of variscan K-bearing phyllosilicates. This indicates that staircase spectrum could originate from older cryptomelane phases by recrystallization processes during weathering, a feature which has been observed in polyphased Mn deposits of R.D.Congo (e.g., De Putter et al., 2015). This period could be early Cretaceous as weathering periods have already been determined in kaolinic deposits in the Brabant, Ardenne and Bohemian massifs (Barbier et al., 2010; Gilg, 2000; Mees and Stoops, 1999; Thiry et al., 2006; Yans and Dupuis, 2005; Fig. 13) and laterite (Théveniaut et al., 2007). Late Paleocene cannot be excluded, as climatic conditions were favorable to the setting up of deep weathering mantles (i.e., Baele et al., 2016; Demoulin et al., 2018; Quesnel et al., 2002; Yans, 2003). Erosion of the upper part of the saprolite and laterite could additionnaly explain the lack of any older cryptomelane ages (Demoulin et al., 2018).

Demoulin et al. (2018) obtained $^{40}Ar/^{39}Ar$ ages at 20 ± 0.2 and 22.2 ± 0.6 Ma in the same levels. These ages are similar and probably belong to the same weathering event dated in the southern part of the Rhenish Massif at ~18.6 ± 0.2 and 20.8 ± 0.4 Ma (Hautmann and Lippolt, 2000). Most of the ages determined by the $^{40}Ar/^{39}Ar$ geochronology are concentrated in the middle-late Miocene (10–12 Ma), which can be considered as the main weathering event recorded in the Salmchâteau area (Fig. 13).

Pliocene ages (5.30 ± 0.76 and 4.11 ± 0.57 Ma) are not perfectly given by the $^{40}Ar/^{39}Ar$ methodology, as they are contaminated by atmospheric argon, which limit their full interpretation (Fig. 10c). Although the Pliocene climate was presumably warmer than today, weathering processes at this time appeared to be less intense than in the older periods. However, not considering this event seems problematic as the Harz and Bohemian massifs also displayed similar ages, and even more recent ones in the Spessart, Black Forest, Bohemian and Thuringen massifs (Figs. 1 and 13; Table 1; Carl and Dill, 1985; Dill, 1985b; Dill et al., 2010; Hautmann and Lippolt, 2000).

6.4.2. The climatic and geodynamic contribution on the development of weathering

The formation of K-Mn oxides during the late Oligocene, early Miocene and middle-late Miocene periods is the result of intense (?) chemical weathering of the Mn-rich slates. Conditions suitable for the development of a weathering profile and the formation of supergene Mn oxides generally consider a combination of a tropical or subtropical climate (Kuleshov, 2016; Varentsov, 1996; Vasconcelos, 1999), and a slow large-scale tectonic movement creating a hydrodynamic gradient (Ruddiman, 2008; Ruddiman et al., 1997; Ruddiman and Prell, 1997; Wyns, 2002; Wyns et al., 2003). Intertropical temperatures prevailed during almost the whole Eocene and, to a lesser extent, during the Middle Miocene (Alexandre and Thorez, 1995; Buchardt, 1978). Such Miocene weathering event could be supported by the development of thick kaolin deposits in Central Ardenne (Yans, 2003), but also by Fe-crust (ferricrete) in the Hautes-Fagnes where a Neogene age is suggested (Alexandre and Thorez, 1995). The tropical to subtropical continental climate of Europe during the Paleocene and early Eocene turned successively into warm temperate to temperate from the Oligocene to the Pliocene (Mosbrugger et al., 2005; Fig. 13). Most of the variations in temperature are accompanied by a relatively constant high humidity during the whole Cenozoic. Seasonality has progressively increased until present days. Middle and late Eocene recorded the first drop of temperatures in Central Europe: the climate was gradually cooling but a sharper cooling occurred worldwide at the end of the short-lived earliest Oligocene (Boulvain and Vandenberghe, 2018; De Man et al., 2004; Zachos et al., 2001). These temperatures are low until the uppermost Chattian, where a peak of temperature records the Late Oligocene Warming (Mosbrugger et al., 2005). The climate is slightly warmer in the early Miocene and persists until the middle Miocene, but is more stepwise and show several short-term variations. However, temperatures are below those recorded during the Paleocene and Eocene (Mosbrugger et al., 2005; Zachos et al., 2001). An exception is made for the Mid-Miocene Climatic Optimum, where temperatures increased significantly in different Cenozoic basins of Central and Western Europe (Mosbrugger et al., 2005). The onset of the Miocene cooling seems to be between 13 and 14 Ma and is intensified until present days with several exceptions, for example, the late Tortonian and early Zanclean warming. The Quaternary period marks the end of any weathering products thanks to a periglacial climate (Alexandre and Thorez, 1995). Pliocene ages are then a witness of the latest weathering phase in the Ardenne. This last event is also described in the Harz and Bohemian massifs (Dill, 1985b; Dill et al., 2010; Hautmann and Lippolt, 2000).

Comparing these climatic variations with the weathering periods obtained by K-Mn oxides indicate that warm climate (Fig. 13) is probably not the main factor responsible for the development of deep weathering profiles in the Salmchâteau area, as most of the cryptomelane ages do not match tropical or subtropical climates in the geological record (Fig. 13). Therefore, the main process from which weathering mantles can develop could be attributed to the combining effect of constant precipitations and slow geodynamic uplift (i.e., Vasconcelos et al., 2018; Wyns et al., 2003). The high precipitation and the seasonality during the Cenozoic can provide water to the weathering system (Mosbrugger et al., 2005), when differential uplift movements generate the weathering gradient for the downward progression of solutions and the dissolution of rocks. The role of temperature (tropical climate) in the development of a weathering profile cannot be dismissed totally, as some ages obtained by cryptomelane could correspond to warm peaks and periods in the paleoclimatic record (Mosbrugger et al., 2005). For example, the late Oligocene age could correspond to the Late Oligocene Warming, whereas Early Miocene ages could be linked to the Langhian Mid-Miocene Climatic Optimum and the global warming of the Earth. Pliocene ages could be attributed to the Tortonian-Zanclean warming (e.g., Mosbrugger et al., 2005; Zachos et al., 2001). However, the best represented cryptomelane ages range between 10 and 12 Ma (Fig. 10e), when colder wet climatic conditions prevailed in a more temperate climate.

The Ardenne is quite stable in a tectonic point of view at least until

the early Paleocene, although major uplift has exposed rocks during the Early Cretaceous (e.g., Quesnel, 2003). In fact, the Ardenne remains as high as the sea level but its borders are subjected to subsidence and then sedimentation (Demoulin, 1995b; Fig. 13). The Ardenne records its first progressive dome uplift in the middle Paleocene, leading to a slight slope oriented to the west, and then the formation of weathering mantles under a warm and humid subtropical climate (Albers, 1981; Demoulin, 1995b; Mosbrugger et al., 2005; Fig. 13). A new uplift phase can be deduced from the Lutetian, but is not associated with an intense weathering phase, as the climate is dryer and temperatures lower than the Paleocene (Albers, 1981; Demoulin, 1995b). Post-Paleocene and Eocene phases have led to only 10 Ma for the development of weathering mantles before the acceleration of the tectonic movements in the middle Oligocene (Demoulin, 1995b). Although the Alpine tectonic is poorly recorded in the sedimentary series of Western Europe, the Alpine Cycle could be responsible for the uplift of most of the Variscan massifs across Central Europe (Prodehl et al., 1995; Ziegler and Dèzes, 2007) including the Rhenish Massif (Fig. 1). The Alpine orogenesis is particularly active from the Oligocene to the Miocene and has probably affected the Ardenne until present days (Demoulin and Hallot, 2009). Additionally, the Roer Valley rifting activity (also known as the Lower Rhine Graben; Prodehl et al., 2006) could have influenced the elevation of the Stavelot Massif, the latter being situated on the shoulders of this rift system (Demoulin, 2018; Van Balen et al., 2000). The Roer rifting activity developed upon Paleozoic and Mesozoic basins is characterized by several episodes of inversion and subsidence during Mesozoic and Cenozoic times. However, the rifting activity (subsidence) increased strongly during the late Oligocene, was inverted again during the Early Miocene and continued until the present days (e.g., Deckers, 2016; Michon et al., 2003). Consequently, the Ardenne uplift may have triggered the development of weathering, as tectonic movement slightly predates the first weathering phase recorded in the Salmchâteau area by the early Chattian (Figs. 10e and 13). Moreover, the joint effect of this slight uplift with low stand levels of the sea have probably contributed to the creation of relief and a weathering gradient. For example, the global low Chattian-Aquitanian sea level (Hardenbol et al., 1998) is combined with the uplift induced by the Alpine tectonics (Savian pulse). Such combination fits well with late Oligocene ages obtained by K-Mn oxides and probably the onset of a long weathering phase. The effect of eustatism could also be supported by a good correlation between weathering ages at ~10–12 Ma and the Serravallian-Tortonian sea level drop (Hardenbol et al., 1998). Both contributions could reinforce the uplift and thus erosion.

The preservation of ages as old as the late Oligocene within the Salmchâteau weathering profile for such a long exposure time is due to the balance between erosion and weathering. It is, for example, difficult to explain that Eocene ^{40}Ar/^{39}Ar ages are not recorded, even in other European massifs (Brannath and Smykatz-Kloss, 1992; Dill, 1985b, p. 185; Dill et al., 2010; Dill and Wemmer, 2012; Hautmann and Lippolt, 2000; Segev et al., 1992), particularly as this period is considered to be a major weathering phase responsible for numerous supergene deposits under tropical conditions (Migoń and Lidmar-Bergström, 2002, 2001). These older ages are missing in the ^{40}Ar/^{39}Ar record, which is not the case in other deposits of the Ardenne (Barbier et al., 2010; Demoulin et al., 2010; Thiry et al., 2006; Yans, 2003). The slow late Oligocene uplift onset limited erosion and favoured weathering under wetter and cooler conditions than the previous supposedly Eocene and Cretaceous phases. This slow vertical motion accelerated during the Quaternary, resulting in the deep incision of valleys and the removal of the laterite in most parts of the Ardenne. Therefore, ^{40}Ar/^{39}Ar geochronological results need to consider that erosion processes have probably removed the oldest dating material, especially the upper part of the weathering mantle in which older ages (i.e., Eocene or Cretaceous) could have been preserved. This means that under a temperate climate, deep weathering developed efficiently since the Chattian and during the whole Neogene period.

6.4.3. Late Oligocene to Neogene weathering in Western Europe

Hautmann and Lippolt (2000) already pointed out that spatial and temporal distributions were difficult to fully be interpreted with the set of ^{40}Ar/^{39}Ar data in Central and Western European massifs (Fig. 1; Table 1). No relationship is observed between apparent ages and geographical location, and the episodic age distribution is not straightforward. Ages recovered from supergene deposits in the Ardenne region and other Western European (see Table 1) massifs can bring new insights on the timing of weathering in these areas. It has to be noted that we discuss about the ^{40}Ar/^{39}Ar data on K-Mn oxides, rather than K-Ar ages, as the former provide an internal control of the ages (i.e., Vasconcelos, 1999), and render the results comparable. ^{40}Ar/^{39}Ar data show that there are very few, if not, ages older than 27 Ma in the geological record of Western and Central Europe (Table 1; Demoulin et al., 2018; Hautmann and Lippolt, 2000; Yans, 2003). This means that the 26.8 ± 0.2 Ma age obtained in the Bihain quarry is the oldest and may correspond to the onset of an intense (?) weathering wave in Europe. Considering the continuous range of values, it is reasonable to consider that weathering processes may have operated more or less continuously during the whole period lasting from Chattian (27 Ma) to Pliocene (2.5 Ma). However, this long period of weathering is probably accompanied by several pulses under more suitable conditions, during when weathering seems to have been recorded more conspicuously by the K-Mn oxides. Two weathering periods are particularly well identified (Figs. 10e and 13): (1) Early Miocene (~23–18.5 Ma) and (2) Middle-Late Miocene (~12–7 Ma). Two other periods, less important in the age record, are the late Oligocene onset (27–25 Ma) and the Pliocene event (5.3–2.5 Ma), marking the end of the long-lasting Neogene weathering period.

The late Oligocene onset is only observed in the Rhenish Massif (this study) and in the western side of the Central Massif in France, in the Romanèche mine (Figs. 1 and 13; Table 1; Hautmann and Lippolt, 2000). This could lead to the interpretation that these areas were better preserved from erosion or they were exposed to meteoric agents earlier, unless the set of data is not exhaustive. The Early Miocene phase is well-constrained in several locations (Odenwald, Rhenish Massif, Central Massif, Harz and Erzgebirge), meaning that they where exposed to meteoric agents at least since the earliest Miocene. The large set of ages in the range between ~7–12 Ma is also observed in the Black Forest (Hautmann and Lippolt, 2000; Segev et al., 1992), in the Thüringer Wald, the Erzgebirge and in the Pfalz massifs (Hautmann and Lippolt, 2000). Similar ages are also identified in U deposits of the Bohemian Massif (Dill, 1985b), meaning that this weathering phase is not a local artefact but extends in different massifs of Western and Central Europe. The decrease in the age record after the Middle Miocene weathering phase is interpreted to be connected to the progressive cooling of the continent (Hautmann and Lippolt, 2000). The Pliocene period probably not records intense weathering but rather denudation conditions. For example, Dill et al. (2010) interpreted Pliocene cryptomelane crust pebbles (dated by K-Ar) in paleochanels to be correlative of the peneplanation of the Bohemian massif and the paleohydraulic system at the base of the weathering profile.

Hautmann and Lippolt (2000) suggested that a single global driver for weathering in the European massifs is difficult to explain, given the wide variability of the ^{40}Ar/^{39}Ar data. Weathering processes probably not operated in the same way and with the same intensity in all of these massifs, although they probably underwent a same long-lasting late Oligocene-Neogene weathering period. Local factors seem to be important, rather than large-scale changes such as those observed by Vasconcelos (1999). Therefore, Hautmann and Lippolt (2000) suggested that weathering in Western Europe was triggered asynchronously in the foreland massifs of the Alpine orogenic belt, due to tectonic reactivation. This interpretation strengthen the importance of local geodynamics in the Ardenne (and the Rhenish Massif) late in the weathering history of Europe. These massifs could have been exposed during the same time window to meteoric fluids, but were stripped

differently due to the variability in the local geodynamic settings. Why older periods (i.e., Eocene, Cretaceous, Permian, …) are not reported in the ^{40}Ar/^{39}Ar age record is not perfectly understood, since these periods are particularly well documented in Europe (see synthesis by Migoń and Lidmar-Bergström, 2002, 2001). The absence of datable material could be invoked, but seems to be irrelevant given the number of analyses. The best interpretation should consider that the upper part of the laterite *s.l.* is currently absent in almost all sampled locations. Hence, the weathering profile is not completely preserved (laterite *s.s.* is absent) and older weathering periods are mostly removed from these deposits. Therefore, the combining effect of high precipitations and the creation of relief are responsible for the formation of Mn oxides but also to their erosion. Consequently, geodynamics is probably an important parameter creating the water gradient and opening the permeability of rocks with fractures and joints. The water in the system is supplied by the wet climate.

There are also important consequences in the understanding of the paleo-drainage system of the Western European basins, as most of the material belonging to the upper part of the weathering mantle recently (Quaternary?) fed temporary rivers and sedimentary basins. This has resulted in some parts of the Variscide to the formation of channel deposits (Dill et al., 2010; Dill and Wemmer, 2012). In terms of economic geology, this means that the supergene zone of Mn deposits (and others?) in these massifs is not preserved in comparison to their Australian, South American or African counterparts, where several weathering stages are commonly detected (e.g., Anand, 2005; Beukes et al., 2016; Dammer et al., 1999, 1996; De Putter et al., 2018, 2015; Gutzmer et al., 2012; Hénocque et al., 1998; Ruffet et al., 1996; Vasconcelos et al., 1992, 2018; Beauvais et al., 2008, 2016). The economic potential of this zone is then limited in Western European Mn deposits. Comparable conclusions were drawn from Mn deposits in China (e.g., Li et al., 2007), where the most (economically) important part of the supergene zone was stripped. However, further studies are needed to complete and better constrain the available set of data in other European massifs (Table 1).

The position of the Ardenne massif in comparison with other areas (Fig. 1) is interesting because this is the only place (at this time) where the whole Miocene weathering phase is recorded by the K-Mn oxides. Additionally, there is still work to do in tracing with accuracy the older periods with the ^{40}Ar/^{39}Ar method as several studies have provided older ages belonging to the Eocene and Cretaceous events (Barbier et al., 2010; Bruyère et al., 2003; Thiry et al., 2006; Yans, 2003). The certainty is that an important set of ages is needed to fully understand the evolution of weathering and erosion in these massifs, rather than isolated ages.

7. Conclusion

New geochronological, petrographical, mineralogical and geochemical data of the Mn-rich slates and coticule of the Ottré Formation in the Stavelot Massif (eastern Ardenne, Belgium) indicate that these deposits record several stages of weathering belonging to a long lasting late Oligocene – Neogene weathering period. The two investigated areas correspond to two types of Mn deposits: the Chevron area (north) is poorly affected by weathering processes and correspond mainly to a carbonate-hosted sedimentary deposit, whereas the Salmchâteau Mn-rich rocks (south) are considered as weathering deposits (Hunsrück-type IV). The difference in the intensity of weathering between these ores is attributed to the elevation of these two locations, higher elevated in the Salmchâteau area, leading to position the Mn orebeds in the lower part of the saprolite, and in the fissured horizon in the Salmchâteau and Chevron areas, respectively. This has led weathered Mn-rich slates to be enriched in Mn and associated transition metals (As, Co, Cu, Ni) than poorly weathered ones. The mineralogy of the weathering products is dominated by cryptomelane and nsutite, with subordinate amounts of lithiophorite, manganite and pyrolusite,

together with goethite and kaolinite. Mn oxides without supplementary cations (nsutite, manganite and pyrolusite) result from the weathering of Mn carbonates (rhodochrosite and/or kutnohorite). The subsequent neoformed cryptomelane and lithiophorite fill open voids or replace the phyllosilicate matrix of the slates by the recombination of K, Li and Al with Mn released from the dissolution of phyllosilicate and Mn carbonates, respectively. The input of Mn from spessartine and other Mn-bearing silicates have poorly contributed to the weathering fluid.

^{40}Ar/^{39}Ar dating of cryptomelane from the Salmchâteau Mn deposits yield, at least, four weathering periods lasting from late Oligocene to Pliocene or younger, without excluding older periods, as the upper part of the saprolite (and laterite) have been removed. As the tropical Paleocene-Eocene climate evolves into temperate by the Oligocene, and temperatures decrease progressively until the present, warm climate seems not to be the major parameter controlling the formation of Mn oxides and the development of weathering profiles in the Salmchâteau area. An additional parameter implies the onset of the Ardenne Massif uplift from late Oligocene to present days to trigger the development of weathering mantles. The constant precipitations and increasing seasonality provide water to the weathering fluids, when the dooming of the massif, maybe associated with the Alpine and/or the Roer graben activity, account for most of the weathering gradient. The Ardenne (Rhenish Massif) records the oldest ^{40}Ar/^{39}Ar ages ever obtained in other Variscan massifs, delimiting a relatively continuous long-lasting weathering period from late Oligocene (~27 Ma) to Pliocene (2.5 Ma). Two main weathering pulses are also supported by numerous K-Mn oxide datings during the Early Miocene (23–18 Ma) and Middle-Late Miocene (12–7 Ma). The absence of older weathering stages recorded in supergene Mn deposits located in the Alpine foreland strengthen the interpretation that an important phase of denudation has removed most of the upper part of the weathering profiles. This limits the global economic potential of the supergene zone in Mn deposits within these massifs.

Appendix A. Supplementary data

Supplementary data to this article can be found online at https://doi.org/10.1016/j.oregeorev.2019.103191. These data include Google maps of the most important areas described in this article.

References

Adams, R., Vandenberghe, N., 1999. The Meuse section across the Condroz-Ardennes (Belgium) based on a predeformational sediment wedge. Tectonophysics 309, 179–195. https://doi.org/10.1016/S0040-1951(99)00138-9.

Albers, H.J., 1981. Neue daten zum klima des nordwesteuropälschen Alttertiars. Fortschritte Geol. Von Rheinl. Westfal. 29, 483–504.

Alexandre, J., Thorez, J., 1995. Au secondaire et au tertiaire, l'Ardenne tropicale. L'altération des roches et les climats anciens, in: L'Ardenne. Essai de Géographie Physique. Publication du Département de Géographie physique et Quaternaire de l'Université de Liège, Liège, pp. 53–67.

Anand, R.R., 2005. Weathering history, landscape evolution and implications for exploration, in: Anand, R.R., de Broekert, P. (Eds.), Regolith Landscape Evolution across Australia. Cooperative Research Centre for Landscape Environments and Mineral Exploration, Bentley, pp. 2–40.

Baele, J.-M., Quesnel, F., Dupuis, C., 2016. Silcrete in northern France and Belgium: a terrestrial record of surface environments under the influence of pyroclastic ash-falls. In: Abstract Book. Presented at the 5th International Geologica Belgica Meeting, pp. 40.

Baijot, M., Hatert, F., Fransolet, A.-M., 2011. Mineralogical and geochemical study of pseudocoticule from the Stavelot Massif, Ardennes (Belgium), and redefinition of coticule. Eur. J. Mineral. 23, 633–644. https://doi.org/10.1127/0935-1221/2011/0023-2115.

Barbarand, J., Bour, I., Pagel, M., Quesnel, F., Delcambre, B., Dupuis, C., Yans, J., 2018. Post-Paleozoic evolution of the northern Ardenne Massif constrained by apatite fission-track thermochronology and geological data. BSGF - Earth Sci. Bull. 189, 16. https://doi.org/10.1051/bsgf/2018015.

Barbier, F., Prognon, C., Quesnel, F., Dupuis, C., Yans, J., 2010. Dating and weathering characterization of the Morialmé quarry (Entre-Sambre-et-Meuse, Belgium), in: 4th French Congress on Stratigraphy. Presented at the Abstract book, Paris, p. 18.

Beauvais, A., Bonnet, N.J., Chardon, D., Arnaud, N., Jayananda, M., 2016. Very long-term stability of passive margin escarpment constrained by ^{40}Ar/^{39}Ar dating of K-Mn oxides. Geology 44, 299–302. https://doi.org/10.1130/G37303.1.

Beauvais, A., Ruffet, G., Hénocque, O., Colin, F., 2008. Chemical and physical erosion rhythms of the West African Cenozoic morphogenesis: The ^{39}Ar-^{40}Ar dating of supergene K-Mn oxides. J. Geophys. Res. 113. https://doi.org/10.1029/2008JF000996.

Berger, P., 1965. Les dépôts sédimentaires de manganèse de la Lienne inférieure. Ann. Société Géologique Belg. 88, 245–267.

Beukes, N.J., Swindell, E.P.W., Wabo, H., 2016. Manganese deposits of Africa. Episodes 39, 285. https://doi.org/10.18814/epiiugs/2016/v39i2/95779.

Biagioni, C., Capalbo, C., Pasero, M., 2013. Nomenclature tunings in the hollandite supergroup. Eur. J. Mineral. 25, 85–90. https://doi.org/10.1127/0935-1221/2013/0025-2255.

Blondieau, M., 2019. Le manganèse en Ardenne, Stâve dès Boûs. ed, Nature, histoire et vien en Ardenne. Trois-Ponts.

Blondieau, M., 2006. Description des espèces minérales présentes dans les gisements salmiens du. Massif de Stavelot.

Blondieau, M., 2005. Les gisements minéraux du Salmien dans le massif de Stavelot.

Blondieau, M., Puccio, S., Compere, P., Hatert, F., 2017. Données nouvelles sur quelques espèces minérales de Vielsalm et de Salmchâteau. Bull. Société R. Sci. Liège 86, 1–48.

Bottke, H., 1969. Die Eisenmanganerze der Grube Dr. Geier bei Bingen/Rhein als Verwitterungsbildungen des Mangans vom Typ Lindener Mark. Miner. Deposita 4, 355–367. https://doi.org/10.1007/BF00207163.

Boulvain, F., Belanger, I., Ghysel, P., Laloux, M., Roche, M., Delsate, D., Dosquet, D., Thorez, J., Godefroit, P., 2000. New lithostratigraphical, sedimentological, mineralogical and palaeontological data on the Mesozoic of Belgian Lorraine. Geol. Belg. 3, 3–33.

Boulvain, F., Vandenberghe, N., 2018. An introduction to the geology of belgium and luxembourg, in: Demoulin, A. (Ed.), Landscapes and Landforms of Belgium and Luxembourg. Springer International Publishing, Cham, pp. 9–33. https://doi.org/10.1007/978-3-319-58239-9_2.

Brannath, A., Smykatz-Kloss, W., 1992. Mineralogische Untersuchungen an einigen hessischen Mangan-Eisenervorkommen. Chem. Erde - Geochem. 52, 3–31.

Bruyère, D., De Putter, T., Perruchot, A., Dupuis, C., 2003. Neogenesis of halloysite in cryptokarstic environments (Beez, Belgium): chemical modeling. In: in: Abstract Book. Presented at the Conference of the European clay groups association, pp. 48.

Buchardt, B., 1978. Oxygen isotope palaeotemperatures from the Tertiary period in the North Sea area. Nature 275, 121–123. https://doi.org/10.1038/275121a0.

Carl, C., Dill, H., 1985. Age of secondary uranium mineralizations in the basement rocks of northeastern Bavaria, F.R.G. Chem. Geol. Isot. Geosci. Sect. 52, 295–316. https://doi.org/10.1016/0168-9622(85)90041-7.

Carroll, D., 1970. Trace Elements in Weathering, in: Rock Weathering. Springer US, Boston, MA, pp. 145–168. https://doi.org/10.1007/978-1-4684-1794-4_12.

Chisonga, B.C., Gutzmer, J., Beukes, N.J., Huizenga, J.M., 2012. Nature and origin of the protolith succession to the Paleoproterozoic Serra do Navio manganese deposit, Amapa Province. Brazil. Ore Geol. Rev. 47, 59–76. https://doi.org/10.1016/j.oregeorev.2011.06.006.

Cocks, L.R.M., Fortey, R.A., 2009. Avalonia: a long-lived terrane in the Lower Palaeozoic? Geol. Soc. Lond. Spec. Publ. 325, 141–155. https://doi.org/10.1144/SP325.7.

Cocks, L.R.M., Torsvik, T.H., 2002. Earth geography from 500 to 400 million years ago: a faunal and palaeomagnetic review. J. Geol. Soc. 159, 631–644. https://doi.org/10.1144/0016-764901-118.

Cosan, Y., 1969. Etude géologique de sondages au Plateau des tailles. Mém. Serv, Géologique Belg, pp. 32.

Dammer, D., Chivas, A.R., McDougall, I., 1996. Isotopic dating of supergene manganese oxides from the Groote Eylandt Deposit, Northern Territory. Australia. Econ. Geol. 91, 386–401. https://doi.org/10.2113/gsecongeo.91.2.386.

Dammer, D., McDougall, I., Chivas, A.R., 1999. Timing of weathering-induced alteration of manganese deposits in Western Australia; evidence from K/Ar and 40Ar/39Ar dating. Econ. Geol. 94, 87–108. https://doi.org/10.2113/gsecongeo.94.1.87.

De Man, E., Ivany, L., Vandenberghe, N., 2004. Stable oxygen isotope record of the

Eocene-Oligocene transition in the southern North Sea Basin: positioning the Oi-1 event. Neth. J. Geosci. 83, 193–197. https://doi.org/10.1017/S0016774600020266.

De Putter, T., Liégeois, J.-P., Dewaele, S., Cailteux, J., Boyce, A., Mees, F., 2018. Paleoproterozoic manganese and base metals deposits at Kisenge-Kamata (Katanga, D.R. Congo). Ore Geol. Rev. 96, 181–200. https://doi.org/10.1016/j.oregeorev.2018.04.015.

De Putter, T., Ruffet, G., Yans, J., Mees, F., 2015. The age of supergene manganese deposits in Katanga and its implications for the Neogene evolution of the African Great Lakes Region. Ore Geol. Rev. 71, 350–362. https://doi.org/10.1016/j.oregeorev.2015.06.015.

Deckers, J., 2016. The Late Oligocene to Early Miocene early evolution of rifting in the southwestern part of the Roer Valley Graben. Int. J. Earth Sci. 105, 1233–1243. https://doi.org/10.1007/s00531-015-1236-5.

Decrée, S., Ruffet, G., Putter, T.D., Baele, J.-M., Recourt, P., Jamoussi, F., Yans, J., 2010. Mn oxides as efficient traps for metal pollutants in a polyphase low-temperature Pliocene environment: A case study in the Tamra iron mine, Nefza mining district. Tunisia. J. Afr. Earth Sci. 57, 249–261. https://doi.org/10.1016/j.jafrearsci.2009.08.005.

Dejonghe, L., 2008. Notice de la carte géologique de Wallonie. Hotton Dochamps, pp. 55/5-6,.

Dejonghe, L., 1985. Mineral deposits of Belgium. Bull. Société Belge Géologie 94, 283–297.

Dejonghe, L., Boni, M., 2005. The "Calamine-type" zinc lead deposits in Belgium and West Germany: a product of Mesozoic paleoweathering processes. Geol. Belg. 8, 3–14.

Dekoninck, A., Bernard, A., Barbarand, J., Saint-Bezar, B., Missenard, Y., Lepretre, R., Saddiqi, O., Yans, J., 2016a. Detailed mineralogy and petrology of manganese oxy-hydroxide deposits of the Imini district (Morocco). Miner. Deposita 51, 13–23. https://doi.org/10.1007/s00126-015-0590-3.

Dekoninck, A., Leprêtre, R., Saddiqi, O., Barbarand, J., Yans, J., 2016b. The high-grade Imini manganese district—karst-hosted deposits of mn oxides and oxyhydroxides, in: Bouabdellah, M., Slack, J.F. (Eds.), Mineral Deposits of North Africa. Springer International Publishing, Cham, pp. 575–594.

Demoulin, A. (Ed.), 2018. Landscapes and Landforms of Belgium and Luxembourg, World Geomorphological Landscapes. Springer International Publishing, Cham. https://doi.org/10.1007/978-3-319-58239-9.

Demoulin, A., 2006. La néotectonique de l'Ardenne-Eifel et des regions avoisinantes. Mémoire de la Classe des Sciences Collection, Académie Royale de Belgique, Bruxelles.

Demoulin, A., 2003. Paleosurfaces and residual deposits in Ardenne-Eifel: historical overview and perspectives. Géologie Fr. 17–21.

Demoulin, A., 1995a. L'Ardenne des plateaux, héritage des temps anciens. Surfaces d'érosion en Ardenne, in: L'Ardenne. Essai de Géographie Physique. Publication du Département de Géographie physique et Quaternaire de l'Université de Liège, Liège, pp. 68–93.

Demoulin, A., 1995b. L'Ardenne, essai de géographie physique. Publication du Département de Géographie physique et Quaternaire de l'Université de Liège, Liège.

Demoulin, A., 1995c. Neotectonique du Massif Ardennais, in: Demoulin, A., L'Ardenne. Essai de Géographie Physique. Publication du Département de Géographie physique et Quaternaire de l'Université de Liège, Liège, pp. 110–135.

Demoulin, A., Barbier, F., Dekoninck, A., Verhaert, M., Ruffet, G., Dupuis, C., Yans, J., 2018. Erosion surfaces in the Ardenne-Oesling and their associated kaolinic weathering mantle. In: Demoulin, A. (Ed.), Landscapes and Landforms of Belgium and Luxembourg. Springer International Publishing, Cham, pp. 63–84. https://doi.org/10.1007/978-3-319-58239-9_5.

Demoulin, A., Hallot, E., 2009. Shape and amount of the Quaternary uplift of the western Rhenish shield and the Ardennes (western Europe). Tectonophysics 474, 696–708. https://doi.org/10.1016/j.tecto.2009.05.015.

Demoulin, A., Quesnel, F., Dupuis, C., Gerrienne, P., Yans, J., 2010. Cenomanian sands and clays north of the Vesdre valley: the oldest known Cretaceous deposits in Eastern Belgium. Geol. Belg. 11, 241–256.

Dill, H.G., 2010. The "chessboard" classification scheme of mineral deposits: Mineralogy and geology from aluminum to zirconium. Earth-Sci. Rev. 100, 1–420. https://doi.org/10.1016/j.earscirev.2009.10.011.

Dill, H.G., 1985a. Terrestrial ferromanganese ore concentrations from mid-european basement blocks and their implication concerning the environment of formation during the late cenozoic (northern Bavaria, F.R.G.). Sediment. Geol. 45, 77–96. https://doi.org/10.1016/0037-0738(85)90024-7.

Dill, H.G., 1985b. Genesis and timing of secondary uranium mineralization in northern Bavaria (FR of Germany) with special reference to geomorphology. Uranium 2, 1–16.

Dill, H.G., Hansen, B., Keck, E., Weber, B., 2010. Cryptomelane: A tool to determine the age and the physical–chemical regime of a Plio-Pleistocene weathering zone in a granitic terrain (Hagendorf, SE Germany). Geomorphology 121, 370–377. https://doi.org/10.1016/j.geomorph.2010.05.004.

Dill, H.G., Sachsenhofer, R.F., Grecula, P., Sasvari, T., Palinkas, L.A., Borojevic-Sostaric, S., Strmic-Palinkas, S., Prochaska, W., Garuti, G., Zaccarini, F., Arbouille, D., Schulz, H.-M., 2008. Fossil fuels, ore and industrial minerals, in: McCann, T. (Ed.), The Geology of Central Europe Volume 2: Mesozoic and Cenozoic. The Geological Society of London, pp. 1341–1449. https://doi.org/10.1144/CEV2P.9.

Dill, H.G., Wemmer, K., 2012. Origin and K/Ar age of cryptomelane-bearing Sn placers on silcretes, SE Germany. Sediment. Geol. 275–276, 70–78. https://doi.org/10.1016/j.sedgeo.2012.07.016.

Dupuis, C., Charlet, J.-M., Dejonghe, L., Thorez, J., 1996. Reconnaissance par carottage des paléoaltérations kaolinisées mésozoïques de la Haute Ardenne (Belgique). Ann. Société Géologique Belg. 119, 91–109.

Dusar, M., Lagrou, D., 2007. Cretaceous flooding of the Brabant Massif and the lithostratigraphic characteristics of its chalk cover in northern Belgium. Geol. Belg. 10,

27–38.

Dussart, N., Dussart, J., 1991. Les mines de Chevron et Rahier. Le manganèse de la basse vallée de la Lienne. 1857–1934.

Echle, W., Plüger, W.L., Zielinski, J., Frank, B., Scheps, V., 1985. Petrography, mineralogy and geochemistry of the Salmian rocks from research borehole Konzen, Hohes Venn (West Germany). Neues Jahrb. Für Geol. Paläontol. Abh. 171, 31–50.

Ferket, H., Muchez, P., Schroyen, K., Sintubin, M., 1998. Metamorphism in the Stavelot-Venn Massif: a study of quartz veins in the basal Devonian conglomerates (Lochkovian). Aardkd. Meded. 9, 7–16.

Fielitz, W., Mansy, J.-L., 1999. Pre- and synorogenic burial metamorphism in the Ardenne and neighbouring areas (Rhenohercynian zone, central European Variscides). Tectonophysics 309, 227–256. https://doi.org/10.1016/S0040-1951(99)00141-9.

Fonseca, E., 1969. Contribution à la géochimie de l'arsenic dans le gisement sédimentaire de manganèse de la Lienne inférieure. Bull. Société Belge Géologie 78, 147–154.

Fransolet, A.-M., 1979. Occurences de lithiophorite, nsutite et cryptomélane dans le massif de Stavelot. Belgique. Ann. Société Géologique Belg. 102, 303–312.

Fransolet, A.-M., Hatert, F., Bernhardt, H.-J., Theye, T., Maresch, W., 2007. Occurrence of sursassite in the Lienne valley, Stavelot Massif, Belgian Ardennes, in: Goldschmidt Conference Abstracts. Presented at the Goldschmit, Cologne, p. A294.

Fransolet, A.-M., Mélon, J., 1975. Données nouvelles sur des minéraux de Belgique. Extr. Bull. Société R. Sci. Liège 157–160.

Garcia-Castellanos, D., Cloetingh, S., Van Balen, R., 2000. Modelling the Middle Pleistocene uplift of the Ardennes-Rhenish Massif: thermo-mechanical weakening under the Eifel? Glob. Planet. Change 27, 39–52. https://doi.org/10.1016/S0921-8181(01)00058-3.

Geukens, F., 1999. Notes accompagnant une révision de la carte structurale du Massif de Stavelot. Aardkd. Meded. 9, 183–190.

Geukens, F., 1986. Commentaires à la carte géologique du Massif de Stavelot. Aardkd. Meded. 3, 15–30.

Geukens, F., 1975. La faille de Bra et le graben de Malmedy. Ann. Société Géologique Belg. 98, 331–339.

Geukens, F., 1965. Problèmes stratigraphiques relatifs aux planchettes Odeigne-Bihain. Bull. Société Belge Géologie 73, 214–219.

Geukens, F., 1957. Quelques remarques au sujet de la répartition des Dicyionema fla-belliforme dans le Massif Cambrien de Stavelot (Belgique), in: Congrès Géologique International. Alger XV, pp. 45–52.

Gilg, H.A., 2000. D-H evidence for the timing of kaolinization in Northeast Bavaria. Germany. Chem. Geol. 170, 5–18. https://doi.org/10.1016/S0009-2541(99)00239-9.

Goemaere, E., Demarque, S., Dreesen, R., Declercq, P.-Y., 2016. The geological and cultural heritage of the Caledonian Stavelot-Venn Massif, Belgium. Geoheritage 8, 211–233. https://doi.org/10.1007/s12371-015-0155-y.

Graulich, J.-M., 1966. Le sondage du bois des Hovas-Chevron (Sondage No. 7). Ministère des affaires économiques, administration des mines, Bruxelles.

Gullentops, F., 1954. Contribution à la chronologie du Pleistocene et des formes du relief en Belgique. Mém. Inst. Géologie Univ. Cathol. Louvain 18, 123–252.

Gustine, C., 2002. Les associations d'oxydes et hydroxydes de manganèse dans le Massif de Stavelot (Unpublished Master thesis). Université de Liège, Liège.

Gutzmer, J., Du Plooy, A.P., Beukes, N.J., 2012. Timing of supergene enrichment of low-grade sedimentary manganese ores in the Kalahari Manganese Field. South Africa. Ore Geol. Rev. 47, 136–153. https://doi.org/10.1016/j.oregeorev.2012.04.003.

Hance, L., Dejonghe, L., Ghysel, P., Laloux, M., Mansy, J.L., 1999. Influence of heterogeneous lithostructural layering on orogenic deformation in the Variscan Front Zone (eastern Belgium). Tectonophysics 309, 161–177. https://doi.org/10.1016/S0040-1951(99)00137-7.

Hance, L., Dejonghe, L., Graulich, J.-M., 1992. Lower Devonian stratigraphy in the Vesdre Massif. Belgium. Ann. Société Géologique Belg. 115, 119–134.

Hardenbol, J., Thierry, J., Farley, M.B., Jacquin, T., de Graciansky, P.-C., Vail, P.R., 1998. Mesozoic and Cenozoic sequence chronostratigraphic chart, in: Mesozoic and Cenozoic Sequence Stratigraphy of European Basins, SEPM Special Publication. Society for Sedimentary Geology.

Hatert, F., Blondieau, M., Puccio, S., Baijot, M., Gustine, C., 2014. Le gisement de manganèse de la Vallée de la Lienne (Belgique). Règne Minéral 117, 5–24.

Hautmann, S., Lippolt, H.J., 2000. 40Ar/39Ar dating of central European K-Mn oxides — a chronological framework of supergene alteration processes during the Neogene. Chem. Geol. 170, 37–80. https://doi.org/10.1016/S0009-2541(99)00241-7.

Hénocque, O., Ruffet, G., Colin, F., Féraud, G., 1998. 40Ar/39Ar dating of West African lateritic cryptomelanes. Geochim. Cosmochim. Acta 62, 2739–2756. https://doi.org/10.1016/S0016-7037(98)00185-9.

Herbosch, A., 1967. La viridine et la braunite de Salmchâteau. Bull. Société Belge Géologie 80, 183–201.

Herbosch, A., 1965. Contribution à l'étude géochimique de l'arsenic dans le Salmien entre Vielsalm et Salm-Château (Unpublished Master thesis). Université Libre de Bruxelles, Bruxelles.

Herbosch, A., Liégeois, J.-P., Pin, C., 2016. Coticules of the Belgian type area (Stavelot-Venn Massif): Limy turbidites within the nascent Rheic oceanic basin. Earth-Sci. Rev. 159, 186–214. https://doi.org/10.1016/j.earscirev.2016.05.012.

Herbosch, A., Verniers, J., 2014. Stratigraphy of the Lower Palaeozoic of the Brabant Massif, Belgium. Part II: The Middle Ordovician to lowest Silurian of the Rebecq Group. Geol. Belg. 17, 115–136.

Herbosch, A., Verniers, J., 2013. Stratigraphy of the Lower Palaeozoic of the Brabant Massif, Belgium. Part I: The Cambro-Ordovician from the Halle and Ottignies groups. Geol. Belg. 16, 49–65.

Johnson, J.E., Webb, S.M., Ma, C., Fischer, W.W., 2016. Manganese mineralogy and diagenesis in the sedimentary rock record. Geochim. Cosmochim. Acta 173, 210–231.

https://doi.org/10.1016/j.gca.2015.10.027.

Koppers, A.A.P., 2002. ArArCALC—software for40Ar/39Ar age calculations. Comput. Geosci. 28, 605–619. https://doi.org/10.1016/S0098-3004(01)00095-4.

Kramm, U., 1980. Muskovit-Paragonit Phasenbeziehungen in niedriggradig metamorphen Schiefern des Venn-Stavelot Massivs. Ardennen. Tschermaks Mineral. Petrogr. Mitteilungen 27, 153–167. https://doi.org/10.1007/BF01082405.

Kramm, U., 1976. The coticule rocks (spessartine quartzites) of the Venn-Stavelot Massif, Ardennes, a volcanoclastic Metasediment? Contrib. Mineral. Petrol. 56, 135–155. https://doi.org/10.1007/BF00399600.

Kramm, U., Bühl, D., 1985. U-Pb zircon dating of the Hill Tonalite, Venn-Stavelot Massif, Ardennes. Neues Jahrb. Für Geol. Paläontol. Abh. 171, 329–337.

Krosse, S., Schreyer, W., 1993. Comparative geochemistry of coticules (spessartine-quartzites) and their redschist country rocks in the Ordovician of the Ardennes Mountains. Belgium. Chem. Erde - Geochem. 53, 1–20.

Kuleshov, V., 2016. Isotope geochemistry: the origin and formation of manganese rocks and ores. Elsevier, Amsterdam Boston Heidelberg London New York Oxford Paris San Diego San Francisco Singapore Sydney Tokyo.

Lamens, J., 1986. Depositional history of Salmian (Lower Ordovician sediments in Belgium). Aardkd. Meded. 3, 125–138.

Lamens, J., 1985a. Transition from turbidite to shallow-water sedimentation in the Lower Salmian (Tremadocian, Lower Ordovician) of the Stavelot Massif. Belgium. Sediment. Geol. 44, 121–142. https://doi.org/10.1016/0037-0738(85)90036-3.

Lamens, J., 1985b. Het Salmiaan (Onder Ordivicum) in het Massief van Stavelot (Unpublished. Katholieke Universiteit Leuven, Leuven Ph.D. thesis).

Lamens, J., Geukens, F., 1984. Volcanic activity in the Lower Ordovician of the Stavelot Massif, Belgium. Meded. Van K. Acad. Voor Wet. Lett. En Schone Kunsten Van Belgïe 46, 1–13.

Lamens, J., Geukens, F., Viaene, W., 1986. Geological setting and genesis of coticules (spessartine metapelites) in the Lower Ordovician of the Stavelot Massif. Belgium. J. Geol. Soc. 143, 253–258. https://doi.org/10.1144/gsjgs.143.2.0253.

Laznicka, P., 1992. Manganese deposits in the global lithogenetic system: Quantitative approach. Ore Geol. Rev. 7, 279–356. https://doi.org/10.1016/0169-1368(92)90013-B.

Li, J.-W., Vasconcelos, P., Zhang, W., Deng, X.-D., Duzgoren-Aydin, N., Yan, D.-R., Zhang, J.-Q., Hu, M.-A., 2007. Timing and duration of supergene mineralization at the Xinrong manganese deposit, western Guangdong Province, South China: cryptomelane 40Ar/39Ar dating. Miner. Deposita 42, 361–383. https://doi.org/10.1007/s00126-006-0118-y.

Libert, J., 1905. Les gisements ferro-manganésifères de la Lienne. Ann. Société Géologique Belg. 32, 144–154.

Linnemann, U., Herbosch, A., Liégeois, J.-P., Pin, C., Gärtner, A., Hofmann, M., 2012. The Cambrian to Devonian odyssey of the Brabant Massif within Avalonia: a review with new zircon ages, geochemistry, Sm–Nd isotopes, stratigraphy and palaeogeography. Earth-Sci. Rev. 112, 126–154. https://doi.org/10.1016/j.earscirev.2012.02.007.

Ma, Y., Liu, C., 1999. Trace element geochemistry during chemical weathering: As exemplified by the weathered crust of granite, Longnan. Jiangxi. Chin. Sci. Bull. 44, 2260–2263. https://doi.org/10.1007/BF02885934.

Mansy, J.L., Everaerts, M., De Vos, W., 1999. Structural analysis of the adjacent Acadian and Variscan fold belts in Belgium and northern France from geophysical and geological evidence. Tectonophysics 309, 99–116. https://doi.org/10.1016/S0040-1951(99)00134-1.

Maynard, J.B., 2014. Manganiferous sediments, rocks, and ores. Treatise on Geochemistry. Elsevier 327–349.

Maynard, J.B., 2010. The chemistry of manganese ores through time: a signal of increasing diversity of earth-surface environments. Econ. Geol. 105, 535–552. https://doi.org/10.2113/gsecongeo.105.3.535.

McLennan, S.M., 2001. Relationships between the trace element composition of sedimentary rocks and upper continental crust. Geochem. Geophys. Geosystems 2, 24. https://doi.org/10.1029/2000GC000109.

Mees, F., Stoops, G., 1999. Palaeoweathering of Lower Palaeozoic rocks of the Brabant Massif, Belgium: a mineralogical and petrographical analysis. Geol. J. 34, 349–367. https://doi.org/10.1002/(SICI)1099-1034(199911/12)34:4 < 349::AID-GJ830 > 3.0.CO;2-S.

Mélon, J., Bourguignon, P., Fransolet, A.-M., 1976. Les minéraux de Belgique, Lelotte. ed. Dison, Belgique.

Mélon, J., Bourguignon, P., Fransolet, A.-M., 1976. Les minéraux de Belgique, Lelotte. ed. Dison, Belgique.

Meyer, H.J., Walter, R., 1985. Technical performance and geological profile of the research borehole Konzen, Hohes Venn (West Germany). Neues Jahrb. Für Geol. Paläontol. Abh. 171, 17–29.

Meyer, W., Stets, J., 1998. unge Tektonik imRheinischen Schiefergebirge und ihre Quantifizierung. Z. Dtsch. Geol. Ges. 149, 359–379.

Michon, L., Van Balen, R.T., Merle, O., Pagnier, H., 2003. The Cenozoic evolution of the Roer Valley Rift System integrated at a European scale. Tectonophysics 367, 101–126. https://doi.org/10.1016/S0040-1951(03)00132-X.

Middelburg, J.J., van der Weijden, C.H., Woittiez, J.R.W., 1988. Chemical processes affecting the mobility of major, minor and trace elements during weathering of granitic rocks. Chem. Geol. 68, 253–273. https://doi.org/10.1016/0009-2541(88)90025-3.

Migoń, P., Lidmar-Bergström, K., 2002. Deep weathering through time in central and northwestern Europe: problems of dating and interpretation of geological record. CATENA 49, 25–40. https://doi.org/10.1016/S0341-8162(02)00015-2.

Migoń, P., Lidmar-Bergström, K., 2001. Weathering mantles and their significance for geomorphological evolution of central and northern Europe since the Mesozoic. Earth-Sci. Rev. 56, 285–324. https://doi.org/10.1016/S0012-8252(01)00068-X.

Mosbrugger, V., Utescher, T., Dilcher, D.L., 2005. Cenozoic continental climatic evolution of Central Europe. Proc. Natl. Acad. Sci. 102, 14964–14969. https://doi.org/10.

1073/pnas.0505267102.

Nahon, D.B., 1991. Self-organization in chemical lateritic weathering. Geoderma 51, 5–13. https://doi.org/10.1016/0016-7061(91)90063-Y.

Nash, D.J., McLaren, S.J. (Eds.), 2008. Geochemical sediments and landscapes, RGS-IBG book series. Blackwell Pub, Malden, MA.

Nicaise, D., 1985. Etude sédimentologique et géochimique du Salmien (Ordovicien Inférieur) de la coupe de la Salm (Unpublished Master thesis). Université Libre de Bruxelles, Bruxelles.

Nicholson, K., 1992. Genetic types of manganese oxide deposits in Scotland; indicators of paleo-ocean-spreading rate and a Devonian geochemical mobility boundary. Econ. Geol. 87, 1301–1309. https://doi.org/10.2113/gsecongeo.87.5.1301.

Oncken, O., von Winterfeld, C., Dittmar, U., 1999. Accretion of a rifted passive margin: The Late Paleozoic Rhenohercynian fold and thrust belt (Middle European Variscides). Tectonics 18, 75–91. https://doi.org/10.1029/98TC02763.

Onstott, T.C., Miller, M.L., Ewing, R.C., Arnold, G.W., Walsh, D.S., 1995. Recoil refinements: Implications for the 40Ar/39Ar dating technique. Geochim. Cosmochim. Acta 59, 1821–1834. https://doi.org/10.1016/0016-7037(95)00085-E.

Parc, S., Nahon, D., Tardy, Y., Vieillard, P., 1989. Estimated solubility products and fields of stability for cryptomelane, nsutite, birnessite, and lithiophorite based on natural lateritic weathering sequences. Am. Mineral. 74, 466–475.

Piessens, K., Sintubin, M., 1997. Partitioning of Variscan strain in the southern part of the Caledonian Stavelot-Venn inlier in the Ardenne Allochthon (Belgium). Aardkd. Meded. 8, 135–138.

Post, J.E., 1999. Manganese oxide minerals: crystal structures and economic and environmental significance. Proc. Natl. Acad. Sci. 96, 3447–3454. https://doi.org/10.1073/pnas.96.7.3447.

Price, J.R., Velbel, M.A., Patino, L.C., 2005. Rates and time scales of clay-mineral formation by weathering in saprolitic regoliths of the southern Appalachians from geochemical mass balance. Geol. Soc. Am. Bull. 117, 783. https://doi.org/10.1130/B25547.1.

Prodehl, C., Mueller, S., Glahn, A., Gutscher, M., Haak, V., 1995. Continental rifts: evolution, structure, tectonics, in: Continental Rifts: Evolution, Structure, Tectonics. K.H. Olsen, New York, pp. 133–212.

Prodehl, C., Mueller, St, Haak, V., 2006. The European Cenozoic rift system. In: Continental Rifts: Evolution. Structure, Tectonics, Developments in Geotectonics. Elsevier, pp. 133–212.

Quesnel, F., 2003. Paleoweathering and paleosurfaces from northern and eastern France to Belgium and Luxembourg: geometry, dating and geodynamic implications. Géologie Fr. 1, 95–104.

Quesnel, F., Dupuis, C., Yans, J., Demoulin, A., Wyns, R., Théveniaut, H., Farjanel, G., Voisin, L., Vergari, A., Baele, J.-M., De Putter, T., Colbach, R., Muller, A., Lacquement, F., Vandycke, S., Brulhet, J., 2002. Les paléoaltérations et paléosurfaces au NE de la France, en Belgique et au Luxembourg : état des connaissances, recherches en cours et implications géodynamiques méso-cénozoïques à l'échelle de la lithosphère nord-ouest européenne. Géologie Fr. 40.

Ruddiman, W.F., 2008. Earth's climate: past and future, 2nd ed. W.H. Freeman, New York.

Ruddiman, W.F., Prell, W.L., 1997. Introduction to the Uplift-Climate Connection. In: Ruddiman, W.F. (Ed.), Tectonic Uplift and Climate Change. Springer, US, Boston, MA, pp. 3–15.

Ruddiman, W.F., Raymo, M.E., Prell, W.L., Kutzbach, J.E., 1997. The uplift-climate connection: a synthesis. In: Ruddiman, W.F. (Ed.), Tectonic Uplift and Climate Change. Springer, US, Boston, MA, pp. 471–515.

Ruffet, G., Innocent, C., Michard, A., Féraud, G., Beauvais, A., Nahon, D., Hamelin, B., 1996. A geochronological and study of K-Mn oxides from the weathering sequence of Azul. Brazil. Geochim. Cosmochim. Acta 60, 2219–2232. https://doi.org/10.1016/0016-7037(96)00080-4.

Schreyer, W., Bernhardt, H.-J., Fransolet, A.-M., Armbruster, T., 2004. End-member ferrian kanonaite: an andalusite phase with one Al fully replaced by (Mn, Fe) 3+ in a quartz vein from the Ardennes mountains, Belgium, and its origin. Contrib. Mineral. Petrol. 147, 276–287. https://doi.org/10.1007/s00410-004-0557-3.

Schreyer, W., Bernhardt, H.-J., Medenbach, O., 1992. Petrologic Evidence for a Rhodochrosite Precursor of Spessartine in Coticules of the Venn-Stavelot Massif. Belgium. Mineral. Mag. 56, 527–532. https://doi.org/10.1180/minmag.1992.056.385.08.

Schreyer, W., Fransolet, A.-M., Bernhardt, H.-J., 2001. Hollandite–strontiomelane solid solutions coexisting with kanonaite and braunite in late quartz veins of the Stavelot Massif, Ardennes. Belgium. Contrib. Mineral. Petrol. 141, 560–571. https://doi.org/10.1007/s004100100260.

Segev, A., Lang, B., Halicz, L., 1991. K-Ar dating of manganese minerals from the Eisenbach region, Black Forest, southwest Germany. Schweiz. Mineral. Petrogr. Mitteilungen 71, 101–114. https://doi.org/10.5169/seals-54349.

Segev, A., Steinitz, G., Wauschkuhn, A., 1992. Dating of K-bearing manganese minerals - preliminary results. Geol. Surv. Isr. Curr. Res. 7, 39–41.

Sintubin, M., Debacker, T.N., Van Baelen, H., 2009. Early Palaeozoic orogenic events north of the Rheic suture (Brabant, Ardenne): A review. Comptes Rendus Geosci. 341, 156–173. https://doi.org/10.1016/j.crte.2008.11.012.

Stoops, G., 1962. Over het Conglomeraat van Malmedy. Natuurwetenschappen Tijdschr. 44, 81–96.

Theunissen, K., 1971. Verband tussen de tectonische vervorming en de metamorphe rekristallisatie in het doorbraakdal van de Salm te Salmchâteau (Unpublished. Katholieke Universiteit Leuven, Leuven Ph.D. thesis).

Théveniaut, H., Quesnel, F., Wyns, R., Hugues, G., 2007. Palaeomagnetic dating of the

"Borne de Fer" ferricrete (NE France): Lower Cretaceous continental weathering. Palaeogeogr. Palaeoclimatol. Palaeoecol. 253, 271–279. https://doi.org/10.1016/j.palaeo.2007.01.010.

Theye, T., Schreyer, W., Fransolet, A.-M., 1996. Low-Temperature, Low-Pressure Metamorphism of Mn-rich Rocks in the Lienne Syncline, Venn—Stavelot Massif (Belgian Ardennes), and the Role of Carpholite. J. Petrol. 37, 767–783. https://doi.org/10.1093/petrology/37.4.767.

Thiry, M., Quesnel, F., Yans, J., Wyns, R., Vergari, A., Theveniaut, H., Simon-Coiçon, R., Ricordel, C., Moreau, M.-G., Giot, D., Dupuis, C., Bruxelles, L., Barbarand, J., Baele, J.-M., 2006. Continental France and Belgium during the early Cretaceous: paleo-weatherings and paleolandforms. Bull. Société Géologique Fr. 177, 155–175. https://doi.org/10.2113/gssgfbull.177.3.155.

Torsvik, T.H., Van der Voo, R., Preeden, U., Mac Niocaill, C., Steinberger, B., Doubrovine, P.V., van Hinsbergen, D.J.J., Domeier, M., Gaina, C., Tohver, E., Meert, J.G., McCausland, P.J.A., Cocks, L.R.M., 2012. Phanerozoic polar wander, palaeogeography and dynamics. Earth-Sci. Rev. 114, 325–368. https://doi.org/10.1016/j.earscirev.2012.06.007.

Van Balen, R.T., Houtgast, R.F., Van der Wateren, F.M., Vandenberghe, J., Bogaart, P.W., 2000. Sediment budget and tectonic evolution of the Meuse catchment in the Ardennes and the Roer Valley Rift System. Glob. Planet. Change 27, 113–129. https://doi.org/10.1016/S0921-8181(01)00062-5.

Vandenven, G., 1991. Explications de la carte géologique du synclinorium de l'Eifel. Ann. Société Géologique Belg. 113, 103–113.

Vanguestaine, M., Breuer, P., Lehnert, O., 2004. Discovery of an Early Ordovician conodont fauna in the Salm Group of the Stavelot Inlier, Belgium. Bull. Inst. R. Sci. Nat. Belg. Sci. Terre 74, 39–48.

Varentsov, I.M., 1996. Manganese ores of supergene zone: Geochemistry of formation. Solid Earth Sciences Library, Springer, Netherlands, Dordrecht.

Vasconcelos, P.M., 1999. K-Ar and 40Ar/39Ar geochronology of weathering processes. Annu. Rev. Earth Planet. Sci. 27, 183–229. https://doi.org/10.1146/annurev.earth.27.1.183.

Vasconcelos, P.M., Becker, T.A., Renne, P.R., Brimhall, G.H., 1992. Age and duration of weathering by 40K/40Ar and 40Ar/39Ar analysis of potassium-manganese oxides. Science 258, 451–455. https://doi.org/10.1126/science.258.5081.451.

Vasconcelos, P.M., Carmo, I. de O., 2018. Calibrating denudation chronology through 40Ar/39Ar weathering geochronology. Earth-Sci. Rev. 179, 411–435. https://doi.org/10.1016/j.earscirev.2018.01.003.

Velbel, M.A., 1984. Natural weathering mechanisms of almandine garnet. Geology 12, 631. https://doi.org/10.1130/0091-7613(1984)12 < 631:NWMOAG > 2.0.CO;2.

Verhaert, M., Bernard, A., Saddiqi, O., Dekoninck, A., Essalhi, M., Yans, J., 2018. Mineralogy and Genesis of the Polymetallic and Polyphased Low Grade Fe-Mn-Cu Ore of Jbel Rhals Deposit (Eastern High Atlas, Morocco). Minerals 8, 39. https://doi.org/10.3390/min8020039.

Verniers, J., Herbosch, A., Vanguestaine, M., Geukens, F., Delcambre, B., Pingot, J.-L., Belanger, I., Hennebert, M., Debacker, T., Sintubin, M., De Vos, W., 2001. Cambrian-Ordovician-Silurian lithostratigraphic units (Belgium). Geol. Belg. 4, 5–38.

von Hoegen, J., von Lemme, B., Zielinski, J., Walter, R., 1985. Cambrian and Lower Ordovician in the Stavelot-Venn Massif: a model for the depositional history. Geol. Rundsch. 87, 407–435.

Wernicke, R.S., Lippolt, H.J., 1995. Direct isotope dating of a Northern Schwarzwald qtz–ba–hem vein. Neues Jb. Miner. Monat. 4, 161–172.

Widdowson, M., 2008. Laterite and Ferricrete, in: Nash, D.J., McLaren, S.J. (Eds.), Geochemical Sediments and Landscapes. Blackwell Publishing Ltd, Oxford, UK, pp. 45–94. https://doi.org/10.1002/9780470712917.ch3.

Wyns, R., 2002. Climat, eustatisme, tectonique: quels contrôles pour l'altération continentale? Exemple des séquences d'altération cénozoïques en France. Bull. Inf. Géologues Bassin Paris 39, 5–16.

Wyns, R., Quesnel, F., Simon-Coinçon, R., Guillocheau, F., Lacquement, F., 2003. Major weathering in France related to lithospheric deformation. Géologie Fr. 79–87.

Xu, C., Mansy, J.L., Van Den Haute, P., Guillot, F., Zhou, Z., Chen, J., De Grave, J., 2009. Late- and post-Variscan evolution of the Ardennes in France and Belgium: constraints from apatite fission-track data. Geol. Soc. Lond. Spec. Publ. 324, 167–179. https://doi.org/10.1144/SP324.13.

Yans, J., 2003. Chronologie des sédiments kaoliniques à faciès wealdien (Barrémien moyen à Albien supérieur; Bassin de Mons) et de la saprolite polyphasée (Crétacé inférieur et Miocène inférieur) de la Haute-Lesse (Belgique): implications géodynamiques et paléoclimatiques (Unpublished. Faculté Polytechnique de Mons, Université de Paris XI Orsay, Mons Ph.D. thesis).

Yans, J., Chauvin, A., Clauer, N., Dejax, J., De Putter, T., Dupuis, C., Feraud, G., Guillocheau, F., Masure, E., Leost, I., Perruchot, A., Pons, D., Spagna, P., Wyns, R., 2003. An overview of the saprolites of Belgium and their potential kaolinitic supplies to Mesozoic and Cenozoic sediments. Géologie Fr. 1, 33–37.

Yans, J., Dupuis, C., 2005. Timing of saprolitisation in the Haute-Lesse area (Belgium), in: Geophysical Research Abstract. Presented at the European union of Geosciences Meeting, Vienna.

Zachos, J., Pagani, M., Sloan, L., Thomas, E., Billups, K., 2001. Trends, rhythms, and aberrations in global climate 65 Ma to Present. Science 292, 686–693. https://doi.org/10.1126/science.1059412.

Ziegler, P.A., Dèzes, P., 2007. Cenozoic uplift of Variscan Massifs in the Alpine foreland: Timing and controlling mechanisms. Glob. Planet. Change 58, 237–269. https://doi.org/10.1016/j.gloplacha.2006.12.004.

Zwicker, W.K., Groeneveld-Meijer, W.O.J., Jaffe, H.W., 1962. Nsutite - a widespread manganese oxide mineral. Am. Mineral. 47, 618–623.